THESIS FOR THE DEGREE OF DOCTOR OF PHILOSOPHY

Vibrational and Structural Characterisation in Two Perovskite Challenges: A Density Functional Theory Study

Erik Jedvik Granhed

Department of Physics
CHALMERS UNIVERSITY OF TECHNOLOGY
Göteborg, Sweden 2019

Vibrational and Structural Characterisation in Two Perovskite Challenges:
A Density Functional Theory Study
Erik Jedvik Granhed

ISBN 978-91-7905-213-3

Doktorsavhandlingar vid Chalmers Tekniska Högskola
Ny serie nr 4680
ISSN 0346-718X

Department of Physics
Chalmers University of Technology
SE-412 96 Göteborg, Sweden
Telephone +46 31 772 10 00

Printed at Chalmers digitaltryck
Göteborg, Sweden 2019

Vibrational and Structural Characterisation in Two Perovskite Challenges: A Density Functional Theory Study

ERIK JEDVIK GRANHED
Department of Physics
Chalmers University of Technology

Abstract

The modelling of perovskites using density functional theory (DFT) can sometimes be a challenge with many different states very close in energy. In particular, the tilting of the inscribed octahedron, as well as the formation of electron polarons, leads to states with energy differences in the meV range. To distinguish between these states requires special care. This thesis investigates how the vibrational frequencies and defect-induced strain, or chemical expansion, can be used to distinguish between different states. For the polaron state in oxyhydride $BaTiO_3$, the comparison of calculations of hydrogen-ion vibrational frequencies to neutron scattering experiments is an excellent discriminator. The presence of polarons is deemed highly unlikely in unstrained material, despite the presence of oxygen vacancies. The observation is confirmed by comparisons of the strain tensor, calculated using a here-developed formalism. In $BaZrO_3$ the likelihood of an anti-ferrodistortive phase transition is a direct consequence of the magnitude of the R_{25}-mode frequency. The R_{25}-mode frequency is strongly dependent on the lattice spacing, but it is shown that the main effect of the inclusion of gradient corrections, as well as non-local correlation, is secondary and is mostly a consequence of the adjusted lattice constant. The inclusion of Fock exchange, however, leads to a significant stabilisation of the cubic phase, which is also verified by neutron scattering measurements. This thesis also concludes that the inclusion of Fock exchange, as found in hybrid functionals, is essential for a correct description of vibrational properties in both two studied perovskites.

Keywords: $BaZrO_3$, $BaTiO_3$, materials modelling, density functional theory, vibrational analysis, phonon, polaron, anti-ferrodistortive, chemical expansion, oxyhydride

LIST OF PUBLICATIONS

This thesis consists of an introductory text and the following papers:

I **Size and shape of oxygen vacancies and protons in acceptor-doped barium zirconate**
Erik Jedvik, Anders Lindman, Magnús Þór Benediktsson and Göran Wahnström
Solid State Ionics 275 (2015) 2-8

II **Band vs. polaron: vibrational motion and chemical expansion of hydride ions as signatures for the electronic character in oxyhydride barium titanate**
Erik Jedvik Granhed, Anders Lindman, Carin Eklöf-Österberg, Maths Karlsson, Stewart F. Parker and Göran Wahnström
Journal of Materials Chemistry A (2019) **7** 16211

III **The role of oxygen vacancies on the vibrational motions of hydride ions in the oxyhydride of barium titanate**
Carin Eklöf-Österberg, Laura Mazzei, Erik Jedvik Granhed, Göran Wahnström, Reji Nedumkandathil, Ulrich Häussermann, Aleksander Jaworski, Andrew J. Pell, Stewart F. Parker, Niina H. Jalarvo, Lars Börjesson and Maths Karlsson
Submitted to Journal of Materials Chemistry A

IV **Unraveling the ground-state structure of $BaZrO_3$ by neutron scattering experiments and first-principles calculations**
Adrien Perrichon, Erik Jedvik Granhed, Giovanni Romanelli, Andrea Piovano, Anders Lindman, Per Hyldgaard, Göran Wahnström and Maths Karlsson
Submitted to Chemistry of Materials

V **$BaZrO_3$ stability under pressure: the role of non-local exchange and correlation**
Erik Jedvik Granhed, Göran Wahnström and Per Hyldgaard
To be submitted

Specification of the authors contribution to the publications:

I The author performed the theoretical modelling, all DFT calculations and wrote the first draft of the paper.

II The author performed all calculations of the theory part and was the main author.

III The author performed all first-principles calculations and co-authored the paper. The analysis was performed jointly.

IV The author performed all first-principles calculations and wrote the corresponding sections.

V The author performed all calculations and was the main author.

Contents

1

Introduction

Materials modelling has become an integral part of materials development and is now routinely used in the development of new materials. Methods like the CALPHAD approach based on thermodynamic modelling, classical Molecular Dynamics (MD) simulations and Monte Carlo (MC) techniques based on empirical potentials have long been used to guide materials development. Properly conducted, materials modelling makes it possible to predict properties of materials not yet synthesised. While the CALPHAD approach is a continuum theory, both MD and MC are atomic simulation techniques which give the user a “microscope” of atomic resolution in all three dimensions. If the calculated prediction matches the experimental results it is also, at least in principle, possible to trace the microscopic origin of macroscopic phenomena. However, common for both the thermodynamic modelling or the empirical potentials mentioned above is that input is often taken from experimental data, and that the output will be limited by the quality of the input data. Some predictions may turn out trivial if the method has been designed to predict it, or worse unreliable and even false if the model has not been designed to be able to capture it. Some phenomena are even impossible to model with these methods when the behaviour is of strict quantum origin.

It is also possible that the phenomenon we are trying to model is predicted to the correct numbers for the wrong reason, that the model produces the correct results because it was designed to, not because there is any underlying fundamental physics behind it. Therefore, we would prefer our model to contain as few parameters as possible, parameters which have to be fitted to some kind of experiment. Indeed, we want our model to contain no parameters at all if possible.

Several of the more challenging prototypical problems for materials theory are found in perovskites. Perovskite is a class of materials which share the basic perovskite crystal structure and the general chemical formula ABX_3, but with few limitations in the constituent elements. Due to the vast number of perovskites this class of material is very versatile and exhibits very large variety of properties, including a plethora of phase transitions. Many of these phase transitions can be categorised as octahedral tilts or cation displacements. The latter can cause the formation of ferroelectric phases, such as in $BaTiO_3$ the first perovskite with a practical application [1–3]. The former leads to anti-ferrodistortive phases such as in the low temperature phase of the prototypical $SrTiO_3$. The energy difference between the phases is usually very small and thermal energy is often enough to stabilize the high symmetry cubic phase. Sometimes even quantum zero point motion is enough to suppress the phase transition.

Victor Goldschmidt [4] was the first to systematically categorise the distortion aptitude for perovskites in the tolerance factor or *Goldschmidt ratio*. The tolerance factor is a measure which relates the ionic radii of the constituent elements and, despite its simplicity, is remarkably accurate at predicting the likelihood of cubic symmetry as well as indicating which type of distortion can be expected otherwise. Although it is but a first rough estimate, two main types of distortions away from the cubic symmetry may be predicted based on the tolerance factor. If the tolerance factor is too high a cation displacement will occur, and if it is too low a more or less rigid rotation, or tilt, of the inscribed octahedron.

The categorisation of perovskites was extended by Mike Glazer [5, 6] who designated the different perovskite derivative crystal structures according to the octahedral tilts. The Glazer notation is a very intuitive and pictorial description of the various lower symmetry structures that the ideal cubic perovskite may transform into by a pure octahedral rotation. Further work on the formal categorisation of perovskites into space groups has been performed by Woodward [7, 8] and Howard and Stokes [9–11]. The latter have also studied cation displacements, which also may be regarded as a function of a continuous order parameter.

One perovskite which seems not to undergo any phase transition is $BaZrO_3$. It is prototypical in the sense that it is one of a select few, perhaps the only non-metallic oxide perovskite, to remain cubic at all temperature [12–17]. Although the absence of phase transitions has been confirmed, at least down to 2 kelvin [12], the phase stability is still under discussion.

Several computational studies [18–22] find an unstable phonon mode at the R-point. This is indicative of an anti-ferrodistortive phase transition, similar to that of $SrTiO_3$. It has been suggested that the absence of experimental evidence is because this phase transition is suppressed by quantum zero point motion [22, 23]. This is in contrast to the several experimental studies [12, 24, 25] which maintain that $BaZrO_3$ will remain cubic all the way down to zero kelvin.

The existence of an anti-ferrodistortive phase transition in $BaZrO_3$ is indeed an example of a challenging materials modelling task, where small differences, in total energy or in some other measurable quantity, e.g., phonon frequencies, can cause a qualitatively different behaviour. It is also a task which is very sensitive to the computational method used and different modelling schemes will predict different behaviours.

Another challenge in materials modelling is to determine the presence or absence of polarons. The oxyhydride $BaTiO_3$, was reported in 2012 [26] and consists of substitutional hydrogen on the oxygen site with ionic charge -1. Conventional band theory predicts oxyhydride $BaTiO_3$ to exhibit metallic conductivity [27], and it has been suggested that the observed semi-conducting behaviour [28] is caused by the presence of polarons [29]. A polaron is a localisation of an electron in real space, as opposed to the state where the electron is completely delocalised in the entire lattice as predicted by conventional band theory. The presence of polarons inhibits electron diffusion and thus conductivity in a material, causing the material to exhibit semi-conducting rather than metallic conductivity. Hole polarons in perovskites have been modelled [30–32] and found to be stable in $BaZrO_3$, $SrTiO_3$ and $BaTiO_3$. Electron polarons seem to be unstable and unlikely to form [29]. However, the conductivity in oxyhydride $BaTiO_3$ is reported to be semi-conducting at low hydrogen concentrations [28].

Modelling of polarons is difficult for many reasons. First of all, it is a phenomenon of quantum nature which requires solution of the electronic-structure problem by means of an electronic structure program. Secondly, it's a phenomenon which might easily be overlooked by a "naive" approach. In addition, the exact ground state structure of $BaZrO_3$ is difficult to determine, and different computational schemes or approximations will yield different results, not only quantitatively but also qualitatively. The only path forward is effectively through a co-called first-principle method.

In this thesis *"First principle"* will be used to denote methods for solving the electronic structure problem which can be directly derived from the (non-relativistic) many-body Schrödinger equation without input from experimental quantities such as cohesive energies, bond lengths or band-gaps. First-principles materials modelling includes wavefunction based methods, such as Hartree-Fock (HF) method, as well as standard density functional theory (DFT). It also includes so-called hybrid formulations, mixing the HF and standard DFT formulations. However, it does not include thermodynamic modelling based on empirical potentials.

The great advantage of first principles methods is that they do not require prior knowledge about the specific system under investigation. In other words, a first principle method does not contain parameters which depend on the specific system which need to be provided from experimental results or heuristic experience. A true first principles method should also be transferable, i.e., if it works for one system it should work also for similar, or even vastly different, systems. This does not mean that computational techniques do not require a certain degree of craftsmanship for producing proper results. Indeed, as this thesis will show, a certain degree of know-how is essential for taking full advantage of the predictive power.

Since the seminal papers in 1964 by Hohenberg and Kohn [33] and 1965 by Kohn and Sham [34] DFT has emerged as the first principles method of choice for modern computational materials modelling, with the number of published articles growing almost exponentially [35, 36]. Experimental results are almost routinely supported by DFT calculations. The popularity of DFT is to a large extent due to two factors: 1) the beauty of the theory and, for practical calculations, also 2) the favourable trade-off between accuracy and computational cost. DFT can, at the same computational cost, treat much larger systems than typical wavefunction based methods [37]. In the present thesis differences in speed of up to a factor 500 has been noted for a 40 atom system. Also the memory requirement for a wavefunction based calculation is higher. Not only do we need to store the set of parameters needed to represent the wavefunction in all three cartesian direction, we need to store this information for all orbitals and all atoms in the system. For large systems or heavy atoms, this rapidly becomes a daunting task. The advantage of DFT is that only one scalar property needs to be stored, namely the electron density.

In principle, DFT is an exact theory. However, practical implementations of DFT relies on approximations to the true functional, which remains intractable. The strength of the Kohn-Sham DFT is that the functional is separated into terms which are easily computed. The approximations are found in the exchange-correlation (xc) functional the energy of which is only a fraction of the total [38]. DFT can therefore give decent results even at rather simple xc-functional approximations.

The local density approximation (LDA), which is regarded as the simplest approximation to the xc-functional, has been extended to higher rungs by including higher orders of density gradients in the families of functionals called the generalised gradient approximation (GGA) and meta-GGA. Since these latter functionals depend not only on the electron density at a specific point but at its neighbourhood, these functionals are often denoted semi-local.

Beyond the GGA, non-local correlation functionals offer an approach to systematically include van der Waals interaction, especially in sparse matter where van der Waals forces are significant [39]. This class of functionals are truly non-local, meaning that their impact on any given point, in principle, also depends on the electron density far away.

Another approach to increasing the accuracy of the xc-functional approximation, is the combination of standard DFT and a wavefunction description adapted from the Hartree-Fock method. This class of functionals are termed hybrids and are popular in the chemistry community and have more recently found widespread use also in the solid state community. As noted by Kohn and Sham [34] “This procedure may be regarded as a Hartree-Fock method corrected for correlation effects.” This class of methods, which goes under the name of hybrid functionals, is a pragmatic approach which combines the benefits of DFT with those of Hartree-Fock. Hybrids are sometimes discussed as not being DFT in the purest of definitions [40], because the exchange depends on the wavefunctions. However, in DFT, the solution wavefunctions are also formally functionals of the density, and so, therefore is the exchange term in the hybrid description [41]. The essential difference between hybrid and standard DFT formulations (like LDA, GGA, meta-GGA and vdW-DF), is that hybrids can not be seen as having an explicit density dependence in their description of exchange and correlation effects. For practical implementations, the suggestion of Kohn and Sham was modified by Becke [42–44] and was soon to be followed by several others [45–50].

Today, a plethora of different functionals have been proposed. In principle there are two different approaches for how to design functionals. Either the underlying parameters can be subjected to a fitting procedure against available experimental data, or it can be determined from theoretical considerations based on known theoretical constraints [45, 51–63]. The previous has the obvious advantage that it produces very accurate values for the materials and properties for which it has been designed, but may be unreliable for other materials or other properties. The latter exhibit a higher degree of transferability between different systems and properties and can hence be termed more predictive.

The assessment of functionals follows similar divides. Functionals can be assessed based on how well a certain property, or set of properties, in one material or set of materials is predicted. The “best” functional is then defined as the functional which makes the best prediction of the desired properties in the investigated materials. The obvious drawback with this approach is that transferability is not guaranteed and that assessment becomes impossible if there are no available measurements of a certain property. Also, there is no guarantee that the underlying mechanism (having the correct electron density) is correct simply because a given observable (e.g., the correct total energy) is accurately predicted for a selection of problems [64].

The other way to asses a functional is by determining to what degree the functional satisfies the known theoretical constraints, such as the reduction to the uniform electron gas limit [51], the conservation of the exchange-correlation hole [51, 52], the exchange scaling relation [53, 54] and the spin-exchange scaling. An overall goal is that the functional approximation delivers DFT solutions that reproduces the correct electron density [64], the fundamental quantity in DFT.

Another criterion, which the xc-functionals should satisfy is the piecewise-linearity criterion [56, 65, 66], that reflects the so called derivative discontinuity of the xc-functional at integer particle number. This criterion is not satisfied for either the GGA or the wavefunction based Hartree-Fock, although they err in different directions [65–67]. This can be taken as a rationale for mixing of DFT with Fock exchange or for adding a Hubbard like U term [68, 69]. The Hubbard like U term is an on-cite repulsion term added to account for the self-interaction error in DFT and is often used in perovskite systems to account for Mott transitions and Jahn-Teller distortions in “strongly correlated” systems. Often, the U term is fitted to some experimentally determined observable, such as the band-gap or the position of the d state in the band structure.

In the spirit of ‘first principle’ this theses advocates the use of *parameter free, constraint based functionals*, or computational schemes where the parameters can be determined self-consistently without prior knowledge of the investigated system. The benefit is an expected improvement in transferability implied by not relying on experimental measurements, but also, as mentioned above, the higher reliability in reflecting the underlying mechanisms.

All predictions performed within a theoretical framework must be tested against observations. This is true even when not relying on experimental input in the development of functionals. A successful theoretical description is that which is corroborated by experimental evidence. While no single experimental result can be treated as the complete answer, the combination of several measurement using different experimental techniques and theoretical first principles modelling can give a deeper understanding of a material or a phenomenon which in turn can spur a technological advancement or an advancement in the field of science.

This thesis investigates and describes several prototypical cases which early use of DFT with explicit LDA or GGA xc-functionals has failed to describe correctly. It will be shown that the vibrational frequencies, and properties derived from these, are very sensitive discriminators. The vibrational frequencies are both difficult to compute accurately, show a large variation between the different functionals and have large implications on the predicted stability of the material state. By comparing the calculated vibrational frequencies to experimental results, we can accurately determine the material state. We can assert the performance of the different functionals for material phases and properties that must be seen as exceptionally sentitive to details of the predicted density variations. Specifically, this thesis investigates which elements of the xc-correlation functional are most crucial for an accurate description of these properties, non-local exchange or non-local correlation. The thesis concludes that inclusion of non-local exchange is of primary importance for an accurate description of the investigated materials and material states, and that non-local correlation effects are, although non-negligible, of lesser importance in $BaZrO_3$. Again, the indirect validation of the accuracy of the electron-density description is valuable since the density variation is the core quantity in DFT.

This thesis also proposes solutions to several materials problems. The size and shape of the oxygen vacancy and the hydroxide ion in barium zirconate are described and given a theoretical framework, and the predicted chemical expansion is found to be well in line with experiments. The existence of oxyhydride BTO is confirmed through a combination of neutron scattering measurements and first-principles calculations, and the conduction state is proposed to be metallic-like. It is shown that the presence of a large number of vacancies do not dramatically affect the local environment of the hydride ion or the conduction state.

Furthermore, this thesis shows that $BaZrO_3$ is indeed cubic all the way down to absolute zero. The discrepancies found by previous computational works are due to the xc-functional used.

Finally, this thesis makes a prediction for the phase transition pressure at zero kelvin for the anti-ferrodistortive phase transition in $BaZrO_3$.

2

The perovskite structure

> “ Perowskit, ein neues Mineral, das ich im Sommer 1839 von Herrn Ober-Bergmeister Kämmerer erhalten und in einer früheren Beschreibung desselben zu Ehren des Vizepräsidenten Herrn von Perowski in Petersburg zu benennen vorgeschlagen habe.[1] ”
>
> – Gustav Rose [70]

Perovskite is a mineral named after the Russian mineralogist Count Lev Perovski [70]. It is composed of calcium titanate ($CaTiO_3$) in a very distinctive crystal structure which is shared by many other compounds. As with many minerals, Perovskite has given its name to this class of materials, called *perovskites*, exhibiting the perovskite structure. We will adopt this terminology of calling a material exhibiting the perovskite structure a *perovskite*.

Perovskites are rather extensively studied due to the abundance of properties exhibited by different perovskites in combination with their rather simple crystal structure. Bhalla *et al.* [3] even claim it is “the single most versatile ceramic host”. Among the properties exhibited by perovskites are high dielectric constant [71], ferro- and anti-ferro-electricity [72], piezoelectricity [73], magnetoresistance [74,75], thermoelectricity [76], superconductivity [77, 78], oxygen ion conduction [79] and last but not least proton conductivity [80].

---

[1] Perovskite, a novel mineral, which I received in the summer of 1839 from Herr Ober-Bergmeister Kämmerer and which I, in an earlier description of it, proposed to name in honor of the Vice-President Herr von Perowski in Petersburg.

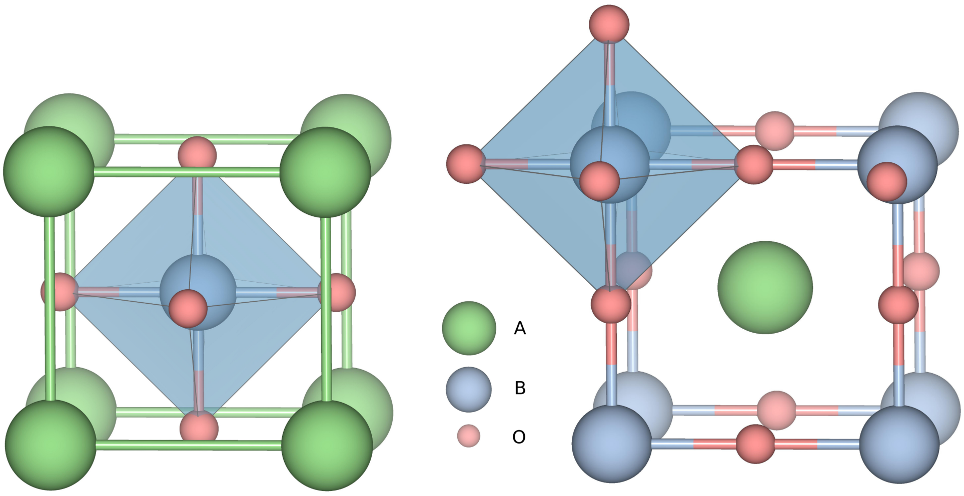

Figure 2.1: The cubic crystal structure of the ideal perovskite with symmetry Pm$\bar{3}$m with the conventional A-atom centred representation (left) and the B-atom centred representation (right). The inscribed oxygen octahedron is marked with blue.

2.1 Ideal crystal structure

A perovskite has the general formula ABX_3, where the cations A and B span the periodic table and the anion, X, typically is a chalcogen or halogen. For the material to be charge balanced the charge sum of the cations must equal three times the charge of X, $(q_A + q_B = -3q_X)$. For an oxide perovskite, $q_X = +2$, the charges of the A and B atoms may be obtained either as 1+5, 2+4 or 3+3. This limited restriction on the valency of the A and B atoms leads to an abundance of perovskites [1, 2] Many more structures can also be constructed by alloying on the A or B site.

The ideal perovskite structure, the aristotype, is simple cubic with symmetry $Pm\bar{3}m$. There are two different, but equivalent representations of the atoms in the unit cell. In the standard representation the A cations is chosen as the origin (0,0,0) with the B atoms in the body centre $(1/2, 1/2, 1/2)$. The X atoms are then located on the face centres, $(1/2, 1/2, 0)$ with cyclic permutations. This is shown in Figure 2.1. The Wyckoff sites for these positions are $1a$, $1b$ and $3c$. A crystallographically equivalent representation can be obtained by shifting the origin of the point group to the B site. The X atoms are then found at (1/2,0,0) with cyclic permutations. The Wyckoff sites for these positions are $1a$, $1b$ and $3d$. The choice of origin has little implication for the most purposes, but it affects the nomenclature for the irreducible representations. For example, the irreducible representation (often abbreviated irrep) R_{25} in the standard or A-atom centred representation is equivalent to R'_{15}

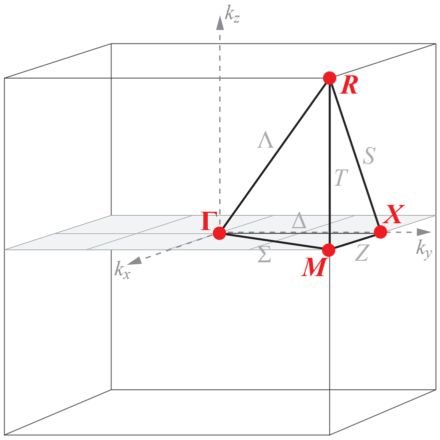

Figure 2.2: The Brillouin zone of the cubic perovskite.

in the B-atom centred representation. In this thesis the standard representation is used.

A very important representation of a crystal is the *reciprocal* cell. The reciprocal cell is the Fourier transform of the real space (primitive) unit cell. It is a mathematical construction in which both electronic and vibrational properties of a crystal can be calculated and visualised. The reciprocal unit cell, also known as the Brillouin zone, of a simple cubic lattice, such as the perovskite structure, is also simple cubic and shown in Figure 2.2. Due to the symmetries of the cube it is customary to specify the properties only at certain points, the high symmetry points, and along the lines connecting them. In Figure 2.2 the high symmetry points Γ, X, M and R corresponding to the points (0,0,0), (0,0,½), (0,½, ½) and (½, ½, ½) are shown.

2.2 Distorted crystal structures

Very few perovskites exhibit the ideal cubic structure [1, 2]. In fact, not even $CaTiO_3$, the perovskite mineral itself, is truly cubic. Since most perovskites are considered to be ionic, the ions building up the crystal can, to a first approximation, be regarded as hard spheres with ionic radii R. For such a model, the lattice constant, as measured along the B–O–B axis, equals $a = 2R_\mathrm{A} + 2R_\mathrm{O}$ or if measured along the face diagonal $\sqrt{2}a = 2R_\mathrm{B} + 2R_\mathrm{O}$. Due to the differences in ionic radii these two measures lead to different lattice constant, and the discrepancy is accommodated for in the *tolerance factor* or Goldschmidt ratio [4]

$$t = \frac{R_\mathrm{A} + R_\mathrm{O}}{\sqrt{2}\,(R_\mathrm{B} + R_\mathrm{O})} \tag{2.1}$$

A tolerance factor close to 1 often implies cubic structure [81] while a tolerance factor lower than unity in general implies distortions into structures of lower symmetry, usually tetragonal or orthorhombic. With the ionic radii defined by Shannon [82] the tolerance factor is 1.002 for $SrTiO_3$, which is indeed cubic at room temperature [83]. However, although $CaTiO_3$ has a tolerance factor of 0.97, which is near unity, it is orthorhombic at room temperature. Tolerance factors larger than unity also cause distortions, generally towards hexagonal close-packed structure [1]. $BaTiO_3$, which has a tolerance factor of 1.06, distorts into a tetragonal symmetry and it is not until at a temperature of 120°C that $BaTiO_3$ becomes cubic. Several lower symmetry crystal structures are described in further detail in Section A.

Although the tolerance factor may serve as a first guide to the crystal structure of a perovskite it is but a rough estimate. Even $SrTiO_3$, which is cubic at room temperature and has a tolerance factor close to 1 undergoes a phase transition when cooled below 105 K [84].

2.3 Tilts and instabilities

For an understanding of phase transitions and various derivative structures of the ideal perovskite it is often convenient to think of the perovskite as built up of corner-sharing BX_6 octahedra. The phase transition of $SrTiO_3$ at 105 K can be described by a rotation, or tilt, of the inscribed BX_6 octahedron about the pseudo-cubic axes. The octahedron, illustrated in Figure 2.1, is regarded as rigid and a rotation leaves the B-atom centred in the cage, but does not disrupt its corner sharing connectivity. The tilts can be designated according to Glazer [5, 6] by the rotations along the three Cartesian coordinates axes, which coincide with the basis vectors. Since rotations do not commute this is an approximation which works reasonably for small angles. General, unequal, rotations about the axes x, y and z are denoted by a, b and c with a superscript $+$ indicating tilts in successive layers in the same direction, i.e. in-phase rotation, and $-$ in opposite directions, i.e. out-of-phase rotation. A zero superscript indicates no rotation. Thus a rotation $a^+b^+c^+$ indicates three unequal rotations about the axes x, y and z, with the octahedra along the axes tilted the same way.

The phase transition exhibited by $SrTiO_3$ at 105 K is a $a^0a^0c^-$ tilt, indicating a rotation about the z-axis with successive layers in opposite directions. This is illustrated in Figure 2.3b. In order to leave the oxygen octahedra rigid the lattice constants must change during a tilt, and for the rotation around the z-axis the lattice constant in the x and y direction decrease by an equal amount leading to a tetragonal $I4/mcm$ symmetry.

The distortion in $BaTiO_3$ differs from the octahedral tilting mentioned above insofar as that the A and B-cations are displaced relative to the polyhedral centres of

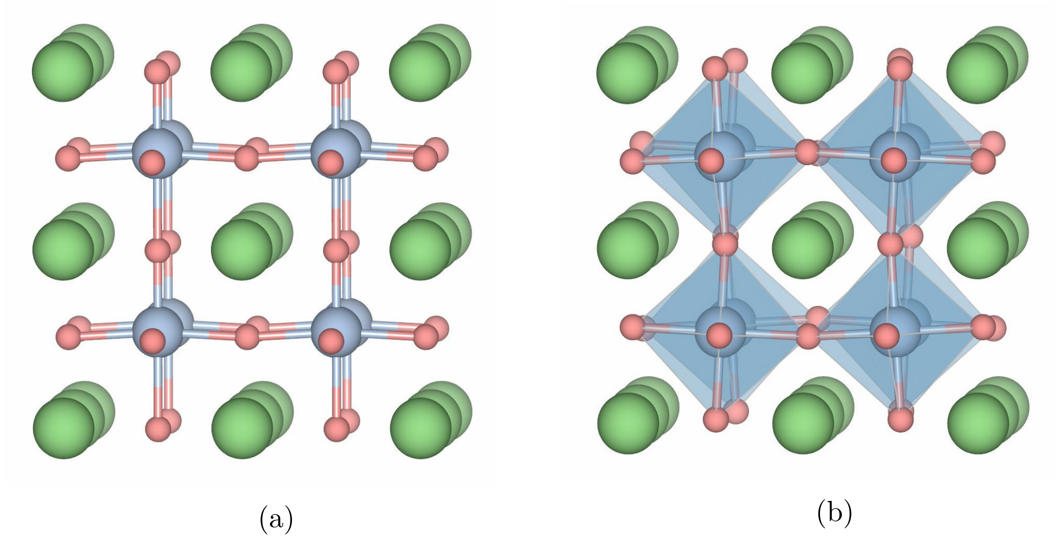
(a) (b)

Figure 2.3: (a) The ferrodistortive phase of $BaTiO_3$ with tetragonal $P4mm$ symmetry and (b) the $a^0a^0c^-$ anti-ferrodistortive phase of $SrTiO_3$ with tetragonal $I4/mcm$ symmetry.

coordination. This causes a permanent electric dipole moment, which is the cause of the ferroelectricity exhibited by $BaTiO_3$. Often this cation displacement is accompanied by an octahedral tilt and $BaTiO_3$ stand out as an example where this is not the case. There are three possible directions for the B-cation displacement; along the [100] direction, the [110] direction and the [111] direction. These displacements cause distortions into crystals of tetragonal, orthorhombic and rhombohedral symmetry, respectively [85]. $BaTiO_3$ is important because it exhibits all these three phases and is therefore sometimes considered as the prototypical ferroelectric [86].

The tilt exhibited by $SrTiO_3$ also carries a local dipole moment which is out-of-phase from one unit cell to the next. This phase is termed anti-ferrodistortive.

2.4 The BZO balancing act

It has been hypothesised in theoretical works that $BaZrO_3$ undergoes an anti-ferrodistortive phase transition similar to that of $SrTiO_3$ [18–22]. This has not been confirmed in experimental works which report $BaZrO_3$ to be cubic, at least down to 2 kelvin [12]. It has been suggested that the absence of experimental evidence is because the phase transition is suppressed by quantum fluctuations [22, 23]. This is contrasted by other experimental studies [12, 24, 25] which claim that $BaZrO_3$ will remain cubic also in the classical regime.

To complicate things further, there are a set of experimental measurements which have been interpreted as indications of a phase transition by theoretical calculations. The “anomalously high Debye–Waller factor” for the Ba–O bonds in EXAFS measurements is attributed to an anti-ferrodistortive tilt [18]. Also the calculated dielectric constant computed with GGA in the tetragonal cell fits the experimental results much better than the values calculated within a cubic cell [19]. Further indications of a possible phase transition is the measured Raman spectrum which shows some features not compatible with a perfectly cubic perovskite in some studies [25, 87] but not in other [13, 14, 88]. It has been suggested that the existence of peaks in the Raman spectrum is due to dynamical disorder [14, 87, 88], but it cannot be ruled out that these features appear due to impurities. It has also been suggested that the forbidden Raman peaks are due to second-order Raman scattering [89]. The earlier experiments are not conclusive.

Although no phase transition has been seen as a function of temperature, a phase transition has been reported at room temperature and an elevated pressure of 17.2 GPa to a tetragonal phase [17]. It is hypothesised, based on previous computational works, that the high pressure phase is the tetragonal $I4/mcm$ symmetry, a hypothesis which is supported by Rietweld refinements performed by the same authors. No further phase transitions were reported up to a pressure of 46.4 GPa. This pressure induced phase transition might be seen as support for the cubic ground state structure of $BaZrO_3$, but measurements of the phase transition pressure at different temperatures are lacking. The phase transition pressure is addressed in **Paper V**.

3

Points defects in $BaZrO_3$ and $BaTiO_3$

> “ Crystals are like people, it is the defects in them which tend to make them interesting ”
>
> – Colin Humphreys [90]

3.1 Point defects

In addition to the structural instabilities discussed above, all real materials contain defects, including point defects such as vacancies and interstitials, line defects such as dislocations and plane defects such as grain boundaries. In this thesis the focus is on three types of point defects; interstitials, vacancies and substitutional defects. These are illustrated schematically in Figure 3.1. A point defect is a non-stoichiometric perturbation of the ideal lattice which may or may not be electrically charged. Point defects cause an increase of the configurational entropy contribution to the free energy at non-zero temperatures and will therefore always be present. Materials can also be prepared in such a way as to increase the number of defects. This is referred to as doping and is performed, e.g., to make $BaZrO_3$ proton conducting.

By substituting a tetravalent zirconium ion with a trivalent ion, such as yttrium, a *substitutional* defect is created. In Kröger-Vink notation, which is often used in defect chemistry, this is written as Y'_{Zr}, where Y denotes yttrium and the subscript Zr indicates the host site. While zirconium donates four electrons to the lattice making the zirconium ion charged +4, yttrium donates only three and the yttrium

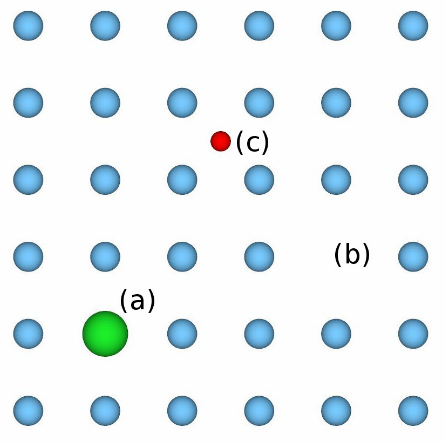

Figure 3.1: Schematic illustration of (a) a substitutional defect (b) a vacancy and (c) an interstitial.

ion is charged +3. Since the defect charge is given relative to the original site in Kröger-Vink notation the apostrophe indicates a defect charge of −1.

A *vacancy* is formed by removal of an atom, e.g., an oxygen atom. Since the oxygen ion has a charged of −2 the defect left behind after removal of an oxygen atom will be $v_O^{\bullet\bullet}$ in Kröger-Vink notation, where v indicates a vacancy[1], the subscript O indicates the oxygen host site and the defect charge of +2 is denoted by two dots. Thus the combination of, e.g., two yttrium substitutional defects and one oxygen vacancy makes the material charge neutral. Alloying with substitutional defects in this manner is usually referred to as acceptor doping due to the similarities to semiconductor doping.

An *interstitial* is an ion situated between ideal lattice sites. An interstitial can be of any type, including those already found in the host, and is denoted by an index i. A proton (H^+) interstitial would for example be denoted $H_i^{\bullet}$, where the dot denotes the positive charge of the proton. The proton studied in **Paper I** however, is so closely bound to the nearest neighbour oxygen that the notation $(OH)_O^{\bullet}$ is more appropriate.

It is often necessary to include a non-defect site in chemical reaction formulas. The notation for an ideal site is written $O_O^{\times}$, which is an oxygen on an oxygen site with neutral charge.

---

[1] Vacancies are often denoted with an upper-case V. Here we adhere to the convention of using lower-case to avoid confusion with a substitutional vanadium. Similarly a lower-case i is used to denote the interstitial.

3.2 Hydration

In **Paper I** the hydration of a $BaZrO_3$ is studied. Although a small number of vacancies can be present also in undoped $BaZrO_3$ a higher concentration of vacancies is made possible by the presence of acceptor doping, such as yttrium in $BaZrO_3$. During hydration an oxygen vacancy is filled and two hydroxide ions are formed.

$$H_2O_{(g)} + V_O^{\bullet\bullet} + O_O^{\times} \rightarrow 2(OH)_O^{\bullet} \tag{3.1}$$

The hydrogen atom is rather closely bound to the oxygen but is mobile in the shape of a positively charged proton which diffuses through the material through the Grotthuss mechanism [91] by hopping between lattice sites, making the material proton conducting.

In analogy with the ionic radii of atoms, the vacancy is often described in terms of an ionic radius. This is intrinsically difficult and the modelling of a vacancy as a hard sphere is problematic as the vacancy should rather be modelled as the lack of one. Similarly, the proton can be given an ionic radius. Usually, the radius is not assigned to the proton itself, but to the hydroxide ion. The difference in ionic radius between the vacancy and the hydroxide ion causes a chemical expansion in the lattice when the material is hydrated [92].

The chemical expansion during hydration is a serious problem in applications with mechanical stress and fatigue that can cause micro cracking and deterioration of the material. Therefore, chemical expansion has been investigated, both experimentally [93–95] and theoretically [96–100]. Despite the efforts to understand chemical expansion and thus the size difference between the vacancy and the proton, the size of the vacancy has been debated. The size of the oxygen vacancy is addressed in **Paper I**.

3.3 Anomalous hydrogen species in barium titanate

Hydrogen can also appear as negatively charged hydride ions in, for example oxyhydride phases, where a hydride ion is substituted on an oxygen site, $H_O^{\bullet}$. Oxyhydrides are rather rare in nature and until recently the layered perovskite structured $LaSrCoO_3H_{0.7}$ and $SrCo_2O_{4.33}H_{0.84}$ were the only reported transition metal oxides exhibiting higher than defect level amounts [101, 102]. The discovery of the oxyhydride perovskites $(Ca,Sr,Ba)TiO_{3-x}H_x$ was therefore rather unexpected [26, 103]. Among these BTO exhibits the highest amounts of hydrogen, up to $x \lesssim 0.6$.

The formation energy of a substitutional hydride ion is large and positive which implies that oxyhydride BTO is not thermodynamically stable and can form only under strongly reducing conditions provided by, e.g., CaH_2. Nevertheless, it is kinetically stable in air (up to 200°C) and under inert conditions up to 450°C, above which hydrogen gas is released [26]. The lattice constant increases slightly compared to the pristine lattice constant, and a phase transformation occurs from tetragonal to cubic. The substitutional hydride thus stabilises the cubic phase. In addition, oxyhydride BTO is a dark blue-black material, in contrast to white pristine BTO. The origin of the blue colour is not fully understood yet.

The substitutional hydrogen is stable only in the positive charge state ($\mathrm{H}_\mathrm{O}^\bullet$) over the entire range of fermi levels within the bandgap [27, 29]. The formation reaction is thus

$$\tfrac{1}{2}\mathrm{H}_2 + \mathrm{O}_\mathrm{O}^\times \rightarrow \tfrac{1}{2}\mathrm{O}_2 + \mathrm{H}_\mathrm{O}^\bullet + \mathrm{e}' \tag{3.2}$$

Therefore, it acts as a shallow donor contributing to n-type conductivity in the initially empty Ti $3d$ band. Conductivity measurements confirm that $\mathrm{BaTiO}_{3-x}\mathrm{H}_x$ is electrically conducting [26, 28]. However, while $\mathrm{SrTiO}_{3-x}\mathrm{H}_x$ exhibits metallic-like conductivity over the whole concentration range, $\mathrm{BaTiO}_{3-x}\mathrm{H}_x$ exhibits semiconductor-like conductivity at lower concentrations. At $x = 0.14$ the conductivity in epitaxial thin films is semiconductor-like for all temperatures, at $x = 0.24$ a semiconductor to metal transition occurs at 200 K, and at higher concentrations the conductivity is metallic for all temperatures [28]. This semiconductor-like conductivity has been attributed to the presence of small electron polarons forming a localised defect level in the bandgap [29].

3.4 The polaron quasi-particle

A band-state electron (or hole), i.e., an electron inside an allowed energy band, moves freely in the crystal with an effective mass m^*, which differs from the electron mass in vacuum m_e [104, 105]. Band theory follows from solving the electronic Hamiltonian in an assumed rigid lattice. In real materials the ions are mobile and at least in an ionic material an electron can polarise the lattice in its neighbourhood and localise. The combination of a localised, self-trapped electron with its accompanying lattice distortions can be treated as a quasi-particle called *polaron* [106–108].

If the extent of the polaron is large compared to the lattice spacing, the polaron is called Fröhlich or large polaron [106]. In this long wavelength limit the solid is treated in a continuum approximation in the adiabatic limit and the polaron moves around in the lattice with an increased effective mass compared to a bandstate electron.

A polaron with a radius for the lattice distortion of the order of the lattice spacing is called a small polaron and the charge carrier is often localised to a single atomic site. Figure 3.2 shows an example of a small polaron where the charge is localised almost entirely to one atom. Because of the short range of the small polarons the Fröhlich continuum theory is not applicable. The description of small polarons are on the other hand accessible through first-principle calculations. The

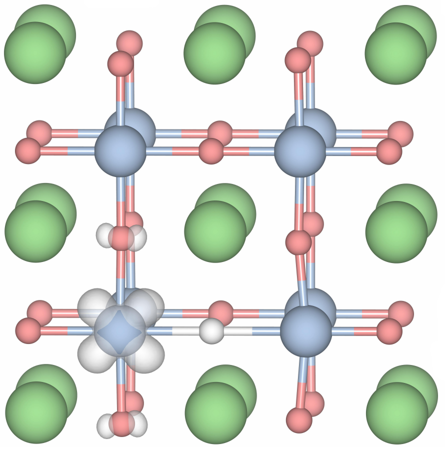

Figure 3.2: The polaron state of the oxyhydride phase of $BaTiO_{3-x}H_x$ with a substitutional hydrogen on an oxygen site. The electron density of the polaron is shown as a white isosurface.

small polaron can be described in a way similar to a substitutional point defect and diffuses through the material through hopping between lattice sites [105].

The formation of a polaron from a delocalised bandstate electron is associated with an energy cost for the polarisation of the lattice. The energy gain by localising the electron must therefore be larger than the energy cost of the lattice polarisation to promote the the formation of a polaron. Figure 3.3 shows a schematic illustration of the energy as a function of lattice distortion. The formation energy E_{pol} is defined as the total energy difference between the relaxed polaronic and delocalised states, and is a combination of the strain energy required to distort the lattice E_{st} and the electronic energy gained by localising the electron in the distorted lattice, E_{el}.

3.5 Polarons in BTO?

Hole polarons in perovskites have been modelled [30–32] and found to be stable in $BaZrO_3$,$SrTiO_3$ and $BaTiO_3$. In addition, small self trapped electron polarons have been found in rutile TiO_2 (although not in anatase) both theoretically [109–112] and experimentally [112–114]. The similarities between the electronic structure of $BaTiO_3$ and TiO_2 near the band edge can be interpreted as a suggestion that self-trapped polarons may be present also in BTO. However, electron polarons seem to be unstable and unlikely to form in $BaTiO_3$ [29].

In some cases the strain energy is too large compared to the electronic energy gain for the polaron to be favourable. Under such circumstances self-trapped electron polarons will not form. This is believed to be the case in pristine $BaTiO_3$ [29]. A

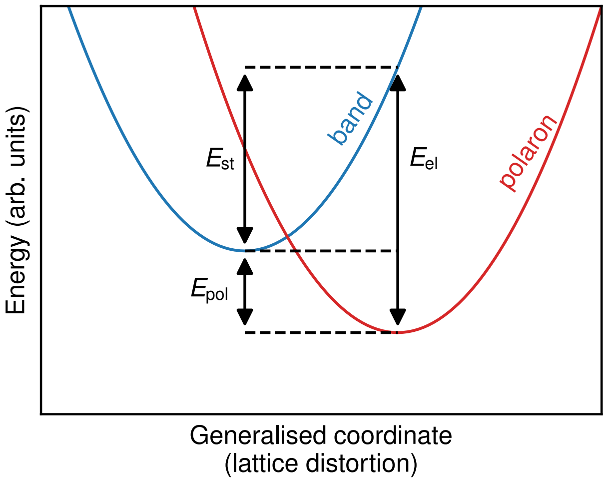

Figure 3.3: Schematic illustration showing the polaronic (E_{pol}), lattice strain (E_{st}), and electronic (E_{el}) energies as a function of lattice distortion for the delocalised bandstate and the localised polaron state

polaron can still form if strain can be induced by other means, e.g. by a charged point defect which attracts the polaron. The strain induced by the point defect lowers the strain energy required to form the polaron and a *bound polaron* is created. Bound polarons have been discussed in BTO in connection with n-type doping such as Nb^{+5} substitution and oxygen vacancies [115, 116]. It is therefore plausible to assume that bound polarons could exist on the titanium ion in oxyhydride BTO where the natural associate defect site is the n-type $H_O^\bullet$ defect [29].

The conductivity in oxyhydride $BaTiO_3$ is reported to be semi-conducting at low hydrogen concentrations [28]. Conventional band theory predicts oxyhydride $BaTiO_3$ to exhibit metallic conductivity [27], and it has been suggested that the semi-conducting behaviour is caused by the presence of polarons [29].

Detection of polarons has proven a challenging task, both experimentally and theoretically. Due to the very short range of the lattice distortion, polarons cannot be seen from X-ray diffraction. Also the theoretical modelling of polarons in oxides has proven challenging. Density functional theory with local and semi-local xc-functionals suffers from the well known self-interaction error [55] which favours delocalisation of the electron and thus cannot properly describe charge localisation such as polarons. **Paper II** presents a method for polaron description from first-principles calculations and how to characterise the bandstate from the polaron state combining vibrational analysis based on density functional theory calculations with inelastic neutron scattering experiments.

4

Electronic structure calculations

> “ The underlying physical laws necessary for the mathematical theory of a large part of physics and the whole of chemistry are thus completely known, and the difficulty is only that the exact application of these laws leads to equations much too complicated to be soluble. It therefore becomes desirable that approximate practical methods of applying quantum mechanics should be developed, which can lead to an explanation of the main features of complex atomic systems without too much computation. ”
>
> – Paul Dirac [117]

The present thesis uses so-called first principles or *ab initio* methods to compute relevant quantities. At the core of first principles calculations is the absence of experimentally fitted parameters. All derived and computed quantities should be obtained from first principles, i.e. from the fundamental description of the nature, the Schrödinger equation. The full time-independent Schrödinger equation in its most compact form reads

$$\mathcal{H}\Psi\left(\mathbf{x},\mathbf{R}\right) = E\Psi\left(\mathbf{x},\mathbf{R}\right) \tag{4.1}$$

where $\mathcal{H}$ is the Hamiltonian, Ψ is the (multi-particle) wavefunction, E is the energy eigenvalues, $\mathbf{R}$ are the positions of the ions and $\mathbf{x}$ the position and spin of the electrons. Almost all first-principles calculations rely on the separation of the full Hamiltonian into an electronic Hamiltonian and an ionic Hamiltonian. The justification for this is the almost instantaneous electronic response to an ionic displacement due to the much lower mass of the electrons. The instantaneous response implies that, as far as electron degrees of freedom are concerned, the ionic position can be treated parametrically. The nuclei are simply assumed to be classical particles (of essentially infinite mass) that only reacts to the electrostatic forces produced by the other nuclei and the electrons. This is called the Born-Oppenheimer or *Adiabatic Approximation.*

After a justification of the adiabatic approximation, the present chapter gives an overview of the methods used for solving the electronic structure problem [36, 37, 44, 118–122]. The ionic motion is treated in Chapter 5.

4.1 Separating electronic and ionic degrees of freedom

For a multi-particle system the full Hamiltonian[1] reads

$$\begin{aligned}\mathcal{H} = -\sum_{i=1}^{N}\frac{\nabla_i^2}{2} - \sum_{k=1}^{K}\frac{\nabla_k^2}{2M_k} + \frac{1}{2}\sum_{\substack{i,j=1\\ i\neq j}}^{N}\frac{1}{|\mathbf{r}_i-\mathbf{r}_j|}\\ -\sum_{k=1}^{K}\sum_{i=1}^{N}\frac{Z_k}{|\mathbf{r}_i-\mathbf{R}_k|} + \frac{1}{2}\sum_{\substack{k,k'=1\\ k\neq k'}}^{K}\frac{Z_kZ_{k'}}{|\mathbf{R}_k-\mathbf{R}_{k'}|}\end{aligned} \tag{4.2}$$

where upper case denotes ionic and lower case electronic quantities. The terms represent in order, the kinetic energy for the electrons and nuclei (with mass M_k), the interaction between electrons, between electrons and nuclei and between the nuclei.

With the electronic Hamiltonian in the Born-Oppenheimer approximation defined as

$$\mathcal{H}_{el} = \sum_i\left[-\frac{\nabla_i^2}{2} + V_{ext}(\mathbf{r}_i)\right] + \frac{1}{2}\sum_{i\neq j}\frac{1}{|\mathbf{r}_i-\mathbf{r}_j|} \tag{4.3}$$

where

$$V_{ext}(\mathbf{r}_i) = -\sum_k\frac{Z_k}{|\mathbf{r}_i-\mathbf{R}_k|} \tag{4.4}$$

is the external potential caused by the ions, the Schrödinger equation for the electrons with the ions at fixed positions $\mathbf{R}$ can be written

$$\mathcal{H}_{el}\psi_{\mathbf{R}}(\mathbf{r}) = \varepsilon_{\mathbf{R}}\psi_{\mathbf{R}}(\mathbf{r}) \tag{4.5}$$

The solution to the electronic Hamiltonian will be discussed in this chapter.

---

[1] In atomic units in which $\hbar = e = m_e = 1/(4\pi\varepsilon_0) = 1$.

The remaining terms in the full Hamiltonian in Equation (4.2) form in the ionic Hamiltonian

$$\mathcal{H}_{ion} = -\sum_k \frac{\nabla_k^2}{2M_k} + V(\mathbf{R}) \tag{4.6}$$

where $V(\mathbf{R})$ is the potential created by the combination of the repulsive ionic potential and the electron-density variation. This is treated in Section 5.

Even when applying the adiabatic approximation the multi-electron Schrödinger equation in Equation (4.5) is quite intractable. Several methods for solving the electronic structure problem have been utilised over the years [36, 44]. The intuitively most accessible are perhaps the Hartree and the Hartree-Fock (HF) approximations. These are also the foundation for understanding notions such as the Hartree potential, self-interaction error and Fock exchange, which are used in hybrid functionals in DFT. In addition, several conclusions and technical aspects carry over to DFT.

4.2 The Hartree and Hartree-Fock approximations

A first approximation to the electronic structure problem can be made by approximating the full wave function with the product of single particle wave functions $\Psi(\mathbf{x}_1, \mathbf{x}_2, ...\mathbf{x}_N) = \psi_1(\mathbf{x}_1)\psi_2(\mathbf{x}_2)...\psi_N(\mathbf{x}_N)$, where ψ_i are one particle wave functions and $\mathbf{x}_i = \mathbf{x}_i(\mathbf{r}_i, \sigma_i)$ denotes the position $\mathbf{r}_i$ and the spin σ_i. This is referred to as the Hartree approximation. In the Hartree approximation the electrons are *uncorrelated* in the sense that the probability of finding electron 1 at $\mathbf{x}_1$, electron 2 at $\mathbf{x}_2$ etc. is given by

$$|\Psi(\mathbf{x}_1, \mathbf{x}_2, ...\mathbf{x}_N)|^2 \mathrm{d}\mathbf{x_1}\mathrm{d}\mathbf{x_2}...\mathrm{d}\mathbf{x_N} = |\psi_1(\mathbf{x}_1)|^2\mathrm{d}\mathbf{x_1}|\psi_2(\mathbf{x}_2)|^2\mathrm{d}\mathbf{x_2}...|\psi_N(\mathbf{x}_N)|^2\mathrm{d}\mathbf{x_N} \tag{4.7}$$

is the product of the probability of finding electron 1 at $\mathbf{x}_1$, electron 2 at $\mathbf{x}_2$ etc.

The single particle wave functions are optimised using the variational principle. By the variational principle the expectation value of the Hamiltonian is always higher than the true ground state energy

$$E_0 \leq \frac{\langle\Psi|\,\mathcal{H}\,|\Psi\rangle}{\langle\Psi|\Psi\rangle} \tag{4.8}$$

for any wave function Ψ, with equality for the true ground state $|\Psi_0\rangle$. The ground state is obtained by minimising the energy with respect to the wavefunction Ψ subject to the constraint

$$\int \mathrm{d}\mathbf{x}\, n(\mathbf{x}) = \int \mathrm{d}\mathbf{x} \sum_{i=1}^{N} n_i(\mathbf{x}) = \int \mathrm{d}\mathbf{x} \sum_{i=1}^{N} |\psi_i(\mathbf{x})|^2 = N \tag{4.9}$$

where $n(\mathbf{x})$ is the electron density and N is the number of electrons. The Hartree equation for the single particle state ψ_i then becomes

$$\left[-\frac{1}{2}\nabla^2 + V_{ext}(\mathbf{x})\right]\psi_i(\mathbf{x}) + \sum_{j=1}^{N}\int \mathrm{d}\mathbf{x}'|\psi_j(\mathbf{x}')|^2\frac{1}{|\mathbf{r}-\mathbf{r}'|}\psi_i(\mathbf{x}) = \varepsilon_i\psi_i(\mathbf{x}) \tag{4.10}$$

The total energy in the Hartree approximation is obtained as

$$E_H = -\frac{1}{2}\sum_i\int \psi_i^*(\mathbf{x})\nabla^2\psi_i(\mathbf{x})\mathrm{d}\mathbf{x} + \int V_{ext}(\mathbf{x})n(\mathbf{x})\mathrm{d}\mathbf{x} + \frac{1}{2}\iint\frac{n(\mathbf{x}')n(\mathbf{x})}{|\mathbf{x}-\mathbf{x}'|}\mathrm{d}\mathbf{x}'\mathrm{d}\mathbf{x} \tag{4.11}$$

Here the first two terms are the kinetic energy and the energy from the external potential from by the nuclei. The third term is called the Hartree energy and contains the interaction from the average charge distribution caused by all the electrons. The Hartree term introduces an interaction between an electron and the electron density of the crystal, which in turn contains the electron itself. The electron thus interacts with itself. This causes the so-called *self-interaction error*.

This self-interaction error can to some degree be removed by taking the anti-symmetry of the wave function required by permutation symmetry for fermions into account. In the Hartree-Fock approximation this is done in the shape of a *Slater determinant*

$$\Psi(\mathbf{x}_1\mathbf{x}_2...\mathbf{x}_N) = \frac{1}{\sqrt{N}}\begin{vmatrix}\psi_1(\mathbf{x}_1) & \psi_2(\mathbf{x}_1) & \cdots & \psi_N(\mathbf{x}_1)\\ \psi_1(\mathbf{x}_2) & \psi_2(\mathbf{x}_2) & \cdots & \psi_N(\mathbf{x}_2)\\ \vdots & \vdots & \ddots & \vdots\\ \psi_1(\mathbf{x}_N) & \psi_2(\mathbf{x}_N) & \cdots & \psi_N(\mathbf{x}_N)\end{vmatrix} \tag{4.12}$$

where the $\psi_i(\mathbf{x}_j)$ is the atomic orbital of atom i at position and spin $\mathbf{x}_j = (\mathbf{r}_j, \sigma_j)$. The introduction of spin here is necessary since the total wave function consists of both a spatial and a spin part. In order for the total wavefunction to be anti-symmetric, as required for fermions, the contributions from both spin and spatial parts need to be considered. When the spin part is symmetric the spatial wave-function must be corrected for the self-interaction error. The inclusion of exchange as discussed below.

The Hartree-Fock equations are very similar to the Hartree equations above with the addition of a fourth term

$$E_x = -\frac{1}{2}\sum_{j=1}^{N}\delta_{\sigma_i,\sigma_j}\int \mathrm{d}\mathbf{r}\,\mathrm{d}\mathbf{r}'\,\psi_i^*(\mathbf{r})\psi_j^*(\mathbf{r}')\frac{1}{|\mathbf{r}-\mathbf{r}'|}\psi_i(\mathbf{r}')\psi_j(\mathbf{r}) \tag{4.13}$$

which is the non-local exchange term and is the result of the anti-symmetry of the wave function. The exchange term, which is non-zero only if the spin are parallel, removes the self-interaction in the Hartree-Fock approximation. However, the true wavefunction is not a single particle theory as there are electron-electron interaction-effects beyond the Hartree-term.

The difference between the Hartree and the Hartree-Fock approximations is the inclusion of *exchange* which removes the self-interaction caused by the Hartree term. Still, HF is an approximation and by definition the difference between the true many-particle ground state energy and the HF energy is called *correlation* [55].

4.3 The Hohenberg-Kohn Theorems

The great advantage of the Hartree and Hartree-Fock approximations (cf. Eq. (4.10)) is that the N-multiparticle Schrödinger equation has been reduced to N non-interacting single state equations. The great disadvantages are that correlation has been left out, that the exchange term in the Hartree-Fock approximation is non-local and that information about all single particle wave functions thus has to be evaluated and stored.

However, the problem can be reformulated with the electron density as the fundamental variable. This possibility of using the density as a fundamental variable had been explored [36, 37, 44], first by Thomas [123], Fermi [124] and Dirac [125] and also extensively in the special case of the homogeneous electron gas before Hohenberg and Kohn [33] proved in two famous theorems that

1. the external potential V_{ext} and thus the full Hamiltonian is uniquely determined by the ground state density $n_0(\mathbf{r})$
2. there exists a functional $E[n, V_{\text{ext}}]$ for any external potential V_{ext} such that the electron density $n(\mathbf{r})$ that minimises this functional will be the exact ground state density.

In short this means that there exists a functional of the electron density only, for any external potential, which solves the problem exactly, not only including exchange but also correlation. Furthermore, it uses the electron density as the fundamental variable.

The functional is defined by Hohenberg and Kohn as

$$F_{HK}[n] = \langle\Psi| \, T + V_{ee} \, |\Psi\rangle \tag{4.14}$$

where T is the kinetic energy and V_{ee} electron-electron interaction of the full interacting system. The corresponding energy functional

$$E_{HK}[n] = F[n] + \int \mathrm{d}\mathbf{r} \; V_{ext}(\mathbf{r}) n(\mathbf{r}) \tag{4.15}$$

satisfies the variational principle, i.e., it assumes it minimum at the value for the correct electron density $n(\mathbf{r})$ subject to the constraint

$$\int n(\mathbf{r})\mathrm{d}\mathbf{r} = N. \tag{4.16}$$

The Hohenberg-Kohn theorems give no explicit expression for this functional. While the last term in Equation (4.15) is easily computed, the Hohenberg-Kohn functional $F_{HK}[n]$, containing the kinetic energy and the electron-electron interaction of the full interacting system, remains unknown.

4.4 The Kohn-Sham Approach

Despite the theoretical beauty of the Hohenberg-Kohn theorems, they provide no recipe for how to make use of these theorems. An ansatz was proposed by Kohn and Sham [34] in which the full interacting many-body system is replaced by an auxiliary system of independent particles. The ansatz relies heavily on the first Hohenberg-Kohn theorem which can be regarded as the inverse relation to the Schrödinger equation. While the Schrödinger equation uniquely determines the wave functions and thus the electron density for a given external potential the first Hohenberg-Kohn theorem says that the inverse relation also holds.

The great benefit of the auxiliary system is twofold; firstly, it reduces the full problem of N interacting particles to N single particle systems, secondly, it separates out the kinetic energy term and the long-range Hartree term in such a way that the remaining exchange-correlation (xc) term can be approximated reasonably well by local or nearly local functionals of the density.

It should be stressed that the Kohn-Sham approach is *not* an approximation. In theory the Kohn-Sham approach would be exact if only the exchange-correlation functional were known. However, for practical calculations approximations to the unknown exchange-correlation functional must be introduced.

Kohn-Sham, in a manner analogous to the Hartree and Hartree-Fock approximation, proposed a separation of the two first terms into tree terms; a kinetic energy term of a *non*-interacting single particle $T_s[n(\mathbf{r})]$, a Hartree term $E_H[n(\mathbf{r})]$ and an exchange-correlation term E_{xc}. The Hohenberg-Kohn energy functional from Equation (4.15) then becomes

$$E_{KS}[n] = T_s[n(\mathbf{r})] + E_H[n(\mathbf{r})] + E_{xc}[n(\mathbf{r})] + \int \mathrm{d}\mathbf{r}\; V_{ext}(\mathbf{r})n(\mathbf{r}) \tag{4.17}$$

A variation of this expression with respect to the single particle wave functions $\psi_i(\mathbf{r})$ subject to the constraint in Equation (4.16) leads to

$$\left[-\frac{1}{2}\nabla^2 + \int \frac{n(\mathbf{r}')}{|\mathbf{r}-\mathbf{r}'|}\mathrm{d}\mathbf{r}' + V_{xc}(\mathbf{r}) + V_{ext}(\mathbf{r})\right]\psi_i(\mathbf{r}) = \varepsilon_i\psi_i(\mathbf{r}) \tag{4.18}$$

where

$$V_{xc}(\mathbf{r}) = \frac{\delta E_{xc}[n(\mathbf{r})]}{\delta n(\mathbf{r})} \tag{4.19}$$

The total energy of the system is

$$E_{KS} = \sum_i \varepsilon_i - E_H[n(\mathbf{r})] + E_{xc}[n(\mathbf{r})] - \int \mathrm{d}\mathbf{r} V_{xc}[n(\mathbf{r})]n(\mathbf{r}) \tag{4.20}$$

Although the Kohn-Sham equation similar to the Hartree equation (4.10) the main difference is that the Hamiltonian now depends on the density and not the one-particle wavefunctions.

4.5 Approximations to the Exchange-Correlation Functional

Up to this point the Density Functional Theory is exact, save for the Born-Oppenheimer approximation. However, in practise the xc-functional in Equation (4.19) must be approximated in some way. The Kohn-Sham approach of separating the Hohenberg-Kohn functional F_{HK} in a kinetic energy, a long range Hartree term and an exchange-correlation (xc) functional E_{xc} has the advantage that the xc-functional is rather small compared to the kinetic and the Hartree energies and may be approximated reasonably well as a local or nearly local functional of the particle density at the point $\mathbf{r}$ [38]. The accuracy of any DFT-calculation relies on the approximations of the xc-functional. Over the years an abundance of different xc-functional approximations have been proposed [35, 44, 45, 47–50, 60–64, 126], but still today the original functional proposed by Kohn-Sham, the local density approximation, is competitive in certain areas.

4.5.1 Local Density Approximation

The local density approximation (LDA) is perhaps the least sophisticated xc-functional. It is based upon the assumption that the electronic structure in solids to a good approximation can be described by the homogeneous electron gas [34]. In this limit the exchange and correlation can be seen as local, i.e., depends only on the electron density at each point. However, simplicity is also an advantage in that it's internal parameterisation can be computed in accurate or even exact model studies [55, 127–129]. It is given by an analytical expression, with the coefficients are determined, once and for all, using quantum Monte Carlo techniques [128]. The total xc-functional in the local density approximation can then be written as

$$E_{xc}[n(\mathbf{r})] = \int \mathrm{d}\mathbf{r}\, n(\mathbf{r})\, \varepsilon_{xc}\left(n(\mathbf{r})\right) \tag{4.21}$$

where $\varepsilon_{xc}(n(\mathbf{r}))$ is the energy density per electron at a point $\mathbf{r}$.

This approximation is remarkably accurate for many solids and was a contributing factor to the great success of the density functional theory. In particular the LDA predicts for example bond lengths in solids with close to homogeneous electron density to within a few percent. However, the LDA fails in molecules where the density varies rapidly.

4.5.2 Generalised Gradient Approximation

The general success of the LDA has inspired the development of various Generalised Gradient Approximations (GGA) with the explicit aim of accounting for the inhomogeneous electron density found in real material. The natural extension of the LDA is to include not only the (local) density at a point $\mathbf{r}$ but also (semi-local) gradients of the density $\varepsilon_{xc} = \varepsilon_{xc}(n(\mathbf{r}), \nabla n(\mathbf{r}))$. The presence of gradients in the functional expression have given this class of functionals its name. Several various forms have been proposed and although derived in different manners, the GGA:s give similar improvements over LDA. Unfortunately, there is no known systematic procedure for improving such “gradient corrections” to LDA, and in practise the development often relies heavily on physical intuition and trial and error [42].

A physically motivated approximation to construct a trusted approximation to the correct functional is to model the so-called xc-hole, which reflects the density-density correlation [51, 52]. From this form the form of the GGA:s can be derived. This procedure leads to some of the most famous and successful GGA versions, namely those proposed by Perdew and Wang (PW91) [129], Perdew, Burke and Ernzerhof [126] (PBE) and Perdew *et al.* [61](PBEsol).

4.5.3 The van der Waals density functional method

The effect of non-local correlation is often not addressed. Among non-local correlation effects are the van der Waals forces of London type between neutral atoms or molecules which are well established and go as $\sim 1/r^6$ in the asymptotic limit. Local or semi-local xc-functional approximations fail to achieve this limit. These effects of dispersion interaction are perhaps most important in sparse matter and biological systems where the wave-function overlap is minimal, but may still be relevant also in dense matter.

There are several ways to take van der Waals forces into account. The van der Waals density functional (vdW-DF) method [39, 130, 131] is very appealing as it produces the correct $1/r^6$ limit with no empirical fitting parameters. Also vdW-DF stays entirely within the DFT framework and like the LDA and GGA represents an explicit functional. It computes the beyond-LDA contributions to the correlation energy as a double integral similar to the Hartree energy

$$\begin{aligned} E_{\mathrm{xc}}^{\mathrm{vwWDF}} &= E_{\mathrm{x}}^{\mathrm{GGA}} + E_{\mathrm{c}}^{\mathrm{LDA}} + E_{\mathrm{c}}^{\mathrm{nl}}[n] \\ E_{c}^{\mathrm{nl}}[n] &= \frac{1}{2}\int n(\mathbf{r})\phi(\mathbf{r},\mathbf{r}')n(\mathbf{r}')\mathrm{d}\mathbf{r}\mathrm{d}\mathbf{r}'. \end{aligned} \tag{4.22}$$

Here, however, an explicit interaction kernel $\phi(\mathbf{r},\mathbf{r}')$ is derived from formal many-body theory of the electron gas theory focusing on the plasmon response [39, 132, 133]. The kernel can be tabulated and the computational cost of adding the non-local correlation term is practically negligible. In the the present thesis the observed cost is generally only about 5% higher than the cost for PBE functional.

The exchange part in the vdW-DF functionals is taken from a suitable GGA-functional. The initial vdW-DF1 functional used the exchange of revPBE [58], while the next version, vdW-DF2, used a revised version of the PW86 [59]. The version used in the this thesis is called vdW-DF-cx [62, 63] and is here abbreviated CX. It uses a combination of Langreth-Vosko exchange for small density variations and PW86 at larger variations in an exchange functional denoted LV-PW86r. The resulting non-empirical vdW-DF-cx functional is consistent in the sense that the same plasmon-response description [39] is used to set both exchange and correlation.

4.5.4 Hybrid functionals

DFT suffers from the well known self-interaction problem [55], as mentioned in Section 4.2. Self-interaction errors lead to a deviation from piecewise linearity of the xc-functional, a theoretically known criterion of the exact xc-functional, and delocalisation of the electrons.

It was mentioned already by Kohn and Sham that the inclusion of Fock exchange (FX), i.e., exchange computed using the Hartree-Fock method, should improve the results compared to LDA, since at least non-local exchange effects are included. As Kohn and Sham point out this may be regarded as a Hartree-Fock method corrected for correlation. However, correlation effects are still treated approximately.

The expected improvement over local and semi-local xc-functionals have inspired a number of functionals incorporating FX. However, although the inclusion of FX is supposed to remove the self-interaction, this is not the case. While the Hartree-Fock method is one-electron self-interaction-free it is not many-electron self-interaction-free and thus over-compensates the self-interaction [67]. Therefore, in general, FX is not incorporated in the way that was proposed by Kohn and Sham but by mixing a fraction of FX with the DFT exchange

$$E_{\mathrm{xc}} = E_{\mathrm{xc}}^{\mathrm{DFT}} + \alpha\left(E_{\mathrm{x}}^{\mathrm{HF}} - E_{\mathrm{x}}^{\mathrm{DFT}}\right) \tag{4.23}$$

One popular choice based on theoretical constraints is the mixing proposed by Perdew, Ernzerhof and Burke (PBE0) [45], which mixes the exchange and correlation from the GGA-PBE with 25% FX.

A computationally more efficient functional is the range separated hybrid functional proposed by Heyd, Scuseria and Ernzerhof (HSE) [47, 48] which splits the terms in the PBE0 into short- and long-range components, with FX only included within the region defined by the parameter ω and the long range exchange given by the semi-local PBE exchange.

$$E_{\mathrm{xc}}^{\mathrm{HSE}} = \alpha E_{\mathrm{x}}^{\mathrm{HF,SR}}(\omega) + (1-\alpha)\, E_{\mathrm{x}}^{\mathrm{PBE,SR}}(\omega) + E_{\mathrm{x}}^{\mathrm{PBE,LR}}(\omega) + E_{\mathrm{c}}^{\mathrm{PBE}} \tag{4.24}$$

The adjustable parameter ω, determines the extent of the short-range interactions, with $\omega = 0$ is equivalent to PBE0 and $\omega \to \infty$ to PBE. The ω must be small enough to agree with PBE0, but large enough to increase performance. There are two standard choices of ω. The first published article (HSE03) [47] stated a value of $\omega = 0.15\ a_0^{-1} \approx 0.3$ Å^{-1}. However, this was not the value actually used in the article and later an erratum was published [48] with stated a value of $\omega = 0.2$ Å^{-1}. The latter functional, which sometimes goes under the name HSE06, has been abbreviated HSE in this thesis.

The non-local correlation in vdW-DF-cx can be combined with non-local exchange into the hybrids vdW-DF-cx0 [49] and vdW-DF-cx0p [50] (in this thesis abbreviated CX0p). The hybrid extension follows the mixing scheme of Eq. (4.23) with $\alpha = 0.25$ for vdW-DF-cx0. After a theoretical derivation based on the adiabatic connection formula [51, 52, 134], the CX0p was proposed with $\alpha = 0.2$ [50]. This value, based on many-body perturbation-theory coincides with the value proposed by Becke [43] after a fitting procedure. The fact that the same value can be obtained using two fundamentally different approaches strengthens the argument for the α-value.

4.5.5 DFT+U – “poor man’s hybrid”

Calculations of exact exchange is computationally very demanding and sometimes the desired properties can be obtained with simpler methods. While hybrids are necessary for correcting the underestimated band-gap in a DFT calculation, the bandstructure within occupied bands can be improved by less computationally demanding schemes such as the DFT+U method [67–69, 135].

As opposed to the rather delocalised s and p states, the d and f states are rather localised and are not well described by LDA or GGA, which favour fractional occupancies. By adding a Hubbard-like on-site repulsion term to the semicore d (or f) states, fractional occupancies are penalised and the total energy is written [67, 135]

$$E_{\text{tot}}^{\text{DFT}+U}\left[\rho(\mathbf{r})\right] = E_{\text{tot}}^{\text{DFT}}\left[\rho(\mathbf{r})\right] + \sum_{t} \frac{U}{2} \left(\sum_{\alpha,\sigma} n_{\alpha,\alpha}^{t,\sigma} - \sum_{\alpha,\beta,\sigma} n_{\alpha,\beta}^{t,\sigma} n_{\beta,\alpha}^{t,\sigma} \right) \tag{4.25}$$

where $n_{\alpha,\alpha}^{t,\sigma}$ are the occupation matrices involving orbitals α and β for site t and spin channel σ.

The value of the U parameter is not transferable and has to be determined from case to case. Different possible approaches for determining the U parameter are possible, e.g. to produce the correct bandgap or the correct position of the d-band [136]. In the spirit of *first principles* it is desirable to determine the value of U without relying on experimental observations. In **Paper II** we choose to fit the U parameter to the piecewise linearity constraint of the xc-functional, i.e. that the energy increases linearly when filling the defect level, which is a theoretically known property of the true xc-functional [56].

4.6 Implementation in periodic solids

The presence of a differential operator in the Schrödinger equation Hamiltonian has caused a wide variety of approaches concerning the practical implementation. One of the most important aspects is how to represent the trial wavefunction solutions. A common approach is to expand the wavefunction in a complete set of basis functions, e.g. in a linear combination of atomic orbitals, which is rather natural in the representation of isolated molecules.

In solids with periodic boundary conditions the natural basis function is the plane wave due to its intrinsic periodicity. In a planewave basis an important implementation aspect is how to represent the core and the core electrons. A proper description of the core, where the wavefunctions oscillate rapidly, requires a very large number of plane waves. The all-electron potentials are not well suited for a planewave basis set, but by constructing an effective potential the core electrons, which do not participate in chemical bonding, can be treated together with the nuclei in a pseudopotential. The resulting system will exhibit a much smoother potential requiring significantly fewer planewave basis functions. With the PAW method the all-electron properties can still be obtained.

Since VASP, which is the code used throughout this thesis, is a planewave PAW code, these aspects will be given attention in the following sections.

4.6.1 Plane waves

Consider a lattice with the periodicity $\mathbf{R}$. The effective potential is then also periodic with the same periodicity $v_{\text{eff}}(\mathbf{r}) = v_{\text{eff}}(\mathbf{R} + \mathbf{r})$. In such a periodic lattice

Bloch's theorem states that a one-electron wavefunction can be written as

$$\psi_{\mathbf{k}}(\mathbf{r}) = u_{\mathbf{k}}(\mathbf{r})\mathrm{e}^{i\mathbf{k}\cdot\mathbf{r}} \tag{4.26}$$

where $u_{\mathbf{k}}(\mathbf{r})$ is a function with the periodicity of the lattice. Like any periodic function it can be expanded in a Fourier series

$$u_{\mathbf{k}}(\mathbf{r}) = \sum_m c_{\mathbf{k},m}\mathrm{e}^{i\mathbf{G}_m\cdot\mathbf{r}} \tag{4.27}$$

where $\mathbf{G}_m$ is a reciprocal lattice vector. The one-particle wave function can now be written

$$\psi_{\mathbf{k}}(\mathbf{r}) = \left(\sum_m c_{\mathbf{k},m}\mathrm{e}^{i\mathbf{G}_m\cdot\mathbf{r}}\right)\mathrm{e}^{i\mathbf{k}\cdot\mathbf{r}} = \sum_m c_{\mathbf{k},m}\mathrm{e}^{i(\mathbf{k}+\mathbf{G}_m)\cdot\mathbf{r}} \tag{4.28}$$

If the effective potential is local it can also be expand in a similar way

$$v_{\text{eff}}(\mathbf{r}) = \sum_m v_{\text{eff}}(\mathbf{G}_m)\mathrm{e}^{i\mathbf{G}_m\cdot\mathbf{r}} \tag{4.29}$$

Substituting these expressions back into the Kohn-Sham Equation (4.18),

$$\left(-\frac{1}{2}\nabla^2 + v_{\text{eff}}\left(\mathbf{r}\right)\right)\psi_{\mathbf{k}}(\mathbf{r}) = \varepsilon_{\mathbf{k}}\psi_{\mathbf{k}}(\mathbf{r}) \tag{4.30}$$

a reciprocal space equation for the coefficients $c_{\mathbf{k},m}$ can be obtained as

$$\frac{1}{2}\left|\mathbf{k}+\mathbf{G}_m\right|^2 c_{\mathbf{k},m} + \sum_{m'} v_{\text{eff}}\left(\mathbf{G}_m - \mathbf{G}_{m'}\right)c_{\mathbf{k},m} = \varepsilon_{\mathbf{k}}c_{\mathbf{k},m} \tag{4.31}$$

The original Kohn-Sham differential equation has now been rewritten as a matrix equation, one for each value of $\mathbf{k}$, where the matrix Hamiltonian is

$$\mathsf{H}_{m,m'}(\mathbf{k}) = \frac{1}{2}\left|\mathbf{k}+\mathbf{G}_m\right|^2\delta_{m,m'} + v_{\text{eff}}\left(\mathbf{G}_m - \mathbf{G}_{m'}\right) \tag{4.32}$$

The problems are that there are infinitely many $\mathbf{k}$-points to consider and that the Hamiltonian matrix in principle is of infinite dimension. In practise both these infinities can be handled by considering only a finite number of $\mathbf{k}$-points and reciprocal lattice vectors $\mathbf{G}$.

4.6.2 Finite sampling

It follows from Bloch's theorem (Equation (4.26)) that if $\psi_{\mathbf{k}}$ is a solution, then so is $\psi_{\mathbf{k+G}}$. The solutions can therefore be restricted to the primitive reciprocal unit cell, called the Brillouin zone. However, there is still an uncountably infinite number of **k**-points to consider. This is handled through discrete sampling of the Brillouin zone. In this thesis the common method of Monkhorst and Pack [137] has been used. The method selects N_i **k**-points along each reciprocal lattice vector **b** according to the scheme

$$u_{n_i} = \frac{2n_i - N_i - 1}{2N_i} \qquad n_i \in [1, N_i] \tag{4.33}$$

$$\mathbf{k}_{n_1,n_2,n_3} = u^{(1)}_{n_i}\mathbf{b}_1 + u^{(2)}_{n_i}\mathbf{b}_2 + u^{(3)}_{n_i}\mathbf{b}_3 \tag{4.34}$$

Due to symmetry in the crystal this can be reduced even further, to the irreducible Brillouin zone, and in practise, especially for crystals of high symmetry, only a few k-points will suffice to determine the electron density in the entire crystal.

The infinite sum over m' and thus the dimension of the Hamiltonian matrix can be truncated at a cut-off energy $\frac{1}{2}|\mathbf{k}+\mathbf{G}|^2 < E_{\text{cut}}$. This introduces a small error and E_{cut} has to be chosen judiciously taking both accuracy and computational cost into account. Usually, the energy cut-off is taken as a value beyond which accuracy increases only marginally when increasing the cut-off energy. The exact value of E_{cut} will depend on how the core electrons are treated. By using the pseudopotential method E_{cut} can be reduced greatly.

4.6.3 Pseudopotentials and PAW

A problem with plane wave basis sets is that rapidly varying functions, such as the wave functions close to heavy nuclei, require a very high cut-off energy in order to be well represented. One solution to this is the *pseudopotential* method in which the potential in the core region, i.e. the nucleus and the innermost electrons, are replaced by a different potential [138]. The argument for this is that the core electrons do not take part in and are to a large degree unaffected by chemical bonding. Among the requirements on pseudopotentials are that they should reproduce the true potential and electron density of the all-electron problem outside the core region as well as energy eigenvalues and be smooth enough that a low E_{cut} is possible.

Although the pseudopotentials are smoother than the original all-electron potentials they can be made even smoother by relaxing the norm-conserving condition. A norm-conserving pseudopotential generates pseudo wavefunctions which obey the usual orthogonality relation of wavefunctions. By relaxing the norm-conserving constraint it is possible to formulate ultrasoft pseudopotentials [139, 140], which reach the goal of accuracy while being much smoother and thus requiring decidedly smaller cut-off energy.

The ultrasoft pseudopotential method was refined and given a firmer theoretical footing by the works of Blöchl [141] and Kresse and Joubert [142] in the *Projector Augmented Wave* (PAW) method. The PAW method prescribes a linear mapping $\mathcal{T}$ which projects the pseudo wavefunctions inside the core regions onto the true all-electron wave functions. The PAW is therefore effectively an all-electron method giving access to the core electron states while still preserving all the benefits of a plane wave pseudopotential. In practise however, the frozen-core approximation is usually applied, in which the core states are not updated. This approximation usually leads to sufficient accuracy [143].

5

Vibrational motion

> “Because atomic behaviour is so unlike ordinary experience, it is very difficult to get used to, and it appears peculiar and mysterious to everyone - both to the novice and to the experienced physicist. ”
>
> – R. Feynman [144]

With the electronic structure problem formally solved it is time to turn to the vibrational motion of the ions. The free energy for the vibrational motion can be rather easily obtained if just the vibrational frequencies are known. The frequencies can be obtained by diagonalising the ionic Hamiltonian in Equation (4.6), which is obtained after applying the adiabatic approximation.

Although it is possible to write down a formal expression for the potential $V(\mathbf{R})$ in Equation (4.6), it is customary to expand the potential in a Taylor series. In the *harmonic approximation* the potential is expanded to second order. The second order term is a matrix, which can computed using first principle methods, and can be diagonalised to yield the eigenmodes and eigenfrequencies for the vibrational motion. These eigenmodes are collective lattice vibrations called *phonons* which oscillate in a harmonic potential for which the quantum mechanical solutions are known.

It is instructive to start the discussion about lattice vibrations with a one dimensional diatomic chain as many of the conclusions can be carried over to the three dimensional case while at the same time being more transparent [118, 145, 146].

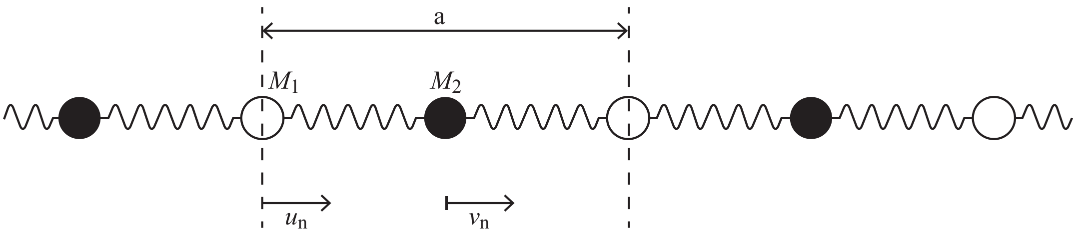

Figure 5.1: One-dimensional diatomic chain

5.1 One-dimensional diatomic chain

Assume a periodic chain of atoms of types A and B, with masses M_1 and M_2 separated a distance $a/2$, where a is the period of the chain, and connected with springs with spring constant c (see Figure 5.1). Denote the deviation from the equilibrium position by u_n and v_n for the atoms A and B respectively in unit cell n. By Hooke's law the atom A in unit cell n will then experience a restoring force equal to $F = c(v_n - u_n) + c(v_{n-1} - u_n) = (-2u_n + v_{n-1} + v_n)c$, and analogously for atom type B. By applying Newtons second law for both atom types we get two coupled differential equations

$$\begin{cases} M_1\ddot{u}_n = (-2u_n + v_{n-1} + v_n)c \\ M_2\ddot{v}_n = (-2v_n + u_n + u_{n+1})c \end{cases} \tag{5.1}$$

The right hand side of Equation (5.1) is the one dimensional equivalent of what will later be called the Force Constant (FC) matrix, times the displacement vector. A general form of solution to a second order differential equation is

$$u_n(t) = \frac{1}{\sqrt{M_1}}\tilde{u}_n \mathrm{e}^{-i\omega t}; \qquad v_n(t) = \frac{1}{\sqrt{M_2}}\tilde{v}_n \mathrm{e}^{-i\omega t} \tag{5.2}$$

which reduces the Equation (5.1) to

$$\begin{cases} -\omega^2\tilde{u}_n = -\frac{2c}{M_1}\tilde{u}_n + \frac{c}{\sqrt{M_1M_2}}\tilde{v}_{n-1} + \frac{c}{\sqrt{M_1M_2}}\tilde{v}_n \\ -\omega^2\tilde{v}_n = -\frac{2c}{M_2}\tilde{v}_n + \frac{c}{\sqrt{M_1M_2}}\tilde{u}_n + \frac{c}{\sqrt{M_1M_2}}\tilde{u}_{n+1} \end{cases} \tag{5.3}$$

By assuming plane wave like solutions we can introduce a phase factor dependence

$$\tilde{u}_n = U\mathrm{e}^{iqx_n}; \qquad \tilde{v}_n = V\mathrm{e}^{iqx_n} \tag{5.4}$$

where x_n is the position of the atoms in unit cell n. This can be written as $x_n = na$ and $x_n = (n+1/2)a$ for atoms A and B respectively. Equation (5.1) is now reduced to

$$\begin{cases} -\omega^2 U = -\frac{2c}{M_1}U + \frac{c}{\sqrt{M_1 M_2}}\mathrm{e}^{+iqa/2}V + \frac{c}{\sqrt{M_1 M_2}}\mathrm{e}^{-\mathrm{i}qa/2}V \\ -\omega^2 V = -\frac{2c}{M_2}V + \frac{c}{\sqrt{M_1 M_2}}\mathrm{e}^{+iqa/2}U + \frac{c}{\sqrt{M_1 M_2}}\mathrm{e}^{-\mathrm{i}qa/2}U \end{cases} \tag{5.5}$$

This can now be written as an eigenvalue problem in matrix notation

$$\omega^2_{q\pm}\mathbf{e}_{q\pm} = \mathsf{D}\left(q\right)\mathbf{e}_{q\pm} \tag{5.6}$$

Here $\mathbf{e}_{q\pm} = (U_\pm, V_\pm)^\mathsf{T}$ are the eigenvectors and

$$\mathsf{D}(q) = \begin{bmatrix} \frac{2c}{M_1} & -\frac{2c}{\sqrt{M_1 M_2}}\cos\left(\frac{qa}{2}\right) \\ -\frac{2c}{\sqrt{M_1 M_2}}\cos\left(\frac{qa}{2}\right) & \frac{2c}{M_2} \end{bmatrix} \tag{5.7}$$

is called the *Dynamical matrix.* This eigenvalue problem can now be solved to yield the eigenfrequencies and eigenmodes of the vibration. As with any 2 × 2 matrix there are two solutions

$$\omega^2_\pm = \frac{c}{M_1 M_2}\left[(M_1 + M_2) \pm \sqrt{(M_1 + M_2)^2 - 4M_1 M_2 \sin^2\left(\frac{qa}{2}\right)}\right] \tag{5.8}$$

In this case the solutions are non-degenerate and non-negative. The solutions are illustrated in Figure 5.2 as functions of q. It is already apparent, due to the periodicity of the cosine function, that the only region of interest is the first Brillouin zone, i.e. when $|q| \leqslant \frac{\pi}{a}$. The formal expression for the eigenvector $\mathbf{e}_\pm = (U_\pm, V_\pm)^\mathsf{T}$ is

$$\frac{U_\pm}{V_\pm} = \frac{c\left(1 + \mathrm{e}^{-\mathrm{i}qa}\right)}{2c - \omega^2_\pm M_1} \tag{5.9}$$

It should be stressed that no assumption has yet been made as to the direction of the displacements u_n and v_n. If the displacement is along the direction of propagation the mode is called *longitudinal.* The two perpendicular modes are called *transversal.* The different modes will in general have different coupling constants c in Equation (5.6).

5.1.1 High symmetry points

Two limiting cases are of particular interest, the limits when $qa \to 0$ and when $qa \to \pi$. The first case, the zone centre where $q = 0$ is called the Γ-point. This is true also in higher dimensions. The solutions near the Γ-point are

$$\omega^2_\Gamma = 2c\left(\frac{1}{M_1} + \frac{1}{M_2}\right) \quad \text{(optical mode)} \tag{5.10}$$

$$\omega^2_\Gamma = \frac{1}{2}\frac{c}{M_1 + M_2}q^2 a^2 \quad \text{(acoustic mode)} \tag{5.11}$$

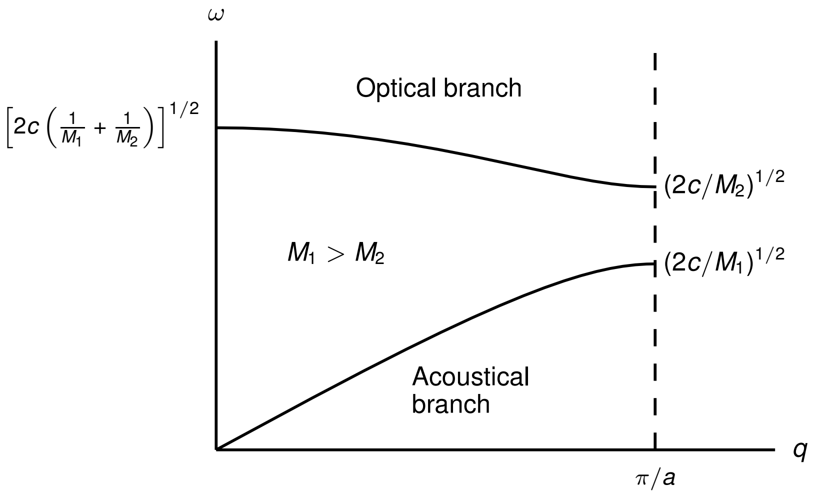

Figure 5.2: One-dimensional diatomic chain dispersion relation

We note immediately that there are two distinct types of solutions to Equation (5.6), one optic and one acoustic mode separated by a bandgap. The eigenvector (Equation (5.9)) for the optical mode is reduced to

$$\frac{U}{V} = -\frac{M_2}{M_1} \tag{5.12}$$

which shows that, at the Γ point, the atoms vibrate against one another with the centre of mass fixed. For the acoustic mode, the ratio is 1 and the atoms vibrate in phase and with the same amplitude. This infinite wavelength limit is equivalent to a pure translation of the lattice.

The zone boundary, where $q = \pi/a$ is another special or high symmetry point. The points have different designations in different symmetries. In 1D, the zone boundary point usually isn't given a name, but for convenience it will henceforth be denoted X in analogy with the point (1,0,0) in a 3D simple cubic lattice (see Figure 2.2). The eigenfrequencies at the zone boundary are

$$\omega_X^2 = \frac{2c}{M_2} \qquad \text{(optical mode)} \tag{5.13}$$

$$\omega_X^2 = \frac{2c}{M_1} \qquad \text{(acoustic mode)} \tag{5.14}$$

The eigenvectors become $\mathbf{e}_+ = (0,1)$ and $\mathbf{e}_- = (1,0)$ for the optical and acoustic modes respectively. This means that in the optic mode only the lighter atoms move and in the acoustic only the heavier.

Since the displacement of atom A in unit cell n is (cf. Eqs. (5.2) and (5.4))

$$u_n = \frac{1}{\sqrt{M_1}} U \mathrm{e}^{\mathrm{i}(qan-\omega t)} \tag{5.15}$$

we can express the displacement of the atom in the neighbouring unit cell as

$$\begin{aligned} u_{n+1} &= \frac{1}{\sqrt{M_1}} U \mathrm{e}^{\mathrm{i}(qa(n+1)-\omega t)} \\ &= \frac{1}{\sqrt{M_1}} U \mathrm{e}^{\mathrm{i}qa} \mathrm{e}^{\mathrm{i}(qan-\omega t)} \\ &= u_n \mathrm{e}^{\mathrm{i}qa} \end{aligned} \tag{5.16}$$

and analogously for the B atom. Thus, at the Γ-point where $q = 0$ all atoms of the same type move in the same direction, while at the Brillouin zone boundary where $q = \pi/a$ and $\mathrm{e}^{\mathrm{i}qa} = -1$ the atoms in neighbouring unitcells move in opposite directions.

5.1.2 Limiting cases I. Identical masses

The bandgap between the two branches at the zone boundary depends on the difference between the masses. In the limiting case when the masses $M_1 = M_2$ are equal the bandgap closes. This is because the atoms are now identical and the primitive unit cell is only half that of the unit cell in Figure 5.1. As a consequence the Brillouin zone is extended to $\frac{2\pi}{a}$. The point at $q = \pi/a$ is no longer a zone boundary point and the two different branches are in fact only one branch. The points on the optical branch should be unfolded to the region between $q = \pi/a$ and $q = 2\pi/a$ such that the Γ-point ends up on $q = 2\pi/a$.

5.1.3 Limiting cases II. Localised vibrations

In the limit when $M_2/M_1 \to 0$ the dispersion of the optical branch goes to zeros and the eigenfrequency becomes independent of q. The motion of one particular atom in one particular unit cell is thus independent of the motion of the atoms in neighbouring unit cells. The eigenvectors will, in this limit, become the same at the Γ point and at the zone boundary, $\mathbf{e}_+ = (0, 1)$. Thus the amplitude of the heavier atom will be negligible in comparison and the motion of the lighter is independent of q-value. In other words, the motion of one light atom is independent of the motion of any other atom in the lattice. Such a mode is called *localised.* The unit cell can be treated as if it were an isolated molecule with no periodicity. In this case only the Γ point has to be considered.

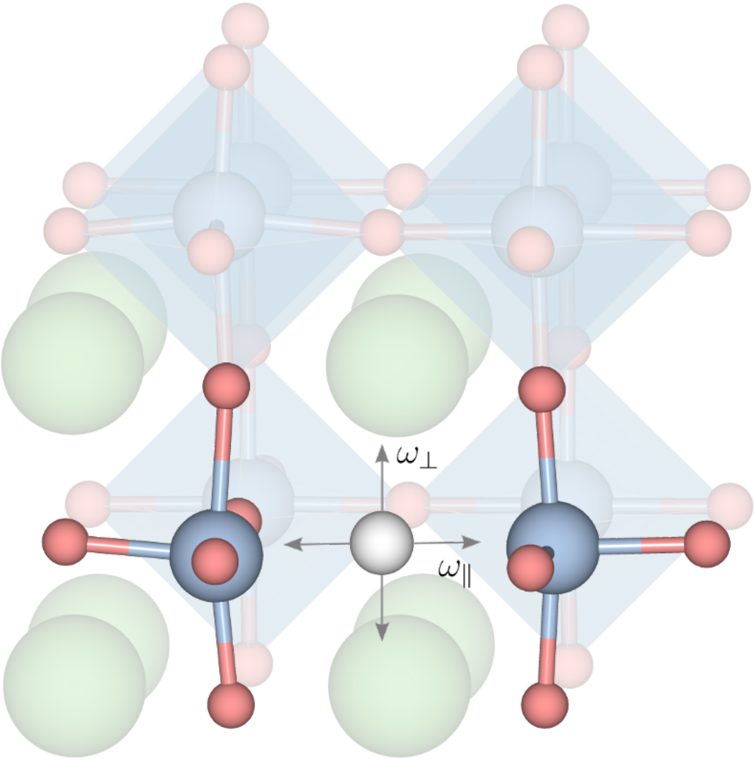

Figure 5.3: Illustration of hydride vibrational modes in the oxyhydride $BaTiO_3$.

5.1.4 Application in oxyhydrides

The one-dimensional diatomic chain is used qualitatively in the study of the oxyhydride $BaTiO_3$ in **Paper II** and **Paper III**. The hydrogen vibrational modes are very localised and it is possible to treat all ions as immobile, except for the oxygen and hydrogen ions along the O-Ti-H-Ti chain, with the hydrogen ion the lighter with mass M_2 and the oxygen ion the heavier with mass M_1. The oxyhydride barium titanate is illustrated in Figure 5.3. In the higher frequency mode the displacements are along the chain while the lower frequency mode is two fold degenerate and perpendicular to the direction of the chain. These three modes are seen as optical modes with very little dispersion in Figure 5.4c. The effective mass for oxygen in atomic mass units is 83 for the longitudinal mode and 426 for the transverse modes, in both cases much than larger 16, the atomic mass for oxygen, which shows that the approximation of a one-dimensional diatomic chain in the limit of infinite mass for one of the atoms holds.

5.2 Lattice modes

In reality the atomic motion in a solid occur in three dimensions and the above model, albeit instructive and intuitive, needs to be generalised [118–120, 145, 147]. The potential energy in a periodic solid, $V(\mathbf{R})$, is a function of the positions $\mathbf{R}$ of all atoms in the crystal. Under the assumptions that the deviations from equilibrium are small the potential energy can be written as an expansion with respect to the displacements $dR_{ni\alpha}$. Furthermore, a local minimum is characterised by the first derivative being zero. By keeping only second order terms in what is called *the harmonic approximation* the potential can be written

$$V(\{\mathbf{R}\}) = V(\{\mathbf{R_0}\}) + \frac{1}{2}\sum_{ni\alpha,mj\beta}\frac{\partial^2 V(\{\mathbf{R_0}\})}{\partial R_{ni\alpha}\partial R_{mj\beta}}\mathrm{d}R_{ni\alpha}\mathrm{d}R_{mj\beta} \tag{5.17}$$

where $V(\{\mathbf{R_0}\}) = E_0$ is the equilibrium energy and is a function of the equilibrium positions $\{\mathbf{R_0}\}$ of all ions. E_0 can e.g. be obtained from DFT calculations. This is just an additive constant and we are free to choose the energy scale in the following such that $E_0 = 0$. The indices i, j indicate sum over atoms in the unit cell, n, m indicate sum over unit cells and α, β the sum over cartesian directions.

With the notation for the displacements $u = \mathrm{d}R$ the ionic Hamiltonian from Equation (4.6) can be written (in the adiabatic approximation)

$$H_n = \sum_{ni\alpha}\frac{p_{ni\alpha}^2}{2M_i} + \frac{1}{2}\sum_{ni\alpha,mj\beta}F_{ni\alpha,mj\beta}u_{ni\alpha}u_{mj\beta} \tag{5.18}$$

The matrix $F_{ni\alpha,mj\beta}$ is called the *Force Constant (FC) Matrix.* Due to the commutativity of the derivatives it is immediately obvious that the FC-matrix is symmetric. The equations of motion become

$$M_i\ddot{u}_{ni\alpha} = -\sum_{mj\beta}F_{ni\alpha.mj\beta}u_{mj\beta} \tag{5.19}$$

By assuming wavelike solutions, a general form of solution is of the form

$$u_{ni\alpha}(t) = \frac{1}{\sqrt{M_i}}\tilde{u}_{ni\alpha}\mathrm{e}^{-\mathrm{i}\omega t} \tag{5.20}$$

Inserting this expression, Equation (5.19) can be written

$$\omega^2\tilde{u}_{ni\alpha} = \sum_{mj\beta}\frac{1}{\sqrt{M_iM_j}}F_{ni\alpha.mj\beta}\tilde{u}_{mj\beta} \tag{5.21}$$

Let us now introduce a new matrix, which is a real space representation of the dynamical matrix[1]

$$\tilde{D}_{ni\alpha,mj\beta} = \frac{1}{\sqrt{M_i M_j}} F_{ni\alpha.mj\beta} \tag{5.22}$$

and has the dimension $3 \times n \times N$, where n is the number of atoms in the unit cell, N is the number of unit cells in the system and 3 is the dimension of space.

5.2.1 q-space

In an (infinite) periodic solid it is convenient to introduce the q-space[2] representation, the *Dynamical Matrix*. First, since the energy cannot depend on the absolute positions of cells n and m, only on their relative position $\mathbf{R} = \mathbf{R}_n - \mathbf{R}_m$ we have

$$\tilde{D}_{ni\alpha,mj\beta} = \frac{1}{\sqrt{M_i M_j}} F_{ni\alpha,mj\beta} = \tilde{D}_{i\alpha,j\beta}(\mathbf{R}_n - \mathbf{R}_m) \tag{5.23}$$

By virtue of Bloch's theorem we can set the $\mathbf{R}$-dependence as a phase and write

$$\tilde{u}_{ni\alpha} = e_{i\alpha} \mathrm{e}^{\mathbf{iq} \cdot \mathbf{R}_n} \tag{5.24}$$

which gives the eigenvalue problem as

$$\omega^2 e_{i\alpha} = \sum_{mj\beta} \tilde{D}_{i\alpha,j\beta}(\mathbf{R}_n - \mathbf{R}_m) \mathrm{e}^{-\mathbf{iq} \cdot (\mathbf{R}_n - \mathbf{R}_m)} e_{j\beta} \tag{5.25}$$

By Fourier transform of the dynamical matrix

$$D_{i\alpha,j\beta}(\mathbf{q}) = \sum_{\mathbf{R}} \tilde{D}_{i\alpha,j\beta}(\mathbf{R}) \mathrm{e}^{-\mathbf{iq} \cdot \mathbf{R}} = \sum_n \mathrm{e}^{-\mathbf{iq} \cdot \mathbf{R}_n} \frac{1}{\sqrt{M_i M_j}} \frac{\partial^2 V}{\partial u_{ni\alpha} \partial u_{0j\beta}} \tag{5.26}$$

we now get the eigenvalue problem

$$\omega^2 e_{i\alpha} = \sum_{j,\beta} D_{i\alpha,j\beta}(\mathbf{q}) e_{j\beta} \tag{5.27}$$

or in matrix notation

$$\omega^2_{s\mathbf{q}} \mathbf{e}_{s\mathbf{q}} = \mathsf{D}(\mathbf{q}) \mathbf{e}_{s\mathbf{q}} \tag{5.28}$$

where the index s denotes the $3 \times n$ solutions at each $\mathbf{q}$-point. The original problem of diagonalising a $3 \times n \times N$ matrix (where the number of unit cells N in principle is infinite) has now been reduced to diagonalising one marix of size $3 \times n$ for each value of $\mathbf{q}$. As with the electronic structure problem (cf. Section 4.6.2), this can be done at a finite number of $\mathbf{q}$-points.

---

[1] The literature is not completely consistent in the notation. Sometimes the FC-matrix is defined weighted with the masses, what is here called the real space dynamical matrix (cf. Equation 5.22), sometimes the opposite. Another name for the FC-matrix is the *Hessian matrix*

[2] The reciprocal space is customarily called k-space, but we will here use the notation q-space for the phonon motion in order not to confuse it with the electronic structure k-space.

5.2.2 Atomic displacements

Once the eigenvectors are found the displacement of ion i at lattice vector $\mathbf{R}_n$ in the mode s with frequency $\omega_{s\mathbf{q}}$ will be given by

$$u_{nis}(\mathbf{q},t) = \frac{1}{\sqrt{M_i}}\mathbf{e}_{i\mathbf{q}s}\mathrm{e}^{\mathrm{i}(\mathbf{q}\cdot\mathbf{R}_n-\omega_{s\mathbf{q}}t)} \tag{5.29}$$

where $\mathbf{e}_{i\mathbf{q}s}$ is the set of d components of the eigenvector solutions to Equation (5.28) that denote the displacement of ion i at frequency $\omega_{s\mathbf{q}}$ in d dimensions. It is customary to chose the eigenvectors to be orthonormal

$$\sum_i \left[\mathbf{e}_{i\mathbf{q}s}\right]^* \mathbf{e}_{i\mathbf{q}s} = \delta_{ss'} \tag{5.30}$$

The most general displacement of ions is the superposition of all linearly independent elementary solutions and can be written as

$$u_{ni}(t) = \frac{1}{\sqrt{M_i}}\sum_{s,\mathbf{q}} c_{s\mathbf{q}}\mathbf{e}_{i\mathbf{q}s}\mathrm{e}^{\mathrm{i}(\mathbf{q}\cdot\mathbf{R}_n-\omega_{s\mathbf{q}}t)} \tag{5.31}$$

where the coefficient $c_{s\mathbf{q}}$ corresponds to the amplitude of the oscillation.

5.2.3 Normal coordinates

The time dependence can be absorbed in a time dependent *normal coordinate* or *generalised coordinate* $Q_{s\mathbf{q}}(t) = c_{s\mathbf{q}}\sqrt{N}\mathrm{e}^{-\mathrm{i}\omega_{s\mathbf{q}}t}$, where N is the number of unit cells in the crystal. It is already clear that, independently for each mode s, $Q_{s\mathbf{q}}(t)$ satisfies the differential equation of a harmonic oscillator

$$\ddot{Q}_{s\mathbf{q}} + \omega_{s\mathbf{q}}^2 Q_{s\mathbf{q}} = 0 \tag{5.32}$$

The displacement can then be written as

$$u_{ni}(t) = \frac{1}{\sqrt{NM_i}}\sum_{s,\mathbf{q}} Q_{s\mathbf{q}}(t)\mathbf{e}_{i\mathbf{q}s}\mathrm{e}^{\mathrm{i}\mathbf{q}\cdot\mathbf{R}_n} \tag{5.33}$$

From the relation $\dot{u}_{ni}(t) = M_i p_{ni}(t)$, which follow immediately from the equations of motion, we can write

$$p_{ni}(t) = \sqrt{\frac{M_i}{N}}\sum_{s,\mathbf{q}} \dot{Q}_{s\mathbf{q}}(t)\mathbf{e}_{i\mathbf{q}s}\mathrm{e}^{\mathrm{i}\mathbf{q}\cdot\mathbf{R}_n} \tag{5.34}$$

Since this describes displacements of ions in a real crystal, both u_{ni} and p_{ni} have to be real. In addition, due to symmetry $\mathbf{q} \to -\mathbf{q}$

$$[Q_{s\mathbf{q}}(t)\mathbf{e}_{i\mathbf{q}s}]^* = Q_{s(-\mathbf{q})}(t)\mathbf{e}_{i(-\mathbf{q})s} \tag{5.35}$$

and since this must be true at all times, both $Q_{s\mathbf{q}}(t)$ and $\mathbf{e}_{i\mathbf{q}s}$ must obey this relation separately.

Equation (5.33) can be inverted

$$\frac{1}{\sqrt{N}}\sum_n u_{mi}(t)\mathrm{e}^{-\mathrm{i}\mathbf{q}\cdot\mathbf{R}_m} = \frac{1}{\sqrt{M_i}}\sum_{s,\mathbf{q}} Q_{s\mathbf{q}}(t)\mathbf{e}_{i\mathbf{q}s}\underbrace{\frac{1}{N}\sum_m \mathrm{e}^{\mathrm{i}\mathbf{q}\cdot(\mathbf{R}_n-\mathbf{R}_m)}}_{=\delta((\mathbf{R}_n-\mathbf{R}_m)-\mathbf{G})} \tag{5.36}$$

$$\sqrt{\frac{M_i}{N}}\sum_{ni} u_{ni}(t)\mathrm{e}^{-\mathrm{i}\mathbf{q}\cdot\mathbf{R}_n}\left(\mathbf{e}_{i\mathbf{q}'s}\right)^* = \sum_s Q_{s\mathbf{q}}(t)\underbrace{\sum_i \mathbf{e}_{i\mathbf{q}s}\mathbf{e}^*_{i\mathbf{q}'s}}_{=\delta_{ss'}} \tag{5.37}$$

$$Q_{s\mathbf{q}}(t) = \sum_{ni}\sqrt{\frac{M_i}{N}}\left(\mathbf{e}_{i\mathbf{q}s}\right)^*\mathrm{e}^{-\mathrm{i}\mathbf{q}\cdot\mathbf{R}_n}u_{ni}(t) \tag{5.38}$$

The kinetic term in the Hamiltonian can now be written as

$$\begin{aligned}
T &= \sum_{ni\alpha}\frac{p_{ni\alpha}}{2M_i} \\
&= \frac{1}{2}\sum_{ni\alpha} M_i(\dot{u})^2 \\
&= \frac{1}{2}\sum_{ni\alpha}\left(\sum_{s\mathbf{q}}\dot{Q}_{s\mathbf{q}}e^{i,\alpha}_{s\mathbf{q}}\mathrm{e}^{i\mathbf{q}\cdot\mathbf{R}_n}\right)\left(\sum_{s'\mathbf{q}'}\dot{Q}_{s'\mathbf{q}'}e^{i,\alpha}_{s'\mathbf{q}'}\mathrm{e}^{i\mathbf{q}'\cdot\mathbf{R}_n}\right) \\
&= \frac{1}{2}\sum_{ni\alpha}\sum_{ss'}\sum_{\mathbf{q}\mathbf{q}'}\dot{Q}_{s\mathbf{q}}\dot{Q}_{s'\mathbf{q}'}e^{i,\alpha}_{s\mathbf{q}}e^{i,\alpha}_{s'\mathbf{q}'}\underbrace{\sum_n \mathrm{e}^{i\mathbf{q}+\mathbf{q}'\cdot\mathbf{R}_n}}_{\implies \mathbf{q}'=-\mathbf{q}} \\
&= \frac{1}{2}\sum_{ss'}\sum_{\mathbf{q}}\dot{Q}_{s\mathbf{q}}\dot{Q}_{s'-\mathbf{q}}\sum_{i\alpha}e^{i,\alpha}_{s\mathbf{q}}e^{i,\alpha}_{s'-\mathbf{q}} \\
&= \frac{1}{2}\sum_{ss'}\sum_{\mathbf{q}}\dot{Q}_{s\mathbf{q}}\dot{Q}^*_{s'\mathbf{q}}\underbrace{\sum_{i\alpha}e^{i,\alpha}_{s\mathbf{q}}\left(e^{i,\alpha}_{s'\mathbf{q}}\right)^*}_{\delta_{ss'}} \\
&= \frac{1}{2}\sum_{s\mathbf{q}}\dot{Q}_{s\mathbf{q}}\dot{Q}^*_{s\mathbf{q}}
\end{aligned} \tag{5.39}$$

After a similar calculation, making use of the reciprocal space representation of the dynamical matrix, the potential term becomes

$$V = \frac{1}{2} \sum_{ni\alpha,mj\beta} F_{ni\alpha,mj\beta} u_{ni\alpha} u_{mj\beta} = \frac{1}{2} \sum_{s\mathbf{q}} \omega_{s\mathbf{q}}^2 Q_{s\mathbf{q}} Q_{s\mathbf{q}}^* \tag{5.40}$$

The Hamiltonian can now be written as $H = T + V$ from which follows that the *conjugate momentum* can be written as

$$P_{s\mathbf{q}} = \frac{\partial \mathcal{L}}{\partial(\dot{Q}_{s\mathbf{q}}^*)} = \dot{Q}_{s\mathbf{q}} \tag{5.41}$$

The harmonic approximation Hamiltonian in (5.18) becomes

$$H = \frac{1}{2} \sum_{s\mathbf{q}} \left(P_{s\mathbf{q}} P_{s\mathbf{q}}^* + {\omega_{s\mathbf{q}}}^2 Q_{s\mathbf{q}} Q_{s\mathbf{q}}^* \right) \tag{5.42}$$

This formally diagonalises the Hamiltonian and is identical to a set of independent harmonic oscillators with frequencies $\omega_{s\mathbf{q}}$, where $Q_{s\mathbf{q}}$ and $P_{s\mathbf{q}}$ are the generalised coordinates and momenta of collective motions.

5.2.4 Quantization

In the above derivation there is nothing preventing the amplitudes take on any real value, similar to a classical particle. The theory can be quantized by imposing canonical commutation relations. We will choose to define

$$\left[Q_{s\mathbf{q}}, P_{s'\mathbf{q}'}^\dagger \right] = \delta_{ss'} \delta_{\mathbf{q}\mathbf{q}'} \tag{5.43}$$

All other commutators are zero.

Introducing creation and annihilation operators $a_{j\mathbf{q}}$ and $a_{j\mathbf{q}}^\dagger$ in the usual fashion

$$\begin{aligned} Q_{s\mathbf{q}} &= \sqrt{\frac{\hbar}{2\omega_{s\mathbf{q}}}} \left(a_{j\mathbf{q}} + a_{j(-\mathbf{q})}^\dagger \right) \\ P_{s\mathbf{q}} &= -\mathrm{i} \sqrt{\frac{\hbar \omega_{s\mathbf{q}}}{2}} \left(a_{j\mathbf{q}} - a_{j(-\mathbf{q})}^\dagger \right) \end{aligned} \tag{5.44}$$

leads to the commutation relations

$$\left[a_{j\mathbf{q}}, a_{j'\mathbf{q}'}^\dagger \right] = \delta_{jj'} \delta_{\mathbf{q}\mathbf{q}'} \quad [a_{j\mathbf{q}}, a_{j'\mathbf{q}'}] = [a_{j\mathbf{q}}^\dagger, a_{j'\mathbf{q}'}^\dagger] = 0 \tag{5.45}$$

Inserting this in Equation (5.42) leads to the Hamiltonian

$$H = \sum_{s\mathbf{q}} \hbar \omega_{s\mathbf{q}} \left(a_{s\mathbf{q}}^\dagger a_{s\mathbf{q}} + \tfrac{1}{2} \right) = E_0 + \sum_{s\mathbf{q}} \hbar \omega_{s\mathbf{q}} \hat{n}_{s\mathbf{q}} \tag{5.46}$$

Here $\hat{n}_{s\mathbf{q}}$ is the number operator and $E_0 = \sum_{s\mathbf{q}} \hbar\omega_{s\mathbf{q}}/2$ is a constant called the zero point energy, which is given considerable attention in **Paper IV** and **Paper V**.

Once again, we see that, in the harmonic approximation, crystal vibrations are made up of a set of independent oscillators.

5.2.5 Mean square displacement

Before quantization the displacement of an atom in the crystal could take on any real value (cf. Equation (5.33)). After quantization the atomic displacement is given by

$$u_{ni}(t) = \sum_{s\mathbf{q}} \sqrt{\frac{\hbar}{2Nm_i\omega_{s\mathbf{q}}}} \left(a_{j\mathbf{q}} + a^{\dagger}_{j(-\mathbf{q})} \right) \mathbf{e}_{i\mathbf{q}s} \mathrm{e}^{\mathrm{i}\mathbf{q}\cdot\mathbf{R}_n} \tag{5.47}$$

This leads to the mean square displacement (MSD) projected onto the individual atoms i and cartesian directions α

$$\langle u^2_{i,\alpha} \rangle = \sum_{s\mathbf{q}} \frac{\hbar}{2Nm_i\omega_{s\mathbf{q}}} \left(1 + 2n_{s\mathbf{q}}\right) |e^{i,\alpha}_{\mathbf{q}s}|^2 \tag{5.48}$$

where m_i is the mass of atom i, s is again the band index and $n_{s\mathbf{q}}$ is the number operator. At finite temperature (see Sec. 5.2.6) it will be replaced by its thermal average, the Bose-Einstein population factor, which takes temperature dependence for the mean square displacement into account.

In analogy with the mean square displacement, the mean square momentum can be computed as

$$\langle p^2_{i,\alpha} \rangle = \sum_{\mathbf{q}s} \frac{m_i\hbar\omega_{s\mathbf{q}}}{2N} \left(1 + 2n_{\mathbf{q}}\right) |e^{i,\alpha}_{\mathbf{q}s}|^2 \tag{5.49}$$

In order to compare with the experiments in **Paper IV** the total mean square momentum for atom i is computed as the average

$$\langle p^2_i \rangle = \frac{1}{3} \sum_{\alpha} \langle p^2_{i,\alpha} \rangle \tag{5.50}$$

5.2.6 Vibrational free energy

We are often interested of quantities at finite temperatures. Using the expression for the energy from Equation (5.46) the partition function becomes

$$Z_{\mathrm{vib}} = \sum_{n_{s\mathbf{q}}} e^{-\beta E_n} = \prod_{s\mathbf{q}} e^{-\beta\hbar\omega_{s\mathbf{q}}/2} \sum_{n_{s\mathbf{q}}} e^{-\beta\hbar\omega_{s\mathbf{q}} n_{s\mathbf{q}}} = \prod_{s\mathbf{q}} \frac{e^{-\beta\hbar\omega_{s\mathbf{q}}/2}}{1 - e^{-\beta\hbar\omega_{s\mathbf{q}}}} \tag{5.51}$$

Here the last equality follows because the sum over n runs over all integer numbers including zero, which makes the sum a geometrical series.

We can now write the vibrational free energy $F_{\text{vib}} = -k_B T \ln\left(Z_{\text{vib}}\right)$ for a periodic solid as

$$F_{\text{vib}} = \sum_{s\mathbf{q}} \left(\frac{\hbar\omega_{s\mathbf{q}}}{2} + k_B T \ln\left(1 - e^{-\beta\hbar\omega_{s\mathbf{q}}}\right) \right) = E_0 + k_B T \sum_{s\mathbf{q}} \ln\left(1 - e^{-\beta\hbar\omega_{s\mathbf{q}}}\right) \tag{5.52}$$

where E_0 is the zero point energy.

The internal energy and the entropy can be obtained as derivatives of the partition function

$$U_{\text{vib}} = -\frac{\partial}{\partial\beta}\Big(\ln Z_{\text{vib}}\Big) = \sum_{s\mathbf{q}} \left(\frac{\hbar\omega_{s\mathbf{q}}}{2} + \frac{\hbar\omega_{s\mathbf{q}}}{e^{\beta\hbar\omega_{s\mathbf{q}}} - 1} \right) = \sum_{s\mathbf{q}} \frac{\hbar\omega_{s\mathbf{q}}}{2}\left(2n_{s\mathbf{q}} + 1\right) \tag{5.53}$$

$$S_{\text{vib}} = \frac{\partial}{\partial T}\Big(k_B T \ln Z_{\text{vib}}\Big) = k_B \sum_{s\mathbf{q}} \left(\frac{\beta\hbar\omega_{s\mathbf{q}}}{e^{\beta\hbar\omega_{s\mathbf{q}}} - 1} - \ln\left(1 - e^{-\beta\hbar\omega_{s\mathbf{q}}}\right) \right) \tag{5.54}$$

The vibrational motion thus contributes both to the internal energy and the entropy.

Within the harmonic approximation, the expression for the internal energy U can also be obtained directly. By taking the thermal average $\langle n_{s\mathbf{q}} \rangle = n_{s\mathbf{q}}(T)$ the number operator is transformed into the Bose-Einstein population factor

$$n_{s\mathbf{q}}(T) = \frac{1}{\exp\left(\frac{\hbar\omega_{s\mathbf{q}}}{k_{\text{B}}T}\right) - 1}. \tag{5.55}$$

This leads to the thermodynamic energy U_{vib}. The internal energy can be written in yet another shape through another often used identity

$$2n_{s\mathbf{q}} + 1 = \coth\left(\tfrac{1}{2}\beta\hbar\omega_{s\mathbf{q}}\right). \tag{5.56}$$

5.2.7 Bandstructure

The vibrational properties of a periodic system are given by its eigenfrequencies, found by diagonalising the Dynamical matrix at each respective q-point in the first Brillouin zone. However, illustrating this in a figure is not as straight forward as in the one-dimensional case in Figure 5.2 since $\mathbf{q}$ is a three-dimensional vector. It it therefore convenient to plot the vibrational frequencies only at selected points of high symmetry in the Brillouin zone and along the path that connects them in a *bandspectrum*. As an example of a bandspectrum Figure 5.4 shows the bandspectra of pristine cubic BaTiO_3 and SrTiO_3 along the high symmetry paths illustrated in Figure 2.2 as well as the bandspectrum of the oxyhydride $\text{BaTiO}_{3-x}\text{H}_x$ in a 40 atom simulation cell.

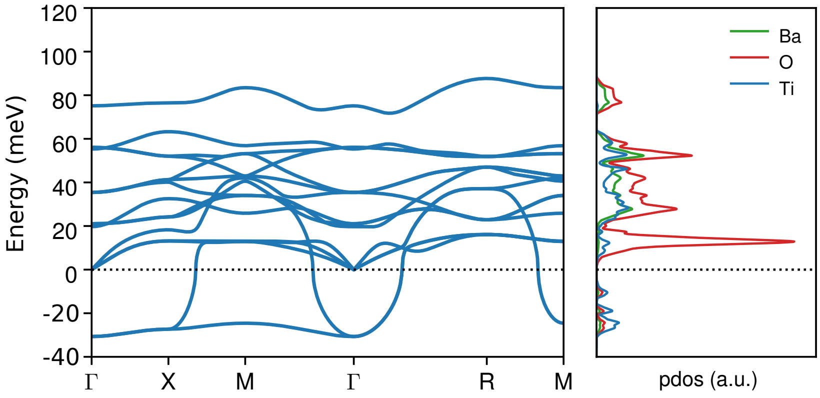

(a) $BaTiO_3$

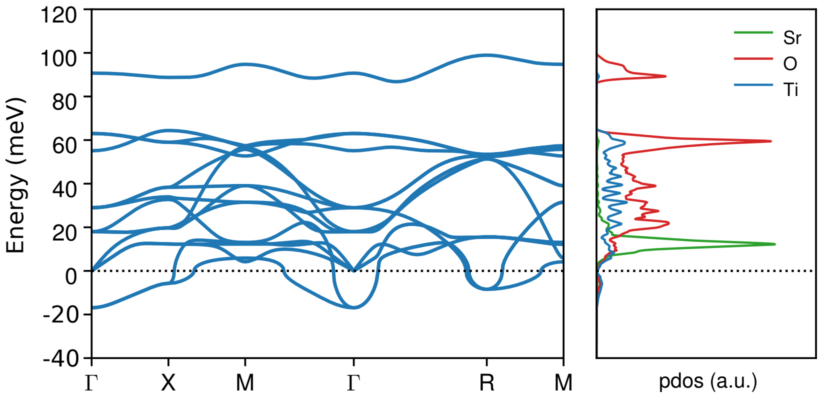

(b) $SrTiO_3$

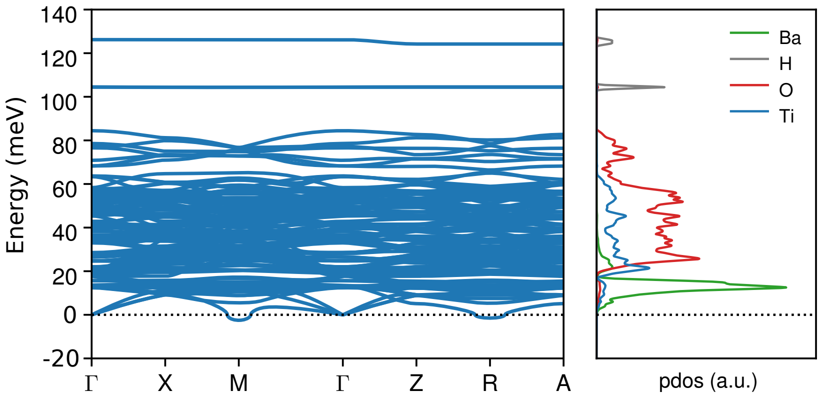

(c) $BaTiO_{3-x}H_x$ bandstate

Figure 5.4: Illustration the bandspectrum (left) and PDOS (right) of (a) pristine cubic $BaTiO_3$ (top), (b) pristine cubic $SrTiO_3$ (middle) and (c) oxyhydride $BaTiO_{3-x}H_x$ (bottom).

5.2.8 Density of State

Often, it is not necessary to illustrate the full vibrational spectrum. Rather, it is sufficient or even desirable to present only a the *density of state* (DOS).

The density of state is a convenient measure of the number of phonons in the interval $[\omega, \omega + \mathrm{d}\omega]$ independent of the $\mathbf{q}$-vector. Formally this can be written as

$$g(\omega) = \sum_{s\mathbf{q}} \delta\left(\omega - \omega_{s\mathbf{q}}\right) \tag{5.57}$$

By integrating the DOS

$$n(\omega) = \int_0^{\omega} g(\omega')\mathrm{d}\omega' \tag{5.58}$$

the number of modes with frequencies below or equal to ω is obtained. By integrating over all frequencies the total number of $3n$ modes is obtained, where n is the number of atoms in the unit cell.

The DOS is useful in the thermodynamic limit of an infinite crystal where the sum over $\mathbf{q}$ in e.g. Equation (5.52) approaches an integral. Using the identity

$$\sum_{s\mathbf{q}} f(\mathbf{q}) = \sum_{s} \frac{\Omega_c}{(2\pi)^3} \int_{BZ} \mathrm{d}\mathbf{q} f(\mathbf{q}) = \int g(\omega) f(\omega) \mathrm{d}\omega \tag{5.59}$$

where Ω_c is the volume of the unit cell, any function of s and $\mathbf{q}$, such as the free energy in Section 5.2.6 can be written in terms of an integral with the density of state as a weight function.

In computer simulations it is possible to separate the contribution from different elements. The *partial density of states* (PDOS) is the density of state caused by the motion of atom i

$$g_i(\omega) = \sum_{s\mathbf{q}} \left|\mathbf{e}_{i\mathbf{q}s}\right|^2 \delta\left(\omega - \omega_{s\mathbf{q}}\right) \tag{5.60}$$

If the atom i does not participate in the mode at frequency $\omega_{s\mathbf{q}}$, the corresponding eigenvector $\mathbf{e}_{i\mathbf{q}s}$ will be the zero vector and the partial density of state at this frequency is zero. As an example Figure 5.4 shows the PDOS of pristine cubic $BaTiO_3$ and $SrTiO_3$ as well as the PDOS of the oxyhydride $BaTiO_{3-x}H_x$ in a 40 atom simulation cell. The correspondence between the bandspectrum and density of state is clearly seen.

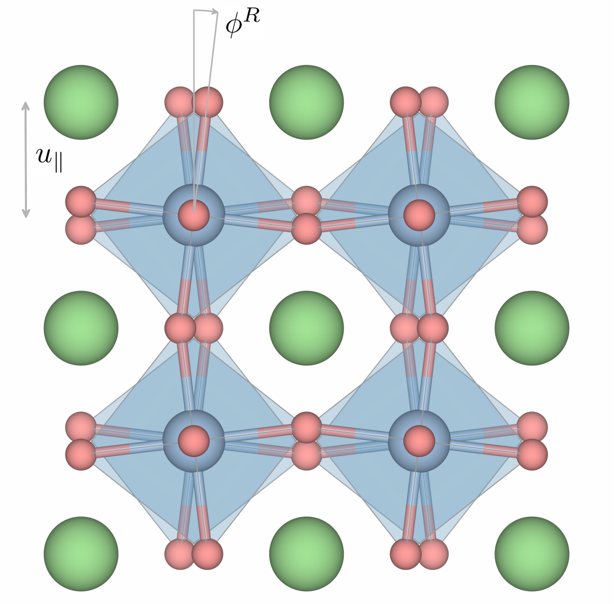

Figure 5.5: Visualisation of the R_{25} anti-ferrodistortive mode. The bond distance $u_{\parallel}$ between barium and oxygen, which can be measured in EXAFS, is also marked. Note that barium and oxygen are found in different planes such that $u_{\parallel}$ contains a component in the direction perpendicular to the plane.

5.2.9 Lattice stability

Although the dynamical matrix is Hermitian and as a consequence has only real eigenvalues, there is nothing preventing the existence of negative eigenvalues. Since the eigenvalue is the square of the frequency the existence of imaginary frequencies has to be addressed.

Assume that there is an eigenvalue $\omega_{s\mathbf{q}}^2 = -\gamma < 0$. Then $\omega = i\sqrt{\gamma}$ will be a purely imaginary number and the displacement (cf. Equations (5.15) and (5.29)) will behave as $\mathrm{e}^{\pm\gamma t}$. Any disturbance will grow exponentially and the crystal is not stable. This corresponds to a negative spring constant c in the one dimensional case. The force is not restoring but repelling and the larger the displacement the larger the repelling force.

Since it is a requirement that all vibrational frequencies be positive it is thus the formal criterion of lattice stability that the matrix of second order derivatives, the Hessian matrix, be positive definite. The presence of imaginary modes indicates that the investigated structure at $\{\mathbf{R_0}\}$, although at a stationary point as assumed in Equation (5.17), is not at an energy minimum but at a saddle point. The imaginary frequencies indicate that a lower energy structure can be found by displacing the atoms in the crystal along the phonon coordinate associated with the imaginary frequency [148].

An example of an imaginary mode is the R_{25}-mode in $SrTiO_3$ which has been extensively studied in first-principles phonon calculations. This mode is illustrated in Figure 5.5. In a cubic symmetry $SrTiO_3$ exhibits an imaginary R_{25}-mode frequency indicating that the cubic phase is not stable at 0 K. This instability causes a phase transformation to a tetragonal phase of $I4/mcm$ symmetry. Lattice instabilities are also at the core of both **Paper IV** and **Paper V**, where the anti-ferrodistortive R_{25}-mode of $BaZrO_3$ is investigated. A phase transition similar to that of $SrTiO_3$ also occurs in $BaZrO_3$ at sufficiently high pressure and is predicted also at zero pressure and zero kelvin for some xc-functionals.

5.2.10 Limiting case. Localised modes.

Despite the collective nature of phonons, there are cases where only a few atoms take part in a certain mode. These modes are called local or localised modes [149]. Localised modes were discussed briefly in Section 5.1.3 in the special case for the one-dimensional diatomic chain. A localised mode is a phonon mode concentrated in a region of space and is characterised by the fact that only a few atoms participate in the vibration while the rest of the lattice remains at rest. The eigenvector for such a mode will be non-zero only for a few elements, which typically are much lighter than all the others and will, to a good approximation, form a sub-matrix in a block diagonal dynamical matrix. The dynamical matrix in Equation (5.26) can thus be obtained as a limiting case of $M_j \to \infty$ for all $j \neq i$, where i is the lighter atom or atoms. If a mode is local most force constants will be close to zero and the dynamical matrix $D_{i\alpha,j\beta}(\mathbf{q})$ will span a relatively small space.

A local mode is typically also rather $\mathbf{q}$-point independent, and there is no need to go to reciprocal space. The vibrational mode is well enough represented at the Γ-point by the real space Force Constant matrix $F_{ni\alpha,mj\beta}$. By the argument above only a part of the FC-matrix needs to be computed in order to describe the vibrational mode [149, 150].

An example of such a local mode is the hydrogen mode in $BaTiO_{3-x}H_x$ which is shown in Figure 5.4c. A 3×3 Force Constant sub-matrix can be constructed by displacing only the hydrogen ion in three directions. By diagonalising only the non-zero sub-matrix the hydrogen vibrational frequencies and eigenmodes can be obtained.

In **Paper II** the localised hydrogen modes for $BaTiO_{3-x}H_x$ were obtained in this way for the HSE calculations. The eigenmodes could be deduced *a priori* from symmetry arguments. Since the mode is very local and contains only one atom, any interaction between atoms could be neglected both within the unitcell (with indices i, j) as well as between unitcells (with indices n, m). To stress this independence

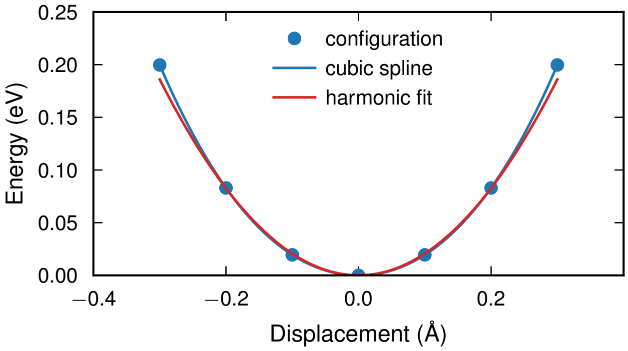

Figure 5.6: Illustration of one particle harmonic potential (OPHP) well mapping.

these indices have been dropped below. The terms in the FC sub-matrix

$$F_{\alpha\alpha} = \frac{\partial^2 V}{\partial u_\alpha^2} \tag{5.61}$$

were computed by fitting second order polynomials of type $\frac{1}{2}m\omega^2x^2$, where m is the mass of the atom, ω the vibrational frequency and x the displacement away from the equilibrium position, to the energy landscape obtained by displacing the ions in both positive and negative directions along the eigenvectors as illustrated in Figure 5.6. In **Paper II** the method is called the one particle harmonic potential (OPHP) method.

5.3 Measurable quantities derived from vibrations

5.3.1 Dynamical structure factor

The dynamical structure factor $S(\mathbf{q},\omega)$ is the thermal average of the Fourier transform in time and space of the time-dependent pair-correlation function of the scattering system. It is closely related to the differential cross-section $\partial\sigma^2/\partial\Omega\partial\varepsilon$ which can be measured from neutron scattering. In the incoherent approximation [151–154], which is used in **Paper II** and is tacitly assumed in the following, the relationship is particularly simple

$$\frac{\partial\sigma^2}{\partial\Omega\partial\varepsilon} = \frac{\sigma}{4\pi}\frac{k_f}{k_i}S(\mathbf{q},\omega) \tag{5.62}$$

Here k_i (k_f) the neutron wave-vector for the initial (final) neutron state and σ is the scattering cross-section.

Inelastic neutron scattering is primarily given by one phonon scattering events. The dynamical structure factor for one phonon scattering is [147, 151]

$$\begin{aligned} S_{(1)}(\mathbf{q},\omega) =& e^{-2W} \sum_s \frac{\hbar}{2M\omega_{\mathbf{q}s}} [\mathbf{q}\cdot\mathbf{e}_{\mathbf{q}s}]^2 \\ & \times \Big([1+n_{\mathbf{q}s}]\delta[\omega+\omega_{\mathbf{q}s}] + n_{\mathbf{q}s}\delta[\omega-\omega_{\mathbf{q}s}] \Big) \end{aligned} \tag{5.63}$$

Here M is the atomic mass, $\mathbf{e}_{\mathbf{q}s}$ is the eigenvector for mode s at the point $\mathbf{q}$, $\omega_{\mathbf{q}s}$ the corresponding frequency and $n(\omega) = [\exp(\hbar\omega/k_B T) - 1]^{-1}$ is the Bose-Einstein distribution factor. The delta function expresses the condition that energy transfer can occur only when the neutron energyloss or gain exactly matches the excitation energy of a phonon $\hbar^2/2m(k_i^2 - k_f^2) = \hbar\omega_s$. Thus, the first term, sometimes called *Stokes shift*, represents phonon creation and the second term, called *Anti-Stokes shift*, annihilation.

It is customary to apply the incoherent approximation, which has also been tacitly assumed above. In the incoherent approximation it is assumed that terms involving coherent scattering between atoms on different sites are neglected. Only the self-correlation is considered. Each atom and isotope has a unique cross section σ and the response to a neutron scattering event will depend on the cross-section of the individual atom. For example, the total neutron-scattering cross-sections of H, Ba, Ti, and O we use 82.0, 3.38, 4.35, and 4.23 barn, respectively [151]. The total dynamical structure factor in the incoherent approximation can be obtained by weighting the structure factors for the constituent atomic species with the corresponding total cross-sections

$$\begin{aligned} S_{(\mathrm{tot})}(\mathbf{q},\omega) \propto & \sum_i \sigma_i e^{-2W_i} \sum_s \frac{\hbar}{2M_i\omega_{\mathbf{q}s}} [\mathbf{q}\cdot\mathbf{e}_{i\mathbf{q}s}]^2 \\ & \times \Big([1+n_{\mathbf{q}s}]\delta[\omega+\omega_{\mathbf{q}s}] + n_{\mathbf{q}s}\delta[\omega-\omega_{\mathbf{q}s}] \Big) \end{aligned} \tag{5.64}$$

where i labels the atomic species.

In the case of a cubic crystal at low temperature the above expression can be simplified. First of all, only a very limited number of phonons are excited at low temperatures so we can make the approximation $n_s(\mathbf{q}) \approx 0$. Secondly, since the materials investigated in this thesis are all powder samples the powder average makes the directional dependence lost. Only the magnitude $q = |\mathbf{q}|$ of the momentum remains and $|\mathbf{q}\cdot\mathbf{e}_s^i|^2 = q^2|\mathbf{e}_s^i|^2$. Combined with the definition of the density of state (Equation (5.60)) we arrive at

$$S_{(\mathrm{tot})}(q,\omega) \propto \sum_i \sigma_i \frac{\hbar q^2}{2M_i} \frac{g_i(\omega)}{\omega} e^{-2W_i(q)} \tag{5.65}$$

Furthermore, the energy of the scattered neutron can in certain cases be assumed negligible and a relation between the phonon energy and neutron momentum can be written as $(\hbar^2 q^2)/(2m_n) = \hbar\omega$. This couples the two variables q and ω and the final expression can be written

$$S_{(\mathrm{tot})}(\omega) \propto \sum_i \sigma_i \frac{m_n}{M_i} g_i(\omega) e^{-2W_i(\omega)} \tag{5.66}$$

5.3.2 Debye Waller factor

The exponential factor in Equation (5.63) is known as the Debye-Waller factor. The effect of the Debye-Waller factor is to reduce the intensity in neutron spectroscopy both with increasing temperature and by increasing mode frequency. The Debye-Waller factor is related to the mean square displacement according to

$$\exp\left(-2W_i\right) = \exp\left(-\langle[\mathbf{q}\cdot\mathbf{u_i}]^2\rangle\right) \tag{5.67}$$

This equation can be simplified significantly. First by assuming powder average in a cubic crystal. Furthermore, in a cubic crystal $\langle u\rangle_x = \langle u\rangle_y = \langle u\rangle_z = \frac{1}{3}\langle u\rangle$

$$2W_i = \langle[\mathbf{q}\cdot\mathbf{u}_i]^2\rangle = q^2\langle u_{iq}\rangle^2 = \tfrac{1}{3}q^2\langle u_i\rangle^2 \tag{5.68}$$

Finally, the Debye-Waller factor can also be expressed using Equation (5.48) in terms of the density of state in a fashion similar to the previous section

$$2W_i = \frac{1}{3}q^2\langle u_i\rangle^2 = \frac{\hbar q^2}{2M_i}\int_0^\infty \mathrm{d}\omega \frac{g_i(\omega)}{\omega}\coth\left(\tfrac{1}{2}\beta\hbar\omega\right) \tag{5.69}$$

We see that the Debye-Waller factor not only reduces the intensity with increasing temperature due to the increased amplitude of $\langle u^2\rangle$, the intensity is also decreased with increasing vibrational frequency. The temperature effect can be taken care of by performing the experiments at low temperatures. For hydrogen, being a very light atom with large mean square displacement and high frequency, the Debye-Waller factor has important implications for the intensity. Fortunately, this is compensated by the large cross-section of hydrogen. However, as was seen in **Paper II**, the oxygen motion was clearly seen relative to the hydrogen intensity despite the significantly lower cross-section of oxygen.

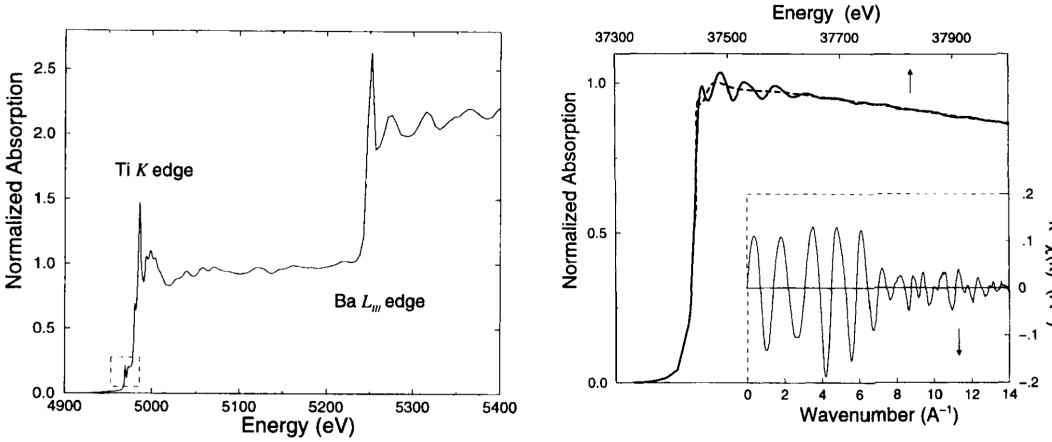

Figure 5.7: (left) The EXAFS spectrum of $BaTiO_3$ in an energy range spanning the titanium K edge at 4966 eV and barium L_{III} edge at 5247 eV. (right) The absorption spectrum for the barium K edge of $BaTiO_3$. The dashed line is the background function. The inset plots the fine structure $\xi(k)$, weighted by k^2 to show detail. (From Ref. [157] with permission.)

5.3.3 EXAFS

Extended X-Ray Absorption Fine Structure (EXAFS) is a technique based on the X-ray Absorption Spectroscopy (XAS) from which local structure can be deduced due to a diffraction-like phenomenon [155,156]. When X-rays sent into a sample match the binding energy of an electron of an atom the number of photons absorbed by the sample increases dramatically causing a peak in the absorption spectrum. An example of a full XAS spectrum for $BaTiO_3$ is shown in the left panel of Figure 5.7. The small oscillations, called fine-structure, on the high energy side of the peak are formed from interference between forward scattered and backscattered photoelectrons from nearby atoms [156]. The inset of the right panel of Figure 5.7 shows the fine structure modulation at the barium K edge of $BaTiO_3$ [157]. Since the range of correlation for electrons in a solid is very limited, EXAFS is a local structure technique. By clever application of the fourier transform [158] the small oscillations in the EXAFS spectrum can provide information on the local structure, such as bond distances, coordination number and chemical identity of the neighbouring atoms.

Similar to how the fluctuation in the position of an atom gives rise to a mean square displacement, the bond length exhibits a variance. These fluctuations in the mean square relative displacement (MSRD) in the direction parallel to the bond are denoted $\langle \Delta u_{\|}^2 \rangle$. The distance $u_{\|}$ for the first neighbour shell relative to barium is marked in Figure 5.5. The MSRD differs from the ordinary mean square displacement (MSD) insofar as that when MSD only measures the fluctuations of an atom around its equilibrium position on a macroscopic level the MSRD enables detailed information on a local level.

The MSRD can be computed [159] through

$$\langle \Delta u_{\parallel}^2 \rangle = \frac{1}{N}\frac{\hbar}{2\mu_{ab}}\sum_{\mathbf{q},s} |Y_{a,b}(\mathbf{q},s)|^2 \frac{1}{\omega(\mathbf{q},s)} \coth\frac{\hbar\omega(\mathbf{q},s)}{k_B T} \tag{5.70}$$

where

$$\begin{aligned} Y_{a,b}(\mathbf{q},s) = \Bigg[&\left(\frac{\mu_{ab}}{m_b}\right)^{1/2} \mathbf{e}_b(\mathbf{q},s) \exp(\mathrm{i}\mathbf{q}\cdot\mathbf{R}_{ab}) \\ &- \left(\frac{\mu_{ab}}{m_a}\right)^{1/2} \mathbf{e}_a(\mathbf{q},s)\Bigg] \cdot \hat{R}_{ab} \end{aligned} \tag{5.71}$$

Here m_a and m_b are the respective masses, μ_{ab} the corresponding reduced mass, $\mathbf{e}(\mathbf{q},s)$ is the eigenvector and $\omega(\mathbf{q},s)$ the eigenfrequency at the point $\mathbf{q}$ and bandindex s. $\mathbf{R}_{ab}$ is the vector connecting atoms a and b and $\hat{R}_{ab}$ the corresponding vector of unit length.

5.3.4 Dielectric constant

The dielectric constant of a material is a tensor measure of the materials response to an induced electric field. The static dielectric tensor can be computed as the sum of the electronic contribution $\varepsilon_{\alpha\beta}^{(el)}$ and the ionic contribution $\varepsilon_{\alpha\beta}^{(ion)}$[160]. The electronic contribution as well as the Born effective charges $Z_{\kappa,\alpha\alpha'}^{*}$ can be obtained from a linear response calculation [161,162] or a Berry's phase calculation [163–169]. The calculation of the ionic contribution also requires the eigenvectors $e_{\mu,\kappa\alpha'}$ and eigenfrequencies ω_μ of the dynamical matrix at $\mathbf{q} = 0$. These quantities can be readily obtained from a phonopy calculation[170].

We define the mode effective charge as [160]

$$Z_{\mu\alpha}^{*} = \sum_{\kappa\alpha'} \frac{Z_{\kappa,\alpha\alpha'}^{*} e_{\mu,\kappa\alpha'}}{\sqrt{m_\kappa}} \tag{5.72}$$

Here an additional sum over degenerate modes is implicit, i.e. if a mode is degenerate (two or three dimensional irreducible representation) they are considered as one. From the mode effective charge we also define (the ionic contribution to) the mode dielectric tensor

$$\epsilon_{\mu\alpha\beta}^{(ion)} = \frac{Z_{\mu\alpha}^{*} Z_{\mu\beta}^{*}}{\epsilon_0 \Omega_0 \omega_\mu^2} \tag{5.73}$$

where Ω_0 is the unit cell volume. The average mode dielectric constant is

$$\epsilon_{\mu}^{(ion)} = \frac{1}{3}\sum_{\alpha} \epsilon_{\mu\alpha\alpha}^{(ion)} \tag{5.74}$$

Here again, the sum over α also implies a sum over degenerate modes μ. Finally we compute the total dielectric constant as

$$\epsilon = \epsilon^{(el)} + \sum_{\mu} \epsilon_{\mu}^{(ion)} \tag{5.75}$$

which, by symmetry is only a constant times the identity matrix in 3 dimensions for a cubic crystal such as $BaZrO_3$. Hence there is no need to write out the tensor indices.

The high dielectric constant of $BaTiO_3$ was the first useful property found in a perovskite [3]. This was a highly sought after property in the early 40:s and the reason for its early application as a dielectric medium in capacitors.

5.4 Handling anharmonicity and temperature dependence

Harmonic approximation, which has been used up to this point, works well for many materials properties, such as the mean square displacement, but is insufficient for other properties. Perhaps most significantly, the harmonic approximation cannot account for thermal expansion. The simplest way to take anharmonicity into account is the *quasi harmonic approximation* [170].

The quasi harmonic approximation is based on the assumption that the harmonic approximation holds at every value of the lattice constant, which is treated as an adjustable parameter. Within the quasi harmonic approximation it is possible to compute, among other things, the thermal lattice expansion, which is out of reach within the harmonic approximation. However, also the quasi harmonic approximation fails ultimately when the temperature increases and the displacements away from equilibrium become too large. At this point higher order terms need to be included in the potential energy expansion in Equation (5.17) [171].

By varying the volume of the unit cell the vibrational free energy at each volume is computed through $F(T, V) \approx U_{\mathrm{el}}(V) + F_{\mathrm{vib}}(T, V)$. The Gibbs free energy is obtained through the minimisation of the free energy with respect to the volume $G(T, p) = \min_{V}[F(T, V) + pV]$. As a result the volume as a function of temperature $V(T)$ and the temperature dependent frequencies $\omega(V(T))$ are obtained.

The treatment is complicated by the presence of imaginary modes. As an example, Figure 5.4 shows the bandspectra of pristine cubic $BaTiO_3$ and $SrTiO_3$ along the high symmetry points illustrated in Figure 2.2. The phase transition of $BaTiO_3$ mentioned in Section 2.3 is clearly seen as imaginary frequencies (on the negative y-axis) at the Γ-point, but also along the entire paths connecting Γ, M and X. $SrTiO_3$ also exhibits this imaginary frequency at the gamma point showing that $SrTiO_3$ also, in principle, could be prone to a ferrodistortive transition [23]. However, in practise $SrTiO_3$ does not exhibit the ferrodistortive phase transition of $BaTiO_3$ [86] because of the R-mode instability which makes the TiO_6 octahedra in $SrTiO_3$ tilt into an anti-ferrodistortive phase described in Section 2.3. $BaTiO_3$ on the other hand is not prone to the anti-ferrodistortive transitions of $SrTiO_3$ due to the lack of imaginary frequencies at the R-point.

Since the cubic phase of $SrTiO_3$ is stable at some temperature it should in principle be possible to stabilise the cubic structure by renormalising the vibrational frequencies at the respective temperatures. Although some work has been attempted [172–180] there is still no simple, generally accepted first-principles approach to the temperature dependence of phase transitions.

5.5 Computational aspects

In order to solve the eigenvalue problem Equation (5.28) the quantity to be computed is the dynamical matrix, reprinted here for convenience,

$$D_{i\alpha,j\beta}(\mathbf{q}) = \sum_n \mathrm{e}^{-\mathrm{i}\mathbf{q}\cdot\mathbf{R}_n} \frac{1}{\sqrt{M_i M_j}} \frac{\partial^2 V}{\partial u_{ni\alpha} \partial u_{0j\beta}} \,. \tag{5.26}$$

Even though the original problem of diagonalising a $3 \times n \times N$ matrix (where N in principle is infinite) now has been reduced to diagonalising one matrix of size $3 \times n$ for each value of $\mathbf{q}$, the calculation of the dynamical matrix in Equation (5.28) is still immense. If the crystal is infinite the number of $\mathbf{q}$-vectors is in principle also infinite. However, it turns out that a judiciously chosen finite number of $\mathbf{q}$-points, e.g. using a Monkhorst-Pack [137] grid, works well enough. The symmetry of the lattice further reduces the number of $\mathbf{q}$-points at which a matrix has to be diagonalised to the irreducible Brillouin zone. The principle is the same as for the electronic structure in Section 4.6.2.

5.5.1 The supercell approach

Not only are the number of $\mathbf{q}$-vectors infinite, in an infinite crystal the sum over unit cells, N, is also infinite. Fortunately acceptable accuracy can often be obtained with a finite number of terms in the infinite sum over unit cells n in Equation (5.26), i.e. $\mathbf{R}_n$ is limited the period of a supercell of modest size. Which size is required must be determined from case to case, usually by performing full phonon calculations in supercells of different sizes until convergence of the phonon spectrum is reached. An example of such a convergence test for $BaZrO_3$ is shown in Figure 5.8. Here a $2 \times 2 \times 2$ supercell was deemed sufficient for convergence. Note that despite not being explicitly contained in the supercell, the zone-boundary R-point is well

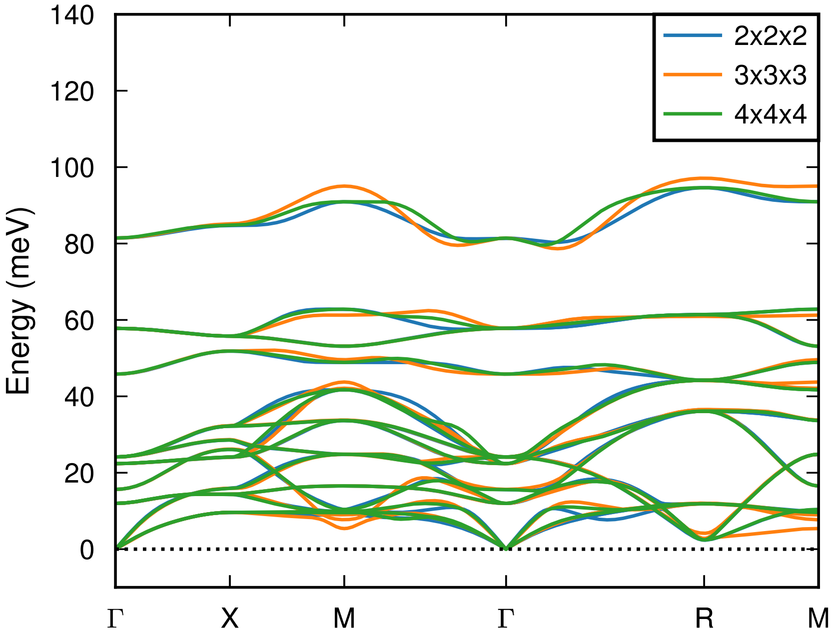

Figure 5.8: Illustration of supercell convergence for $BaZrO_3$ calculated with the PBE xc-functional.

represented also in a $3 \times 3 \times 3$ supercell. The M zone-boundary point on the other hand seems more long range and is less well represented in this supercell. The $2 \times 2 \times 2$ and $4 \times 4 \times 4$ supercells give identical results for the zone-boundary points. This is because the zone-boundary points are explicitly included and the $2 \times 2 \times 2$ supercell can accommodate the long range nature of these modes.

5.5.2 The frozen phonon approximation

In the present thesis the matrix elements are obtained using `phonopy` [170] which is a software implementation of the *frozen phonon* approach. In the frozen phonon approach the motion of the i:th atom is frozen in at a finite displacement δ and the forces on each ion are calculated from the relaxed electronic structure. This works rather well if the displacements are small enough not to violate the harmonic approximation but large enough for numerical accuracy. The forces are typically given as the Hellmann-Feynman forces directly from an electronic structure calculation. The matrix elements can be computed using finite differentiation and central differences.

$$\begin{aligned} F_{ni\alpha,0j\beta} &= \frac{\partial^2 V(\mathbf{u})}{\partial u_{ni\alpha} \partial u_{0j\beta}} = \frac{\partial}{\partial u_{ni\alpha}} \left(\frac{\partial V(\mathbf{u})}{\partial u_{0j\beta}} \right) = -\frac{\partial f_{0j\beta}(\mathbf{u})}{\partial u_{ni\alpha}} \\ &\approx -\frac{f_{0j\beta}\left(u_1, \ldots, u_{ni\alpha} + \Delta, \ldots, u_{3N}\right) - f_{0j\beta}\left(u_1, \ldots, u_{ni\alpha} - \Delta, \ldots, u_{3N}\right)}{2\Delta} \end{aligned} \tag{5.76}$$

6

Energy of point defect formation

> “ Textbooks and Heaven only are Ideal;
> Solidity is an imperfect state.
> Within the cracked and dislocated Real
> Nonstoichiometric crystals dominate. ”
>
> – John Updike [181]

The formation of a point defect can be regarded as a chemical reaction which, at constant pressure, p, and temperature, T, proceeds in the direction that lowers the Gibbs free energy defined as

$$G = U + pV - TS = H - TS \tag{6.1}$$

where U is the internal energy, V the volume and S is the entropy. H is the enthalpy, defined as $H = U + pV$.

If we consider the formation of n independent defects the change in free energy can be written as

$$\Delta G = n\Delta_f G - T\Delta_f S_{\text{conf}} \tag{6.2}$$

where $\Delta_f S_{\text{conf}}$ is the configurational entropy, the part of the entropy change associated with randomly distributing n defect in the material. $\Delta_f G$, the formation free energy for a single defect, can be written as

$$\Delta_f G = \Delta_f U + p\Delta_f V - T\Delta_f S \tag{6.3}$$

and is independent of the number of defects.

6.1 Defect formation energy

The formation free energy, $\Delta_f G$, can be separated into different contributions of chemical bonding and vibrational character [182]. The largest contribution is the formation energy, $\Delta_f E$, responsible for chemical bonding. The defect formation energy for a defect X in charge state q is defined as [67, 183]

$$\begin{aligned} \Delta_f E\left[X^q\right] = E_{\text{tot}}\left[X^q\right] - E_{\text{tot}}\left[\text{bulk}\right] + E_{\text{corr}}^q \\ - \sum_i \Delta n_i \bar{\mu_i} + q\left(\varepsilon_v + \mu_e + \Delta v_0\right) \end{aligned} \tag{6.4}$$

where $E_{\text{tot}}\left[X^q\right]$ is the total energy at zero kelvin from a supercell calculation including the defect and $E_{\text{tot}}\left[\text{bulk}\right]$ is the reference energy of the pristine material. E_{corr}^q is the energy correction which compensates for the spurious electrostatic interaction between charged defects in the supercell approach. There are several different correction schemes. **Paper II** makes use of the modified Makov-Payne correction scheme of Lany and Zunger [184]

$$\Delta E_{\text{corr}} = \frac{2}{3}\frac{Mq^2}{2\varepsilon L}, \tag{6.5}$$

where M is the Madelung constant, q is the charge, ε is the dielectric constant and L is the linear dimension of the supercell. The integer Δn_i is the number of atoms of type i that have been added ($\Delta n_i > 0$) or removed ($\Delta n_i < 0$) from the supercell in creating the defect, and $\bar{\mu_i}$ is the corresponding chemical potential. The chemical potential $\bar{\mu_i}$ is the reference energy of the reservoir with which the atoms are exchanged. If the reservoir is a gaseous phase the chemical potential can be computed from the expressions for a classical ideal gas. The electron chemical potential, μ_e, is often called the Fermi energy and is customarily given relative to the valence band maximum, ε_v. The additional term Δv_0 is used for properly aligning the electrostatic potentials of the bulk and the defect containing supercells [185, 186].

6.2 Chemical potentials for the gas phases

In a first approximation the chemical potentials for the gas phases $\bar{\mu_i}$ can be taken as the total energies from electronic structure calculations similar to $E_{\text{tot}}\left[X^q\right]$. This is marked by a bar in Equation (6.4) and would correspond to the free energy at zero kelvin, neglecting zero point effects. At finite temperatures the pressure dependence for the gas phases can be assumed to follow classical ideal gas behaviour. The chemical potential for a mono atomic gas can then be written as

$$\mu_i(p_i, T) = \bar{\mu_i} + k_{\text{B}}T \ln\left(\frac{p_i V_{\text{Q}}}{k_{\text{B}}T}\right) \tag{6.6}$$

where k_B is Boltzmann's constant, p_i is the partial pressure and $V_\mathrm{Q} = (2\pi\hbar^2/mk_\mathrm{B}T)^{3/2}$ is the quantum volume [67]. For molecules involving more than one atom additional terms containing vibrational and rotational degrees of freedom must also be taken into account.

The vibrational contribution contains a temperature independent part, the zero point energy, ε^ZP, which can be separated from the temperature dependent part. If the zero-point energy is computed within the harmonic approximation the zero point energy is $\varepsilon^\mathrm{ZP} = \sum_k \hbar\omega_k/2$, where ω_k are the molecular vibrational frequencies. These frequencies can be obtained from tables [187] or computed from first principle methods as described in Section 5.

The temperature dependence can be obtained by computing the full partition function, which is illustrated for the vibrational degrees of freedom in Section 5, but can also been taken, relative to the reference pressure p°, from thermodynamic tables [188] if shifted such that $h_i^\circ(0) = 0$. The full pressure and temperature dependence of the chemical potential for the gas phases can, under the assumption of ideal gas behaviour, be written as

$$\mu_i(p_i, T) = \bar{\mu}_i + \varepsilon_i^\mathrm{ZP} + h_i^\circ(T) - Ts_i^\circ(T) + k_\mathrm{B}T \ln\left(\frac{p_i}{p^\circ}\right) \tag{6.7}$$

6.3 Configurational entropy

While the formation energy must be positive for the material to be stable the configurational entropy must be large enough to lower the free energy to a negative value to enable defect formation. Without the configurational entropy there would be no defect chemistry.

Unfortunately, the configurational entropy is by nature extremely difficult to calculate since each configuration has a probability of the respective Boltzmann factor. This means that the energy of every possible configuration must be computed. One approximate approach is the cluster expansion technique in combination with Monte Carlo simulations and the Metropolis algorithm. However, since defect formation energies are often calculated in the dilute limit, i.e. in the limit where individual defects can be assumed to be independent of each other, it is possible to resort to a simpler first approximation to the configurational entropy, namely the ideal solution where all configurations have the same probability.

For n defects distributed on N sites with a degeneracy factor g accounting for the internal degrees of freedom of the point defect, the number of microstates is

$$\Omega = \frac{gN \cdot g(N-1) \cdots g(N-n+1)}{n} = g^n \binom{N}{n} \tag{6.8}$$

and the entropy can be written with the use of Stirling's approximation as

$$S = k_B \ln \Omega \approx n \ln g + N \ln \frac{N}{N-n} - n \ln \frac{n}{N-n} \tag{6.9}$$

Since T is always positive and $\Omega \geq 1$, the configurational formation entropy contribution to the free energy is always negative, thus favouring defect formation.

In the dilute limit the total free energy change ΔG is a function of the number of defects n only through the configurational entropy and can now be written as in Equation (6.2), restated here for convenience

$$\Delta G = n \Delta_f G - T S^{\text{conf}}(n) \tag{6.2}$$

An equilibrium is obtained when the derivative with respect to the number of defects is zero. The equilibrium condition then reads

$$\begin{aligned} \frac{\partial G}{\partial n} &= \frac{\partial}{\partial n} \Delta G \\ &= \Delta_f G + k_B T \left(\ln \frac{n}{N-n} - \ln g \right) = 0 \end{aligned} \tag{6.10}$$

It is convenient to introduce the defect concentration $x = n/N$. The equilibrium concentration is then given by

$$\frac{x_{\text{eq}}}{1 - x_{\text{eq}}} = g e^{-\Delta_f G / k_B T} \tag{6.11}$$

or if the concentration is very low ($x_{\text{eq}} \ll 1$)

$$x_{\text{eq}} = g e^{-\Delta_f G / k_B T} \tag{6.12}$$

6.4 Influence of configurational entropy on site probability

When one defect is introduced in a material translational symmetry is destroyed. The defect formation free energy $\Delta_f G \left[X^q \right]$ for an introduced second defect will in general differ depending on defect site. Some sites will be more energetically favourable than other. At zero kelvin the configuration with the lowest electronic energy E_{tot} becomes the most likely state (provided that differences in vibrational zero point motion is negligible). This does not mean that it is the most likely state also at finite temperature. As the temperature is increased the configurational entropy make also energetically unfavourable states accessible. A simple way to

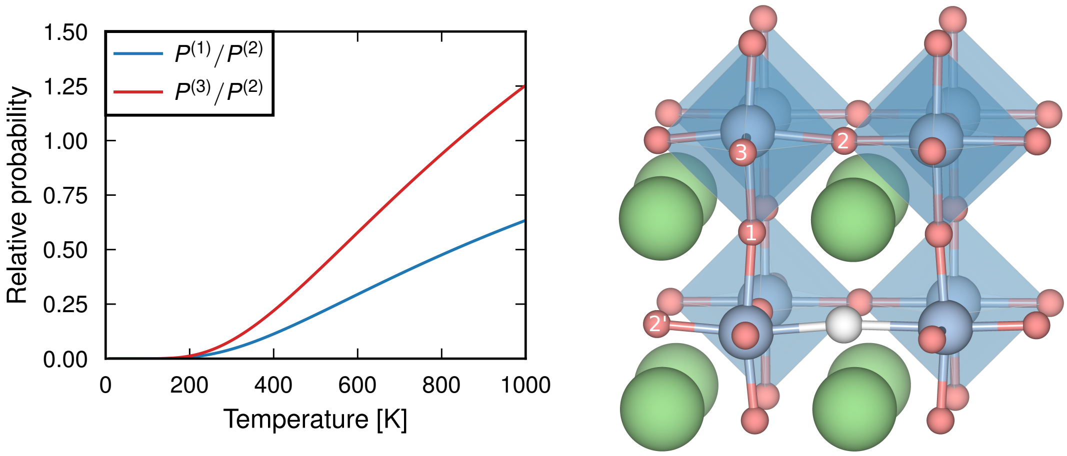

(a) (b)

Figure 6.1: (a) The relative site probability as a function of temperature for the three defects sites indicated in the illustration in (b).

account for the different configurational entropies of different defect sites will be discussed below.

The probability for site (†) to be occupied is given by the Boltzmann factor

$$P^{(\dagger)} \propto g^{(\dagger)} \exp\left(-\Delta_f G^{(\dagger)}/k_\mathrm{B}T\right) \tag{6.13}$$

Here $g^{(\dagger)}$ is the multiplicity of the site (†) counting all crystallographically equivalent sites. The defect formation energy $\Delta_f G\left[X^q\right]$ can be computed from Eq. (6.4), and could in principle include vibrational entropy, but not configurational entropy. However, since all terms in Eq. (6.4), except for the first, are equal for all defect sites these factor out and cancel when forming ratios. Therefore, it is sufficient to know $E_\mathrm{tot}\left[X^q\right]$ relative to some arbitrarily chosen reference level. The extension to include vibrational entropy is straight forward. The probability of a site is then just the summation over all energy levels given by the vibrational spectrum.

In **Paper III** the relative site probability for three different vacancy-hydrogen configurations is investigated. The second nearest neighbour site, marked 2 in Fig. 6.1a, is the energetically most stable site for the vacancy. However, the multiplicity of that site is only 4, to be compared with 8 for the first nearest neighbour site and 16 for the third nearest neighbour site. With increasing temperature the other sites become more and more likely until 837 K, above which the third nearest neighbour site has the highest probability. Also the first nearest neighbour site has a non-zero probability, although not as high as that of the third nearest neighbour. We thereby rationalise the observed peak at 100 meV as a signature of first nearest neighbour vacancies frozen in from the sintering process at higher temperatures. It should be noted that even if the multiplicity of the higher energy state had been lower than the lowest energy state, the higher energy state would still have a non-zero probability although it would then never exceed that of the lower energy state.

7

Phase Transitions

7.1 Thermodynamics of Phase Transitions

The crystal structure of phase attained by a material is determined by the free energy [189]. Setting aside meta-stable structures, which can exist if the energy barrier for transforming into the equilibrium structure is to high, the structure attained by the material at a given temperature and pressure is the one with the lowest free energy. At absolute zero, entropy effects, other than zero point motion, can be neglected and the free energy equals the enthalpy H. As the temperature is increased entropy becomes increasingly important until at some point a lower free energy can be attained if the material assumes a different phase. If the enthalpy of two phases differ by a latent heat ΔH the phase transition is called first order.

The phase transition temperature also depends on the applied pressure. By applying pressure it becomes favourable to attain the crystal structure with a smaller volume. This is the case for $BaZrO_3$. While $BaZrO_3$ remains cubic down to zero kelvin, as shown in **Paper IV**, $BaZrO_3$ undergoes a pressure induced phase transition at 17.2 GPa when measured at 300 K. This shows up as imaginary phonon modes at the R-point at sufficiently small lattice constants.

In Figure 7.1 the energy-volume curves for the three phases attainable from an R_{25}-mode instability in $BaZrO_3$ are shown. Here the energies and volumes are given relative to the reference values E_0 and V_0 given by the energy minimum and its corresponding volume of the cubic phase. As seen in Figure 7.1, for positive volumes (negative pressures) all phases have the same energy. This is because the lower symmetry phase differs from the cubic structure only by a Glazer rotation of the inscribed oxygen octahedron. The magnitude of the Glazer angle depends on the pressure where a larger angle is associated with a smaller unit cell volume. At negative pressure there is no energy gain associated with the reduction the unit cell

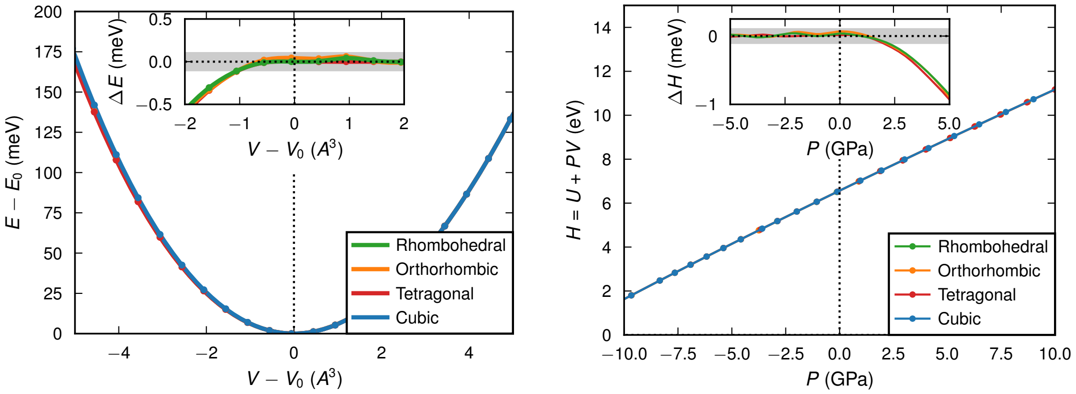

Figure 7.1: Energy as a function of volume (left) and enthalpy as a function of pressure (right) computed using the PBE functional for the three different phases attainable from an R_{25}-mode instability in BaZrO$_3$.

volume and all lower symmetry structures relax into the cubic phase. At higher pressures (smaller volumes) a finite angle will be energetically favourable and a phase transition occurs.

Based on the information shown in Figure 7.1, determination of the phase-transition pressure for BaZrO$_3$ is difficult. Rather than showing two distinctly separate parabolas for the energy as a function of volume, Figure 7.1 shows two practically overlapping parabolas. Similarly the two expected essentially straight lines with different slopes intersecting at a transition pressure have merged into only one. The insets show how the differences between energies and enthalpies of the lower symmetry structures and the cubic. Here the deviation as the pressure is increased is seen more clearly. However, the difference is in the meV range, below what is usually considered the accuracy of DFT. By also taking the accuracy of the calculations (marked by the shaded area in the figure) into account, determination of a phase transition pressure based on identification of the lowest enthalpy structure becomes difficult and other methods must be utilised. Since the different lower symmetry structures can be characterised by their Glazer angle the phase transition can be modelled as a continuous phase transition.

7.2 Free energy expansion

Many phase transitions can be expressed in terms of a continuous order parameter, often denoted q, which is a quantitative measure of the extent to which the phase transition has changed the structure [190, 191]. A first, and necessary, requirement for this formalism to be applicable is that the two phases have a group-subgroup relation, i.e. all the symmetry elements in the lower symmetry structure are contained in the higher symmetry structure [9].

We can now express the free energy as an expansion around $q = 0$

$$G(q) = G_0 + aq^2 + bq^4 + cq^6 + \dots \tag{7.1}$$

Due to the symmetry requirement $G(q) = G(-q)$ odd order terms can be excluded in a cubic crystal. This is referred to as a 2-4-6 potential after the exponents in q. It can almost always be assumed that c is small enough to be neglected for small values of q as long as b is positive. The equilibrium value of q is that which fulfils

$$\frac{\partial G}{\partial q} = 0 \; ; \; \frac{\partial^2 G}{\partial q^2} > 0 \tag{7.2}$$

When both coefficients a and b are positive, $G(q)$ has a single minimum at $q = 0$ and the free energy expansion describes the system in a high symmetry phase as its equilibrium. When a is negative (and b is positive) the expansion describes a system with a double well potential with a maximum at $q = 0$ and minima at non-zero values of $\pm q$ and the equilibrium phase is now the lower symmetry phase. A schematic of the free energy expansion is illustrated in Figure 7.2 for $T < T_\mathrm{C}$, $T = T_\mathrm{C}$ and $T > T_\mathrm{C}$. This is equivalent to $a < 0$, $a = 0$ and $a > 0$ as will be discussed below.

Usually, the higher symmetry phase is also the high temperature phase and as the temperature is lowered the lower symmetry phase is attained. Since the sign of a is crucial for determining the equilibrium phase it is reasonable to assume a simple relationship where the coefficient a decreases continuously with temperature and changes sign at the critical temperature T_C at which a phase transition occurs. The simplest relationship is $a = \tilde{a}(T - T_\mathrm{C})$, where $\tilde{a}$ is a positive constant. This allows a continuously increasing value of the order parameter at the phase transition.

When both a and b are negative it is important to include (the positive) 6th order coefficient c to make the expansion bounded from below. As long as a is negative the potential describes a double well potential similar to that discussed above, but when a becomes positive the expansion describes a triple-well potential, with three distinct local minima. Depending on the value of a the global minimum will be either at $q = 0$ or $\pm q$. In this case the order parameter jumps discontinuously at the phase transition at a finite value of $a > 0$.

When the values of the order parameter changes continuously through the phase transition it is denoted *continuous* or for historic reasons *second order*. If the order parameter makes a discontinuous jump to a non-zero value at the phase transition the transition is denoted *first order*. A note is in order here. With second order phase transition it is implied that $c = 0$ is a valid approximation. When $b = 0 < c$ the order is called tricritical.

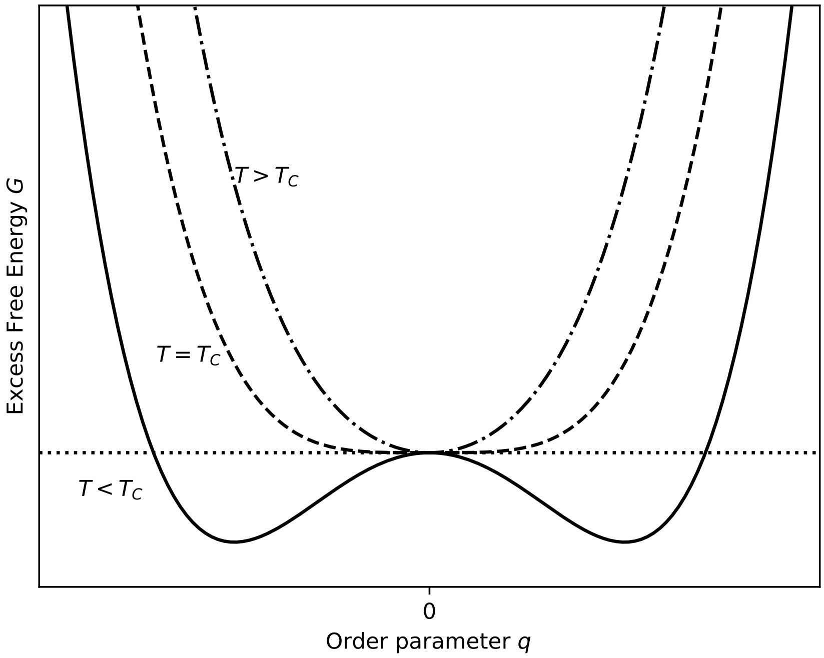

Figure 7.2: Schematic of the excess free energy as a function of the order parameter q at different temperatures T.

The final form of the expansion often goes under the name of *Landau expansion* or sometimes *excess free energy* since it describes the increase (decrease) of the free energy

$$G(q) = \frac{1}{2}\tilde{a}(T - T_{\mathrm{C}})q^2 + \frac{1}{4}bq^4 + \frac{1}{6}cq^6 \tag{7.3}$$

While there exist many subgroups to the high symmetry cubic phase, not all are attainable through a continuous phase transition. The second necessary requirement for a continuous phase transition is that $\frac{\partial G}{\partial \mathbf{q}} = 0$ has a solution for a non-zero q with $\frac{\partial^2 G}{\partial \mathbf{q}^2} > 0$ which is a global minimum [11]. To understand this we need to extend the expansion above to higher dimension. The extension is rather straight forward, but a subtlety is that different coefficients are allowed for the double derivatives with respect to the same variable and those including the cross derivatives.

Let us for example investigate the Landau expression

$$
\begin{aligned}
G = \frac{1}{2}a(T - T_{\mathrm{C}})(q_1^2 + q_2^2 + q_3^2) + \frac{1}{4}b(q_1^2 + q_2^2 + q_3^2)^2 \\
+ \frac{1}{4}b'(q_1^4 + q_2^4 + q_3^4) + \frac{1}{6}c(q_1^2 + q_2^2 + q_3^2)^4 + \dots
\end{aligned}
\tag{7.4}
$$

where $q = [q_1, q_2, q_3]$ is now vector valued. Here q_i can for example be a Glazer tilt angle around the three cartesian axes or a cation displacement. If the last term in Equation (7.4) is omitted the equilibrium condition can be written as

$$
\frac{\partial G}{\partial q_i} = a(T - T_{\mathrm{C}})q_i + b(q_1^2 + q_2^2 + q_3^2)q_i + b'q_i^3 = 0 \tag{7.5}
$$

which has the trivial solutions for $q_i = 0$, which we recognise as the high temperature solution or the saddle point at lower temperatures. Let us study three non symmetry-equivalent cases, $\mathbf{q} = \frac{q}{\sqrt{3}}[1,1,1]$, $\mathbf{q} = \frac{q}{\sqrt{2}}[1,1,0]$ and $\mathbf{q} = q[1,0,0]$. If q_i denotes the tilt angle around the three cartesian axes these cases would correspond to the structures $a^-a^-a^-$ ($R\bar{3}c$), $a^0b^-b^-$ ($Imma$) and $a^0a^0c^-$ ($I4/mcm$). The non-trivial solution is

$$
q_i^2 = \frac{a(T - T_{\mathrm{C}}) + b'}{nb} \tag{7.6}
$$

where n is the number of non zero elements in $\mathbf{q}$. Using this result the excess free energy can be written as

$$
G = -\frac{1}{2}a\frac{a + b'}{b} + \frac{1}{4}\frac{(a + b')^2}{b} + \frac{b'}{4n}\left(\frac{a + b'}{b}^{2}\right) \tag{7.7}
$$

The role of $q_1^4 + q_2^4 + q_3^4$ term is to distinguish the three different directions in order parameter space. Depending on the sign of b' the global minimum is attained for $n = 1$ or $n = 3$ for $b' < 0$ and $b' > 0$ respectively. We can see that $n = 2$ can never be a global minimum and hence $Imma$ ($a^0b^-b^-$) cannot be obtained through a continuous phase transition. The $q_1^4 + q_2^4 + q_3^4$ term also shifts the critical temperature in Equation (7.6) slightly such that the renormalized critical temperature is

$$
T_{\mathrm{C}}^* = T_{\mathrm{C}} - b'/a \tag{7.8}
$$

We will assume that b' is small and neglect this for the time being.

7.3 Spontaneous strain

During a phase transition the change the change in order parameter q is often accompanied by a spontaneous change in lattice constant. This is called *spontaneous strain* and must fulfil the symmetry of the phase transition. Following Refs. [9, 192–196] the excess free energy can be written as

$$\begin{aligned} G = \frac{1}{2}a(T - T_{\mathrm{C}})q^2 + \frac{1}{4}bq^4 + \frac{1}{6}cq^6 \\ + \frac{1}{2}\sum_{ik} c^0_{ik} e_i e_k + \sum_i \lambda_i e_i q^2 \end{aligned} \tag{7.9}$$

where the index on the order parameter q has been dropped. (See Refs. [9], [192] or [193] for the generalisation with vector valued q.) Here q is the order parameter, a, b, and c are the normal, or bare Landau coefficients, the first summation is over the elastic strain components and the second is the coupling between spontaneous strain and the order parameter. The elements of the stiffness tensor c_{ij} are in reality not constant when the order parameter changes, but in a first approximation we here assume they change very little and that their equilibrium values can be used. This is marked with a superscript 0.

In a cubic crystal there are only 3 independent non-zero components of c^0_{ik}: $c^0_{11} = c^0_{22} = c^0_{33}$, $c^0_{12} = c_{13} = c_{23}$ and $c^0_{44} = c^0_{55} = c^0_{66}$. All other $c^0_{ik} = 0$. It is therefore convenient to rewrite Equation (7.9) in terms of the the volume, tetragonal and orthorhombic stains

$$e_{\mathrm{a}} = (e_1 + e_2 + e_3) \tag{7.10a}$$

$$e_{\mathrm{t}} = \frac{1}{\sqrt{3}}(2e_3 - e_1 - e_2) \tag{7.10b}$$

$$e_{\mathrm{o}} = (e_1 - e_2) \tag{7.10c}$$

as

$$\begin{aligned} G =& \frac{1}{2}a(T - T_{\mathrm{C}})q^2 + \frac{1}{4}bq^4 + \frac{1}{6}cq^6 \\ &+ \frac{1}{4}\left(c^0_{11} - c^0_{12}\right)\left(e_{\mathrm{o}}^2 + e_{\mathrm{t}}^2\right) + \frac{1}{6}\left(c^0_{11} + 2c^0_{12}\right)e_{\mathrm{a}}^2 \\ &+ \frac{1}{2}\left(e_4^2 + e_5^2 + e_6^2\right) + \lambda_1^* e_{\mathrm{a}} q^2 + 2\lambda_2^* e_{\mathrm{t}} q^2 \end{aligned} \tag{7.11}$$

Here the relation between the coupling constants is

$$\lambda_1 = \lambda_1^* + \sqrt{3}\lambda_2^* - \frac{2}{\sqrt{3}}\lambda_2^* \tag{7.12a}$$

$$\lambda_2 = \lambda_1^* - \sqrt{3}\lambda_2^* - \frac{2}{\sqrt{3}}\lambda_2^* \tag{7.12b}$$

$$\lambda_3 = \lambda_1^* + \frac{4}{\sqrt{3}}\lambda_2^* \tag{7.12c}$$

A relation between the strain and the order parameter can be obtained for the equilibrium condition $\partial G/\partial e = 0$ as

$$e_\mathrm{a} = -\frac{q^2\lambda_1^*}{\frac{1}{3}\left(c_{11}^0 + 2c_{12}^0\right)} \tag{7.13a}$$

$$e_\mathrm{t} = -\frac{2q^2\lambda_2^*}{\frac{1}{2}\left(c_{11}^0 - c_{12}^0\right)} \tag{7.13b}$$

$$e_\mathrm{o} = 0 \tag{7.13c}$$

Substituting these equations back into equation (7.11), a new Landau like expression is found, with the coefficient b renormalised to b^*, as

$$G = \frac{1}{2}a(T - T_\mathrm{C})q^2 + \frac{1}{4}b^*q^4 + \frac{1}{6}cq^6 \tag{7.14}$$

With the addition of externally applied stresses, σ_i, with the customary sign convention of positive sign for expansive pressure, the contribution to the excess free energy, is $-\sum_i e_i\sigma_i$ and (remembering that $e_\mathrm{o} = e_4 = e_5 = e_6 = 0$) the expression is yet again modified to

$$\begin{aligned} G = \frac{1}{2}a(T - T_\mathrm{C})q^2 + \frac{1}{4}b'q^4 + \frac{1}{6}cq^6 \\ + P_\mathrm{a}e_\mathrm{a} + P_\mathrm{t}e_\mathrm{t} \end{aligned} \tag{7.15}$$

where

$$P_\mathrm{a} = -\frac{1}{3}(\sigma_1 + \sigma_2 + \sigma_3) \tag{7.16a}$$

$$P_\mathrm{t} = -\frac{1}{2\sqrt{3}}\left(2\sigma_3 - \sigma_1 - \sigma_2\right) \tag{7.16b}$$

7.4 Hydrostatic pressure

Let us now shift focus from an excess free energy as a function of temperature to a function of pressure. For a hydrostatic pressure the transition (critical pressure) occurs when the second order term changes sign. Substituting the strains from equation (7.13) the expression for the critical pressure can be defined as

$$P_{\mathrm{C}} = \frac{a\frac{1}{3}(c_{11}^0 + 2c_{12}^0)}{2\lambda_1^*}(T - T_{\mathrm{C}}) \tag{7.17}$$

Using this definition of P_{C} we can finally write the excess free energy in terms of the hydrostatic pressure as

$$G = \frac{1}{2}A(P_{\mathrm{C}} - P)q^2 + \frac{1}{4}Bq^4 + \frac{1}{6}Cq^6 \tag{7.18}$$

This result could have been obtained by the same type of reasoning used above for the Landau expansion since temperature and pressure occur on equal footing in the free energy expression, keeping in mind that pressure appears with a positive sign $G = U - TS + PV$, while temperature comes with a negative sign. Equivalently, the double well shape of the excess free energy is expected at lower temperature, but at higher pressures. The strength with the above argument is that it connects the two with a quantitative expression for the temperature development of the critical pressure P_{C}.

At equilibrium $\frac{\partial G}{\partial q} = 0$ the order parameter is given by

$$q^2 = \frac{1}{2C}\left(-B \pm \sqrt{B^2 + 4AC(P - P_c)}\right) \tag{7.19}$$

The negative solutions result in imaginary order parameter values and indicate (inversely to the soft mode frequency) stability for the cubic phase. In the limit when $C \to 0$ the phase transition is second order and

$$q^2 = \frac{A(P - P_c)}{B} \tag{7.20}$$

Combining this equation with equation (7.13b) a linear relationship between the tetragonal strain and pressure can also be obtained

$$e_{\mathrm{t}} = -\frac{2\lambda_2^*}{\frac{1}{2}(c_{11}^0 - c_{12}^0)}\frac{A(P - P_c)}{B} \tag{7.21}$$

Equations (7.20) and (7.21) constitute two discriminators for determining the phase transition pressure. This is illustrated in Figure 7.3.

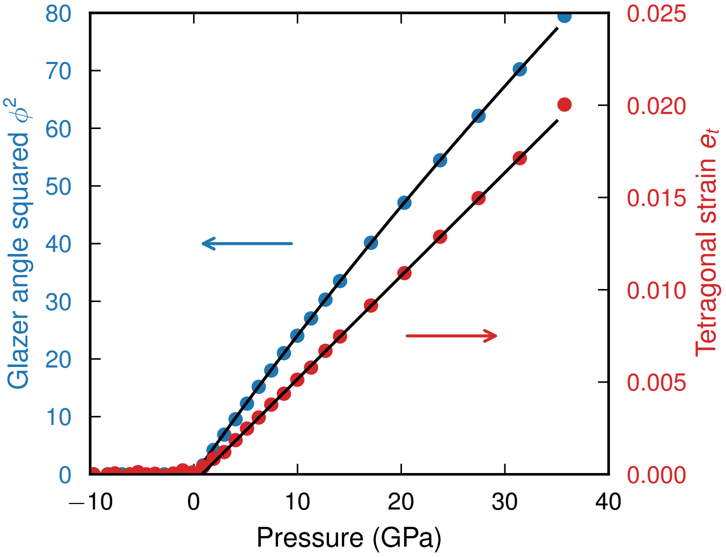

Figure 7.3: Illustration of the near pressure dependence of the square of the tilt angle according to Equation (7.19) and the almost perfect linear dependence for the tetragonal strain predicted by Equation (7.21).

7.5 Relation to soft mode frequency

In the harmonic approximation, the potential is expanded up to second order

$$V = V_0 + \frac{1}{2}\sum_{ij}\Phi_{ij}u_i u_j \tag{7.22}$$

A very natural choice of the order parameter q is the normal coordinates $Q_{s\mathbf{q}}$, which diagonalises the Hamiltonian. The harmonic potential can then be written as

$$\frac{1}{2}\sum_{ij}\Phi_{ij}u_i u_j = \frac{1}{2}\sum_{s\mathbf{q}}\omega^2_{s\mathbf{q}}Q_{s\mathbf{q}}Q^*_{s\mathbf{q}} \tag{7.23}$$

Now expressing the Landau potential in the normal coordinate of the R_{25} mode ($q \equiv Q_{s\mathbf{q}}\big|_{s\mathbf{q}=R_{25}} \equiv Q_{R_{25}}$) to harmonic order and we obtain the relation

$$\frac{1}{2}A(P_{\mathrm{C}} - P)q^2 = \frac{1}{2}\omega^2_{R_{25}}Q_{R_{25}}Q^*_{R_{25}} \tag{7.24}$$

i.e. that the square of the harmonic vibrational frequency is proportional to the applied pressure.

$$\omega^2 = \left.\frac{\partial^2 G}{\partial q^2}\right|_{q=0} = A(P - P_c) \tag{7.25}$$

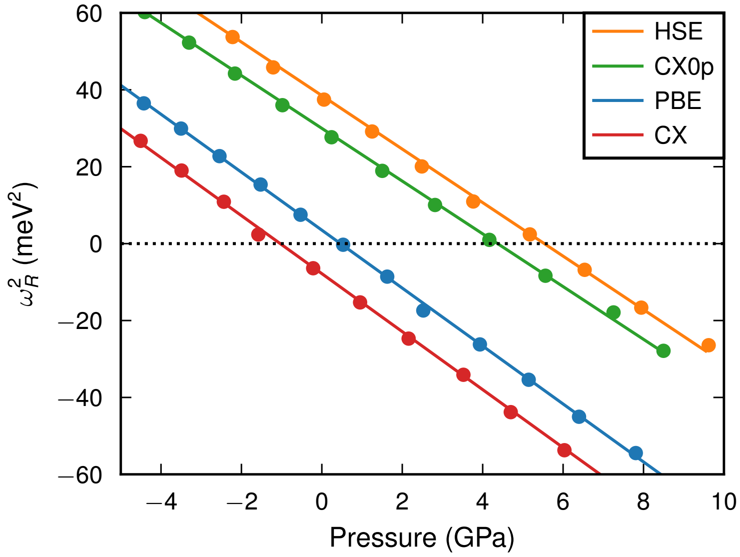

Figure 7.4: Illustration of the linear relationship between square of the harmonic vibrational frequency and the applied pressure (cf. Equation (7.25))

This shows that not only does the order parameter go to zero at the phase transition (see Equation (7.20) and Figure 7.3) but so does also the soft mode frequency squared. This is illustrated in Figure 7.4, where the correspondence to the phase transition pressure for the PBE functional determined from the tilt angle is confirmed.

However, and since $G(P)$ is defined in a multidimensional q-space we can expect the true transition pressure to be renormalised P_C^* (cf. Eq (7.8))

$$P_C^* = P_C + B'/A \tag{7.26}$$

Depending on the sign of B' the phase transition pressure could be shifted slightly. Since the assumed phase transition in $BaZrO_3$ is of type $n = 1$ B' should be negative and the measured phase transition pressure shifted to lower pressures. On the other hand, quantum fluctuations near the phase transition temperature will help stabilising the cubic symmetry and shift the measured phase transition pressure to higher pressures.

8

Chemical expansion

While the formation volume contribution to the formation free energy is negligible, the formation volume is significant when it comes to chemical expansion. As already mentioned in Section 3.2 the formation volume induces strain in the material upon defect formation. In a material where the composition changes constantly, such as in a proton conducting fuel cell membrane where the material is constantly hydrated and de-hydrated, this is particularly important. Chemical expansion is often measured as a unit cell volume change per defect, or per water molecule. This works well in (pseudo) cubic material where the strain can be considered isotropic, but does not capture the anisotropy or shear that a single defect may induce. To model this we have expressed the chemical expansion it terms of defect induced strain tensor in **Paper I**. Although it turned out that the strain tensors indeed were diagonal **Paper I** is written with precisely such a general case in mind.

8.1 A thermodynamics view on strain

Let us consider the crystal volume, $V = V(T, P, \{x_k\})$, to depend on the temperature, pressure and defect concentration of species k. In analogy with the thermal expansion coefficient and the bulk modulus mentioned above we now define the chemical expansion coefficient as [92]

$$\beta_k = \frac{1}{V}\left(\frac{\partial V}{\partial x_k}\right)_{P,T,x_{k'}\neq x_k} \tag{8.1}$$

In order to generalise the scalar chemical expansion coefficient to three dimensions, we first note that the volume expansion of a material in the small strain limit is given by the trace of the strain tensor [145, 197]

$$\frac{\Delta V}{V} = \mathrm{Tr}\left(\varepsilon\right) \tag{8.2}$$

By dividing by the change in defect concentration Δx_k and taking the infinitesimal limit we can write the chemical expansion coefficient as

$$\beta_k = \mathrm{Tr}\left(\frac{\partial \varepsilon}{\partial x_k}\right)_{P,T,x_{k'} \neq x_k} = \mathrm{Tr}\left(\lambda_k\right)_{P,T,x_{k'} \neq x_k} \tag{8.3}$$

where λ is the *defect induced strain tensor* in the infinite dilute limit [198].

8.2 The defect induced strain tensor

The defect induced strain tensor is the natural generalisation of the chemical expansion coefficient. In practical calculations with a finite concentration, we consider the effect of a single defect introduced in a volume V_0. With a defect concentration $x_d = \Omega_c / V_0$, where Ω_c is the volume of a primitive unit cell, the defect induced strain tensor is

$$\lambda = \frac{1}{x_d}\varepsilon \tag{8.4}$$

With this definition we get the chemical expansion coefficient as

$$\beta = \mathrm{Tr}\left(\lambda\right) = \frac{1}{x_d}\mathrm{Tr}\left(\varepsilon\right) = \frac{V_0}{\Omega_c} \cdot \frac{\Delta V}{V_0} = \frac{\Delta V}{\Omega_c} \tag{8.5}$$

and the defect formation volume is given by

$$\Delta_f V = \Omega_c \mathrm{Tr}\left(\lambda\right) \tag{8.6}$$

8.3 Strain in one dimension

The strain tensor appearing in Equations (8.3) and (8.4) is often calculated from the relative lattice expansion, the linear strain, for each axis in the crystal. In an isotropic cubic material, in which the defects can be assumed to be randomly oriented, causing no shear strain, the linear strains are all equal and are found along the diagonal in the three dimensional strain tensor. With the volume expansion in Equation (8.2) equal to the trace of the strain tensor the volume expansion can be written as three times the linear strain.

Consider therefore a one-dimensional object of initial length l_0. This can e.g. be the lattice constant in a cubic material. It is, by some means, forced into a new length l, which can be either larger or smaller than l_0. The elongation

$$\Delta l = l - l_0 \tag{8.7}$$

is defined such that it is positive (negative) if the length of the rod has increased (decreased). The strain is the dimensionless quantity

$$e = \frac{\Delta l}{l_0} \tag{8.8}$$

This is called the *engineering strain* [199] and is the measured quantity in an experiment. There is, in general, no reason to favour l_0 over l in the denominator and the engineering strain can just as well be defined with l in place of l_0. To relate the elongation to the original length of the rod , i.e. using l_0 in the denominator, is called the *Lagrangian strain measure* and relating the elongation to the final length, l, is called *Eulerian strain measure* [199].

Under the assumption that the strain is small the Lagrangian strain and the Eulerian strain are approximately equal, but under greater strain one would ideally measure the length l at every infinitesimal Δl in order to compute the logarithmic or *true strain*. The true strain is defined as

$$e = \int_{l_0}^{l} \frac{\mathrm{d}l'}{l'} = \ln\left(\frac{l}{l_0}\right) \approx \frac{l - l_0}{l_0} \tag{8.9}$$

where the last approximation is valid under small strain and takes us back to the engineering strain. The one-dimensional engineering strain is the average of the diagonal terms in the full strain tensor $e = \mathrm{Tr}(\varepsilon)/3$ and the chemical expansion coefficient can now be computed as

$$\beta = 3\frac{\Delta l/l_0}{x_d} = \frac{3e}{x_d} \tag{8.10}$$

8.4 Obtaining the strain tensor

When there is shear strain present, or when the crystal is not cubic the linear strain is not sufficient to describe the deformation of the crystal. Under such circumstances a formalism for a three dimensional body has to be used.

Assume a body in three dimensions can be described as a periodic lattice with a unit cell of basis vectors $\mathbf{a}_1, \mathbf{a}_1$ and $\mathbf{a}_3$. Let

$$\mathbf{a}_i = \mathsf{L}_0\,\mathbf{e}_i \tag{8.11}$$

be the one-to-one matrix transformation that maps the cartesian coordinates $\mathbf{e}_i$ onto the undeformed crystal $\mathbf{a}_i$. After deformation the crystal is defined by the new set of basis vectors

$$\mathbf{a}'_i = \mathsf{L}\,\mathbf{e}_i = \mathsf{L}\mathsf{L}_0{}^{-1}\mathbf{a}_i \tag{8.12}$$

The last equality follows because L_0 is one-to-one and Equation (8.11) is invertible.

The location of an arbitrary point $P = (p_1, p_2, p_3)$ as measured relative to the cell vectors in the undeformed crystal can be written as

$$\mathbf{r} = \sum_i p_i \mathbf{a}_i \tag{8.13}$$

and analogously after deformation. The displacement of the point is

$$\mathbf{u} = \mathbf{r}' - \mathbf{r} = \sum_i p_i \left(\mathbf{a}'_i - \mathbf{a}_i\right) = \big(\mathsf{L}\mathsf{L}_0{}^{-1} - 1\big)\,\mathbf{r} \tag{8.14}$$

The linear transformation $\mathsf{F} = \mathsf{L}\mathsf{L}_0{}^{-1}$ that maps the undeformed system onto the deformed is called the displacement gradient and can formally written as

$$\mathsf{F} = \frac{\partial r'_i}{\partial r_j} \tag{8.15}$$

from which the Biot strain tensor is defined as

$$\varepsilon_{ij} = \frac{\partial u_i}{\partial r_j} = \frac{\partial (r'_i - r_i)}{\partial r_j} = \frac{\partial r'_i}{\partial r_j} - \delta_{ij} = \mathsf{F} - \mathsf{I} \tag{8.16}$$

We can now recognise

$$\varepsilon = \big(\mathsf{L}\mathsf{L}_0{}^{-1} - 1\big) \tag{8.17}$$

in Equation (8.14) as the Biot strain tensor in the Lagrangian description of continuum mechanics.

A transformation of a three dimensional body can in general be decomposed in three different actions; translation, rotation and deformation. Translation, as well as rotation, can have no thermodynamical significance, since they do not alter the internal structure of the body. Translation are by construction not included. Rotations on the other hand can in principle be present since the Biot strain tensor is not by necessity symmetric.

Rotations can be removed through a symmetrization procedure. In general this can be done through a polar decomposition [199], but for small rotations it is sufficient to add the transpose and take the mean. The strain tensor is then given by

$$\varepsilon_{ij} = \tfrac{1}{2}\left(\frac{\partial u_i}{\partial r_j} + \frac{\partial u_j}{\partial r_i}\right) \tag{8.18}$$

or in matrix notation

$$\varepsilon = \tfrac{1}{2}\left(\mathsf{L}\mathsf{L}_0^{-1} + \left(\mathsf{L}_0^{-1}\right)^T (\mathsf{L})^T\right) \tag{8.19}$$

However, if no rotations are present there is no reason to favour one strain tensor over another and the strain tensor can be computed as the Biot strain tensor

$$\varepsilon = \left(\mathsf{L}\mathsf{L}_0{}^{-1} - 1\right) = (\mathsf{L} - \mathsf{L}_0)\,\mathsf{L}_0{}^{-1} \tag{8.20}$$

This is the natural generalisation of the engineering strain in Equation (8.8) to three dimensional objects.

9

Summary of appended papers

> “ Wer Großes will, muss sich zusammenraffen;
> in der Beschränkung zeigt sich erst der Meister,
> und das Gesetz nur kann uns Freiheit geben.[1] ”
>
> – Johann Wolfgang von Goethe, Natur und Kunst

9.1 The size and shape of a defect

The volume of a defect, and how to properly describe the shape of a defect, is investigated in **Paper I** for $BaZrO_3$. The strain tensor formalism, which describes not only the size, i.e. the ionic radius, but also the anisotropy induced by the defect is developed. The trace of the strain tensor is directly related to the volume of the defect from which an ionic radius can be obtained. The strain tensor is general and applicable to any point defect in any material describing not only the volume expansion but also the anisotropy.

The strain tensor formalism is applied to the defects involved in hydration of $BaZrO_3$ i.e. the proton and the oxygen vacancy, including some acceptor dopants necessary for the formation of the vacancies. The difference in ionic radius between the hydroxide ion and the vacancy causes the material to expand during hydration. We conclude that the vacancy is smaller than the oxygen host ion but more interestingly, also the hydroxide ion is smaller than the oxygen ion. The cause of the chemical expansion during hydration is not the large size of the proton, but the

---

[1] Whoever seeks greatness must gather himself together, only in limitation does the master distinguish himself, and only the law can give us freedom

relatively small size of the vacancy. An important side result is that the strain tensor is rather independent of the acceptor dopant species as well as the supercell size.

The strain tensor is also applied in **Paper II** to the oxyhydride $BaTiO_3$ as an independent discriminator for the polaron state. The difference in chemical expansion between the oxyhydride in the bandstate and in the polaron state is about a factor two, leading to the conclusion that the chemical expansion determined from measurements of the lattice constants implies a bandstate configuration.

9.2 Understanding the oxyhydride $BaTiO_{3\text{-}x}H_x$

The substitutional hydrogen $H_O^{\bullet}$, which can form in $BaTiO_3$, consists of a negatively charged H^- ion on an oxygen site and leads to n-type doping of the material. Doping into the initially empty Ti 3d band should according to band theory lead to a delocalised electron. However, through coupling to phonons it can also lead to a polaron.

In order to localise an electron and form a polaron the DFT+U method is used. The value of the U-parameter was determined self-consistently through applying the criterion of piecewise linearity to the xc-functional. The exact value of the U-parameter is not transferable between different systems and we find that the optimum U-value is different in a $2 \times 2 \times 2$ supercell ($U = 3.3$) and a $3 \times 3 \times 3$ supercell ($U = 3.1$). Polaron formation is found to be energetically favourable ($\Delta E = -57$ meV) in the smaller supercell, but unfavourable ($\Delta E = 124$ meV) in the larger. This can perhaps be interpreted as an indication of a concentration dependence for the polaron formation energy. We conclude that the formation energy is not sufficient do determine whether polarons are present or not in the oxyhydride.

The hydrogen local environment differs significantly between the polaron and the bandstate. This has a large impact on the vibrational character of the hydride ion and the vibrational properties of the hydride ion changes significantly when a bound polaron is formed on the nearest neighbour titanium. For both states the hydrogen vibrational modes are found to be highly localised and decoupled from the lattice and thus easily distinguishable.

The PBE functional turns out to be insufficient at accurately predicting the vibrational frequencies of pure $BaTiO_3$. The HSE hybrid functional on the other hand is shown to produce more accurate vibrational frequencies. Since the vibrational frequencies are highly localised the One Particle Potential method (also known as the Partial Hessian approach) has been used. This method requires fewer displacements, only one displacement of the hydrogen atom in each of the three cartesian directions, and consequently fewer calculations.

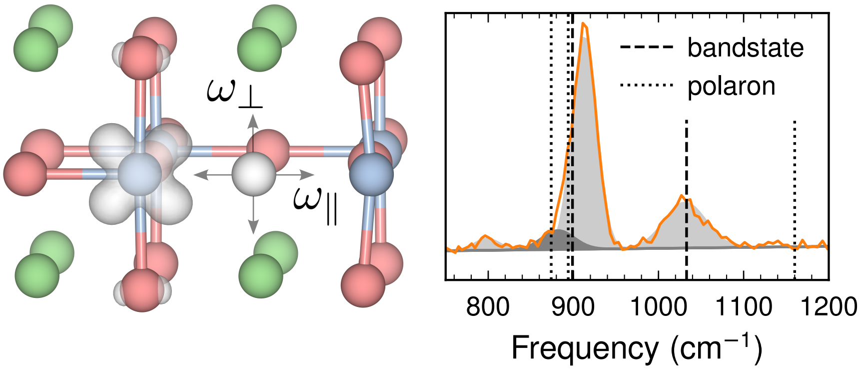

Figure 9.1: Close up of the measures INS spectrum in the interval 700–1250 cm^{-1}. Frequencies calculated with HSE are marked with dashed (bandstate) and dotted (polaron) lines. Gaussian fits are indicated by shaded areas.

In **Paper II** we discriminate between the two possible electronic states, the delocalised bandstate and the localised polaron state. The agreement between the calculated vibrational frequencies and the measured inelastic neutron scattering spectrum is excellent and leads to the conclusion that the conduction electrons in the measured sample are predominantly delocalised.

As an independent confirmation of the conclusion we computed the strain tensor for the two states. We find that the strain tensor agrees very well with the bandstate but that polarons are highly unlikely in unstrained material.

While a a bound polaron on the nearest neighbour titanium changes the vibrational frequencies significantly, the presence of oxygen vacancies does not. This is shown in **Paper III**. Only when an oxygen vacancy is formed in closest possible proximity to the hydride ion can a shift of the vibrational frequencies be observed as a peak at 800 cm^{-1}. This configuration is not energetically favourable, however, and is only found at elevated temperatures. Thus the presence of nearest neighbour oxygen vacancies at lower temperatures can only be explained by assuming that oxygen mobility is limited and that these configurations are formed during the sintering at 600 °C.

9.3 Understanding anti-ferro distortions in $BaZrO_3$

The presence of imaginary modes in the phonon dispersion of $BaZrO_3$ indicates an instability of the cubic phase. Since the imaginary mode is at the R-point, more specifically the R_{25} irreducible representation, the instability is anti-ferrodistortive, leading to a transition into a tetragonal phase. No such phase transition has been

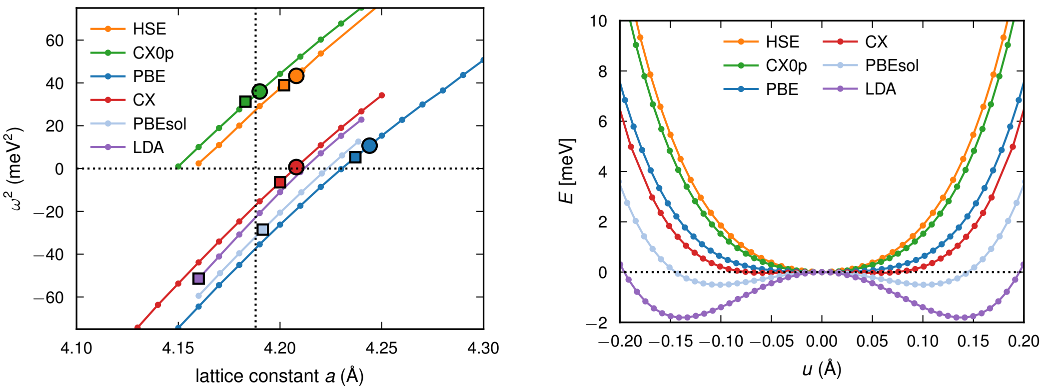

Figure 9.2: (left) The square of the R_{25}-mode frequency as a function of lattice constant for the six different functionals. The equilibrium lattice constant is marked by a square and the zero point energy corrected lattice constant obtained from a quasi harmonic approximation is marked by a circle (right). The potential energy surface (PES) along the R_{25} phonon mode. The curvature of the PES is directly proportional to the square of the R_{25}-mode frequency.

seen experimentally.

As seen in Figure 9.2 the magnitude of the R_{25}-mode frequency is different in different functionals. The R_{25}-mode frequency is also strongly lattice constant dependent and for the non-hybrids the magnitude ranges from the largest instability predicted by LDA to PBE, which does not predict any instability. As seen in Figure 9.2 the lattice constant is the largest effect and can almost entirely explain the difference between LDA, PBEsol and PBE. Inclusion of non-local exchange causes a significant shift in the R_{25}-mode frequency while inclusion of non-local correlation only has a minor effect.

Many early works used LDA and found discrepancies between experiments and theory, while later works have relied on PBE, or sometimes a $3 \times 3 \times 3$ supercell, to prevent octahedral rotations and thus circumvent the problem. With standard functionals exhibiting qualitatively different behaviour two questions arise: which is the crystal structure of $BaZrO_3$ at zero kelvin and which functional can accurately predict this?

In **Paper IV** we address the question of the $BaZrO_3$ ground state structure. By combining results from inelastic neutron scattering experiments on a powder sample with the calculated phonon dispersion using different functionals we can extract the R_{25}-mode and accurately determine the R_{25}-mode frequency as a function of temperature, down to 5 K. We thereby conclude that $BaZrO_3$ is cubic down to zero kelvin with a R_{25}-mode frequency of about 6 meV. Thus, although often denoted *soft*, the R_{25}-mode is not soft. We also both calculate and measure the mean square displacement and momentum distribution, both of which show only small differences between the different functionals, but more importantly, good agreement with the experimental values.

In **Paper V** we present an extended set of properties and compare them with measurements found in the literature. Once again we find a set of properties, such as the elastic constants, which show good agreement with the experimental values for all investigated functionals. These results are obtained in the cubic symmetry and are fully consistent with a cubic ground state structure of $BaZrO_3$. However, we also identify a set of properties where the different functionals predict different values. Perhaps the most interesting ones are the dielectric constant and the parallel mean square relative displacement, where earlier works have failed to achieve agreement between computational and measured values. This failure has previously been interpreted as an indication of a different crystal structure.

We show that there is no need to go beyond the assumption of cubic symmetry for an accurate description for a wide range of measurable $BaZrO_3$ properties. Using hybrid functionals we achieve agreement between experimental measurements and theoretical predictions in the cubic crystal structure. Both the Γ-point frequencies, the dielectric constant and the EXAFS measurements of the parallel mean square relative displacements can be accurately described computationally within the cubic symmetry. By the inclusion of Fock exchange (in HSE and CX0p) the calculated values are in very good agreement with the experimental values.

An independent confirmation of the stability of the cubic ground state of $BaZrO_3$ is given by the observed pressure-induced phase transition at room temperature. In **Paper V** we predict that such a pressure-induced phase transition at zero kelvin would lead to a tetragonal $I4/mcm$ symmetry at high pressures in accordance with the observation. This would be similar to the well-studied anti-ferrodistortive phase transition exhibited by $SrTiO_3$ at 105 K and ambient pressure. Using Landau theory for continuous phase transitions we predict the phase transition pressure at zero kelvin using three different discriminators.

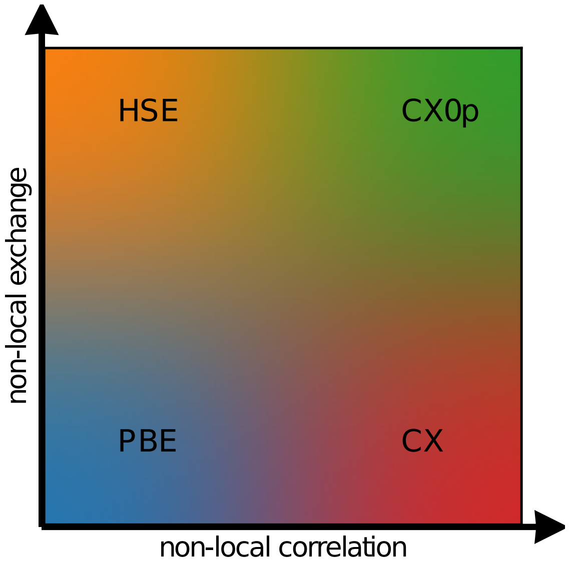

Figure 9.3: Illustration of the functional square

9.4 The role of non-local exchange and non-local correlation in the description of vibrational frequencies and the phase transition of BZO

The four approximations to the exchange-correlation functional investigated in **Paper IV** and **Paper V** can be represented as a 2 × 2 square as illustrated in Figure 9.3. Letting PBE represent one corner in which both correlation and exchange are treated semi-locally, the inclusion of non-local correlation along the horizontal axis is represented by CX, and the inclusion of non-local exchange along the vertical axis by HSE. The simultaneous inclusion of both non-local exchange and non-local correlation is represented by CX0p. This allows us to investigate the effect of including non-local exchange and non-local correlation separately.

Figure 9.4 summarises the results. A general observation is that non-local Fock-exchange significantly improves the description of the vibrational properties in both $BaZrO_3$ and $BaTiO_3$. This is in agreement with the literature [200, 201]. In **Paper II** we conclude that Fock exchange is necessary for an accurate prediction of the hydrogen vibrational frequencies ($\omega_{H^\bullet_O}$) in the oxyhydride $BaTiO_3$. Similarly, in **Paper IV** we again find that Fock exchange is necessary for an accurate prediction of the R_{25}-mode frequency. Fock exchange is also essential for a range of properties directly affected by the vibrational properties of the material, as discussed in **Paper V**. However, as also discussed below and in **Paper V**, inclusion of non-local correlation effects are beneficial, although the effect is smaller.

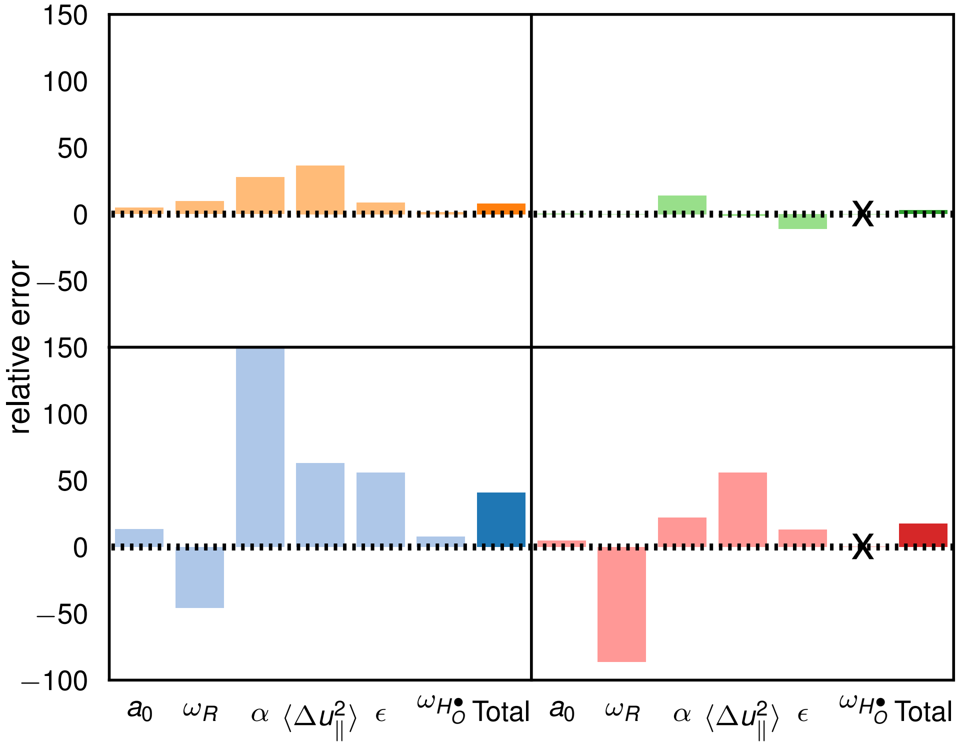

Figure 9.4: The assessment square comparing the prediction from of the functionals HSE (top left), CX0p (top right) PBE (bottom left) and CX (bottom right) with the available measurements. The bars indicate the relative error in percent compared with experiments for the lattice constant a (magnified 10 times), the R_{25}-mode frequency ω_R, the dielectric constant ϵ, the oxygen-barium MSRD at 300 K $\langle \Delta u_{\|}^2 \rangle_{\text{BaO}}$ and the root mean square average thermal expansion. The penultimate column shows the relative error of the hydride ion vibrational frequencies in oxyhydride BaTiO_3. The last column shows a root mean square error summarising the previous columns.

The dielectric constant ϵ also proves to be an excellent discriminator between the different functionals. The poor performance of LDA, which has led to suggestions of a different ground state crystal symmetry at zero kelvin, is inherited by PBE. The inclusion of Fock-exchange in HSE significantly improves the prediction of the dielectric constant. This is in line with the general observation that the inclusion of Fock-exchange improves the predictive power of the functional.

What is more interesting is that inclusion of non-local correlation has a rather significant effect. This is interesting because the difference can be traced back to the differences in the dynamical matrix and not only to the difference in the vibrational frequencies. While the differences in the dynamical matrix upon inclusion of non-local exchange is small the difference upon inclusion of non-local correlation is significant. The former leads to a significantly improved prediction of the dielectric constant, mostly due to the improved prediction of the vibrational frequencies. The effect of the latter is far less obvious and is to an almost equal amount due to a change of the eigenvectors.

The oxygen-barium parallel mean square relative displacement (MSRD) $\langle \Delta u_{\parallel}^2 \rangle_{\mathrm{BaO}}$ also proves to be an excellent discriminator of the different functionals. The MSRD is strongly dependent on a correct determination of the R_{25}-mode frequency. With increasing temperature, modes with lower vibrational energy will be more easily populated and a stronger temperature dependence is expected for xc-functionals exhibiting a lower R_{25}-mode frequency. This is also partly true. While all functionals predict similar MSRD valued as zero kelvin, both PBE and CX exhibit a strong temperature dependence. However, this is also the case for HSE, which proves that the simplified picture of the MSRD being a measure of the R-point instability is insufficient. In fact, the MSRD is again a property where truly non-local correlation becomes important. This is particularly interesting since the effect of truly non-local correlation is usually considered more important in sparse matter while $\mathrm{BaZrO_3}$ is not sparse.

The common denominator for these two properties, the MSRD and the dielectric constant, is that the calculation of said properties explicitly includes the eigenvectors of the dynamical matrix. In **Paper V** we show that the inclusion of non-local correlation significantly changes the dynamical matrix, while the change due to inclusion of non-local Fock-exchange is smaller. This is somewhat curious since the effect on the observable properties is the opposite. It seems that, in the MSRD and the dielectric constant we have found two excellent discriminators between the different functionals. Furthermore, it seems that the dynamical matrix and its eigenvectors are where we should probe to elucidate the role of truly non-local correlation.

10

Conclusions and Outlook

> “ The game of science is, in principle, without end. He who decides one day that scientific statements do not call for any further test, and that they can be regarded as finally verified, retires from the game ”
>
> – Karl Popper [202]

In this thesis we have seen two examples of how first principles calculations can be used to penetrate a material and provide information about the local environment. We have also seen how this affects macroscopic properties in a material.

In **Paper I** the chemical expansion, which is a difference in ionic volume between two different types of defects, could be separated into the formation volume of the two defects individually. Due to the charged nature of the defects this information is not easily accessible through experiments. The agreement between the measured and calculated chemical expansion supports the conclusion that the chemical expansion can be understood from the separation into two individual effects. However, the agreement is not perfect and there are important effects which are neglected in the article, such as finite temperature and the quantum fluctuation of hydrogen. Moreover, in charged supercells, such as those used here, there is a fictitious pressure which depends on the specific implementation [203]. While the effect should cancel for the modelling of the overall chemical expansion during hydration, the individual defect volumes for the proton and the oxygen vacancy will in principle differ between different DFT implementations. A proper modelling of this effect requires further work.

In **Paper II** and **Paper III** the oxyhydride barium titanate was investigated. Our calculated vibrational spectrum is in good agreement with the spectrum measured using inelastic neutron scattering. There is no signature from the O-H stretch confirming that hydride ions occupy the oxygen site and that oxygen vacancies in the lattice have only a minor impact on the hydrogen vibrational. We also refute the hypothesis that small bound electron polarons would form in unstrained oxyhydride $BaTiO_3$.

The oxyhydride $BaTiO_3$ is still a rather recent discovery and many aspects remain to be understood. Most importantly for a practical application is perhaps the elementary diffusion step, and thus the hydride exchange mechanism. The apparent thermodynamical instability also needs further investigation. Also the apparent semi-conducting behaviour of epitaxial $BaTiO_3$ lacks an explanation. It is not unlikely that polarons could form in an epitaxially strained material. Furthermore, additional types of hydrogen defects may be present in the material. For example the presence of substitutional dihydrogen, i.e. a hydrogen molecule or two hydrogen ions, on any type of site, including the barium or titanium sites.

In **Paper IV** and **Paper V** we claim to have settled a long outstanding question of the ground state structure of $BaZrO_3$. In **Paper IV** we measure the R_{25}-mode frequency and find that the cubic crystal structure is stable. The agreement between the simulated neutron scattering map based on the CX0p functional is in remarkable agreement with the measurement. In **Paper V** we continue assessing the functionals against a broader set of experimental values found in the literature. The strong agreement between the predicted and measured values, at least for the hybrid functionals and in particular for the CX0p, leads us to conclude that $BaZrO_3$ is indeed cubic down to zero kelvin.

At the same time, these two articles lead to new questions. For example, why are the dynamical matrices for HSE and CX0p so different, and why is this not reflected more strongly in the predicted properties? Another question which remains unsettled is the extent to which the zero point energy can stabilise a higher symmetry structure. How deep must a double well potential be before a phase transformation is inevitable?

It has been argued that $BaZrO_3$ should exhibit a shallow double well potential, which is stabilised by quantum zero point motion. Since the R_{25}-mode in $BaZrO_3$ turned out to be far from soft, and the ionic potential energy landscape very close to harmonic, the question of zero point energy stabilisation turned out rather semantic. However, the question of to which degree a weak instability can be stabilised by zero point motion remains.

Many perovskites, e.g., $SrTiO_3$, exhibit double well potentials in DFT deep enough to cause phase transformations when the temperature is lowered. The phase transformation in $SrTiO_3$ occurs at 105 K and is of the same type as the phase transition investigated in **Paper V** for $BaZrO_3$. The temperature-pressure phase diagram has also been rather extensively studied experimentally for $SrTiO_3$. Taking temperature effect into account in the modelling of the pressure-induced phase transition in both $SrTiO_3$ and $BaZrO_3$ is the natural next step. The question is also of general interest. A solid approach to modelling temperature effects based on DFT data, and in particular temperature induced phase transitions, both at high and and low temperatures, remains an open question.

A

Description of relevant crystal structures

> “If you want to understand *function*, study *structure*.”
>
> – Francis Crick [204]

A.1 Cubic $Pm\bar{3}m$ (221)

The ideal perovskite crystal structure, from which all other structures can be derived, is called the *aristotype*. It has space group $Pm\bar{3}m$ which is No. 221 in the International Tables for Crystallography [205]. The point group in Schönflies notation is O_h^1. The atomic positions are described by their Wyckoff site is A ($1a$), B ($1b$) and O ($3c$). This structure, illustrated in figure A.1, consists of two interpenetrating simple cubic lattices of A and B atoms respectively shifted such that the origin of one lattice is the body centre of the other with oxygen on the faces of the A-lattice. The oxygen atoms thus form an inscribed octahedron, the dual to the cube, with the B atom at its centre.

It should be noted that it is also possible to shift the origin to the B-atom without loss of generality, since both the $1a$ and the $1b$ Wyckoff site as well as the $3c$ and $3d$ Wyckoff sites have the same symmetry, O_h and D_{4h}, respectively. In this case the respective Wyckoff sites become A ($1b$), B ($1a$) and O ($3d$) and the oxygen atoms now occupy positions along the edges of the cube. Which convention is used is of importance for the characterisation of the irreducible representations in Appendix B. All other lower symmetry structures contain the B atom at the centre of the point group.

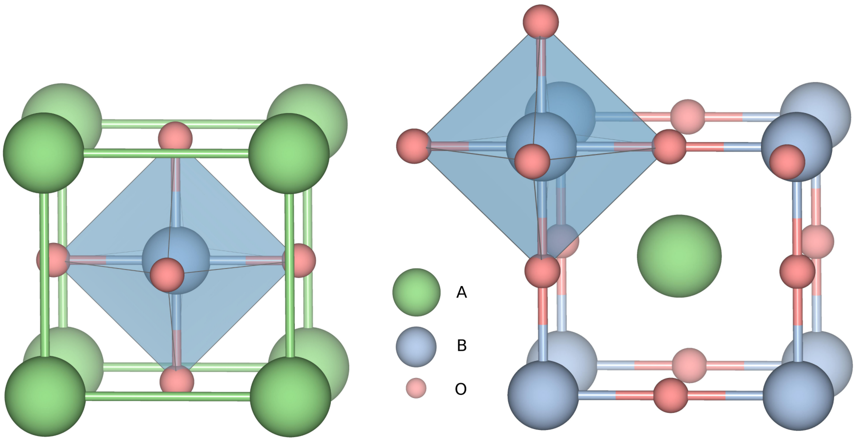

Figure A.1: The Cubic $Pm\bar{3}m$ (221) crystal symmetry for the perovskite. The conventional A-atom centred representation is shown to the left and the B-atom centred representation to the right. The inscribed oxygen octahedron is marked with blue.

Many lower symmetry perovskite structures, called *hettptypes*, can be related to the aristotype as either a rigid rotation of the inscribed oxygen octahedron, called tilt or Glazer rotation, or as a displacement of the body centreed B atom. The tilted structures can be described in terms of six order parameters ϕ_i, where ϕ_1 to ϕ_3 denote the rotation angle about the three cartesian axes with rotation in successive layers in the same direction and ϕ_4 to ϕ_6 in opposite direction in successive layers. The R_{25}-mode instability, which implies octahedral rotation in opposite direction along the axis of rotation, can lead to symmetries $(0,0,0,1,0,0)$ (tetragonal $I4/mcm$), $(0,0,0,1,1,0)$ (orthorombic $Imma$), $(0,0,0,1,1,1)$ (rombohedral $R\bar{3}c$) and linear combinations of these. An M-point instability leads to structures described by the first three order parameters ϕ_1 to ϕ_3. Similarly, the three ferroelectric phases of $BaTiO_3$ can be described by three order parameters describing the displacement of the Ti atom in the directions [100] (tetragonal $Pmma$), [110] (orthorombic $Amm2$) and [111] (rombohedral $R3c$).

The lower symmetry structures are generally described by unit cell vectors which do not coincide with the original cubic lattice vectors. In these cases the vector equivalent to the unitcell vectors for the cubic symmetry (essentially the distance between nearest neighbour A (or B) atoms in three (almost) orthogonal directions) are referred to as *pseudo cubic* lattice vector $\tilde{a}$. These are often of different lengths in different directions. The pseudo cubic lattice constant can then be defined as $\tilde{a} = (abc)^{1/3} \approx V_{\text{pseudo cubic}}^{1/3}$. The approximation becomes an equality if the three directions are truly orthogonal and of equal length.

Below follows an overview of three different crystal structures likely to form as a consequence of an R-point instability. In addition, the three different ferroelectric phases exhibited by $BaTiO_3$ are described.

A.2 Tetragonal $I4/mcm$ (140)

The anti-ferroelectric distortion in $SrTiO_3$, which is also the conjectured phase of pressurised BZO, causes a lowering of the symmetry to a tetragonal phase. This phase can be described as a Glazer rotation $a^0a^0c^-$, i.e. a rigid rotation of the oxygen octahedra around the z-axis in a cog-wheel fashion, with the rotation of neighbouring layers along the z-axis in opposite direction. This structure is illustrated in a 40 atom supercell in Fig. A.2a. The conventional unit cell is related to the original cubic through the transformation $a' = [1, 1, 0]$, $b' = [1, -1, 0]$ and $c' = [0, 0, 2]$, with the lengths of the new lattice vectors $a' = b' \neq c'$ with $a'/np.sqrt2 < a = 2c'$. The conventional unit cell contains 20 atoms. The primitive unit cell, which is preferred for computational purposes but less intuitive, contains only 10 atoms. The Shoenflies notation D_{4h} indicates a dihedral symmetry with 4-fold rotational symmetry around the principal axis, the z-axis, together with a horrisontal mirror plane.

A.3 Orthorhombic $Imma$ (74)

The orthorhombic $Imma$ (74), visualised in figure A.2b, is related to the original cubic through the transformation $a' = [1, 1, 0]$, $b' = [1, -1, 0]$ and $c' = [0, 0, 2]$, with the lengths of the new lattice vectors $a' = b' \neq c'$ with $c' < 2a$, in combination with the Glazer tilt $a^0b^-b^-$, i.e. equal octahedral rotations around two axes. In the orthorhombic setting one zirconium atom is located in (0,0,0) and one is base centred with a repetition at $c'/2$ but with the octahedral tilt in the opposite direction. The conventional unit cell thus contains 20 atoms, but for computational purposes a primitive unit cell containing only 10 atoms in attainable. The Shoenflies notation D_{2h}.

A.4 Rhombohedral $R\bar{3}c$ (167)

The rhombohedral $R\bar{3}c$ (167) is obtained from the cubic perovskite structure through equal octahedral rotations around all three cartesian axes. This can be denoted in a Glazer rotation as $a^-a^-a^-$. In other words this is a rotation around the [1,1,1]-direction with consecutive layers in opposite order. Figure A.2c shows the primitive unit cell of this structure along the 3-fold principal axis. There is the rhombohedral rendering.

The new lattice vectors a', b', and c' are obtained from the pseudo-cubic lattice vectors a, b, and c through the relation $a' = [1, 0, 1]$, $b' = [1, 0, -1]$ and $c' = [1, 1, 1]$. Although a pure Glazer rotation would leave all $\alpha = 90°$, this is not a requirement. In order for these new vectors to span, not a cubic but a rhombohedral cell the cell also needs to be augmented along the c'-direction, causing the $\alpha \neq 90°$. However, all pseudo-cubic angles α as well as pseudo-cubic lattice constants a are still equal in magnitude.

A.5 Tetragonal $Pmma$ (99)

The Tetragonal $Pmma$ (99) structure is a FE displacement through [100]. This is the ferroelectric phase assumed by $BaTiO_3$ at room temperature. The unit cell remains the same with octahedral unit vectors, but of equal length with one $c > a = b$.

A.6 Orthorombic $Amm2$ (38)

The orthorhombic $Amm2$ structure, visualised in figure A.2e, is essentially obtained from a rotation of the basis vectors b^* and c^* around the a-axis to [0,1,1] and [0,1,-1] with a remaining [100]. In addition the length of the vectors is changed such that the basis square becomes rectangular $b \neq c$ with an approximate length of $\sqrt{2}$a. The Shoenflies notation C_{2v} reveals that the c axis can also be viewed as a two-fold rotation with two vertical mirror planes, containing one of the two other cartesian axes. The cell now contains an base centred atom on the A face, i.e. in the plane perpendicular to the a axis. The a and b axes contain horizontal mirror planes (both planes include the c-axis) while the third direction (011) only has 2-fold rotational symmetry. This is because the Ba-atom is slightly displaced in the c-direction (The b and c axes are similar from a point group perspective.)

A.7 Rombohedral $R3c$ (160)

The rhombohedral $R3c$ (160) structure is a FE displacement through [111]. Similar to the rhombohedral structure No. 167, the new lattice vectors a', b', and c' are obtained from the pseudo-cubic lattice vectors a, b, and c through the relation $a' = [1, 0, 1]$, $b' = [1, 0, -1]$ and $c' = [1, 1, 1]$.

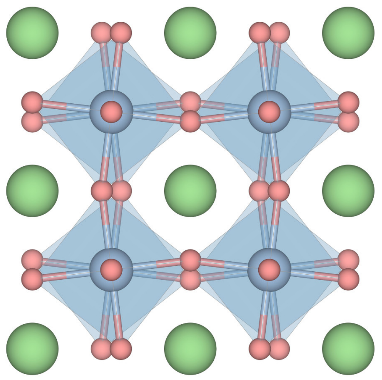

(a) The Tetragonal $I4/mcm$ (140) perovskite crystal symmetry.

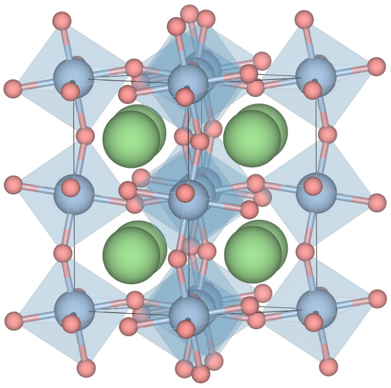

(b) The Orthorhombic $Imma$ (74) crystal symmetry in the orthorhombic visualisation.

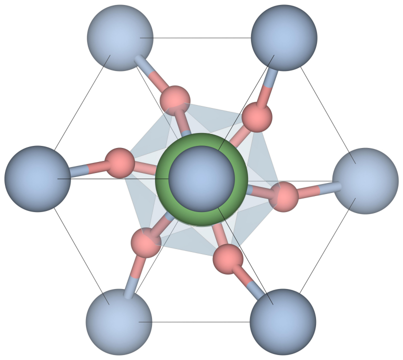

(c) The Rhombohedral $R\bar{3}c$ (167) crystal symmetry in the rhombohedral visualisation.

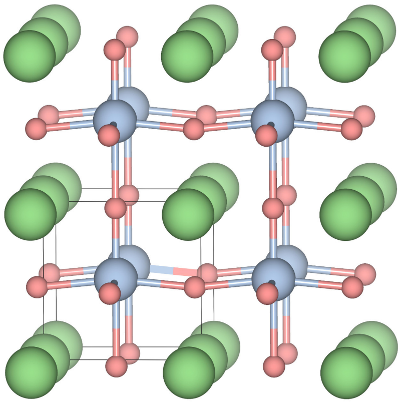

(d) The Tetragonal $P4mm$ (99) crystal symmetry.

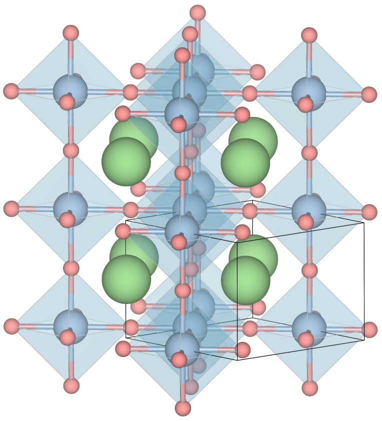

(e) The Orthorhombic $Amm2$ (38) crystal symmetry in the orthorhombic visualisation.

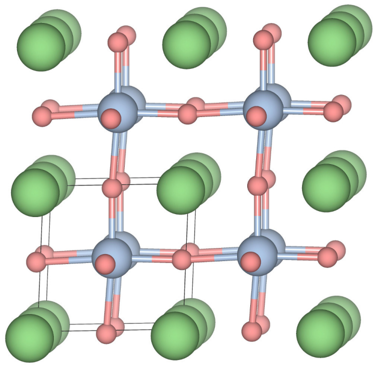

(f) The Rhombohedral $R3m$ (160) crystal symmetry in the pseudocubic visualisation.

Space group	$Pm\bar{3}m$	$I4/mcm$	$Imma$	$R\bar{3}c$	$Pmma$
Crystal system	*Cubic*	*Tetr.*	*Orth.*	*Rhomb.*	*Tetr.*
No.	221	140	74	167	99
Schönflies	O_h^1	D_{4h}^{18}	D_{2h}^{24}	D_{3d}^{6}	C_{4v}^{1}
Glazer*	$a^0a^0a^0$	$a^0a^0c^-$	$a^0b^-b^-$	$a^-a^-a^-$	100
a	$a = b = c$	$a = b \neq c$	$a = b \neq c$	$a = b \neq c$	$a = b \neq c$
α	90	90	90	90	90
β	90	90	90	90	90
γ	90	90	90	120	90
O1	$3c$	$4a$	$8g$	$18e$	$2c$
O2	–	$8h$	$4e$	–	$1a$
Ba	$1a$	$4b$	$4e$	$6a$	$1b$
Zr	$1b$	$4c$	$4a$	$6b$	$1a$

[*] Where the Glazer rotation is not applicable the B-cation displacement direction has instea

The irreducible representations using group theoretical methods

The following section is a short outline of the determination of the irreducible representations (irreps) for the special k-points on the Brillouin zone boundary where $R_\alpha^{-1}\mathbf{k} = \mathbf{k} + \mathbf{K}_m$. Here R_α is a symmetry operation, $\mathbf{k}$ the k-point in the Brillouin zone and $\mathbf{K}_m$ a reciprocal lattice vector. As a specific example irreps at the R-point is determined, following the prescription in Ref. 206.

The characters (χ) for the equivalence transformation are give by

$$\chi^{\mathrm{eq}} = \sum_j \delta_{R_\alpha \mathbf{r}_j, \mathbf{r}_j} e^{\mathrm{i}\mathbf{K}_m \cdot \mathbf{r}_j} \tag{B.1}$$

where $\mathbf{r}_j$ is the position of the jth atom with respect to the origin of the point group and $\delta_{R_\alpha \mathbf{r}_j, \mathbf{r}_j} = 1$ if $R_\alpha \mathbf{r}_j$ and $\mathbf{r}_j$ refer to equivalent atomic positions ($R_\alpha \mathbf{r}_j = \mathbf{r}_j + R_n$ where R_n is a lattice vector). Application of Eq. (B.1) becomes simple for the Γ-point irreps. Here χ^{eq} equals the number of atoms which remain on the same site after a given symmetry transformation R_α. For other high symmetry points some terms come with a negative sign due to the exponential factor .

By letting the A atom be at the centre of the point group, $\mathbf{r}_\mathrm{A} = (0,0,0)$, $\mathbf{r}_\mathrm{B} = (1/2,1/2,1/2)$ while for the oxygen $\mathbf{r}_{\mathrm{O}_1} = (0,1/2,1/2)$, $\mathbf{r}_{\mathrm{O}_2} = (1/2,0,1/2)$ and $\mathbf{r}_{\mathrm{O}_3} = (1/2,1/2,0)$. The characters for the equivalence transformations at the R-point are found at the top of table B.1. The rest of table B.1 contains the character table for the O_h group to be used in combination with the decomposition formula below.

The equivalence transformations are identified as:

$$\begin{aligned} R_{\mathrm{A}}^{\mathrm{eq}} &= R_1 \\ R_{\mathrm{B}}^{\mathrm{eq}} &= R_2' \\ R_{\mathrm{O_3}}^{\mathrm{eq}} &= R_{25} \\ R_{\mathrm{vec}} &= R_{15} \end{aligned} \tag{B.2}$$

The lattice modes is computed as

$$\begin{aligned} R_{\mathrm{lat.mod.}} &= R^{\mathrm{eq}} \otimes R_{\mathrm{vec}} \\ &= (R_1 + R_2' + R_{25}) \otimes R_{15} \\ &= R_1 \otimes R_{15} + R_2' \otimes R_{15} + R_{25} \otimes R_{15} \\ &= R_{15} + R_{25}' + (R_2' + R_{12}' + R_{15} + R_{25}) \\ &= R_2' + R_{12}' + 2R_{15} + R_{25}' + R_{25} \end{aligned} \tag{B.3}$$

Here the characters for the direct product $\otimes$, taken between two representations of the same group R, are computed through

$$\chi^{(l_1 \otimes l_2)}(R) = \chi^{(l_1)}(R)\chi^{(l_2)}(R) \tag{B.4}$$

where χ is the character for the symmetry element R and l_i is representation of the group. If the direct product is again a reducible representation

$$\chi^{(\mathrm{reducible})}(\mathcal{C}_k) = \sum_{\Gamma_j} a_j \chi^{(\Gamma_j)}(\mathcal{C}_k) \tag{B.5}$$

it can be reduced through the decomposition formula

$$a_j = \frac{1}{h} \sum_k N_k \chi^{(\Gamma_j)}(\mathcal{C}_k)^* \chi^{(\mathrm{reducible})}(\mathcal{C}_k) \tag{B.6}$$

where N is the number of elements in the class $\mathcal{C}_k$ and h is order of the group.

Until the fourth line in Equation (B.3) the terms have been ordered atomwise in such a way that A is the first term, B is the second and O are the remaining. This makes it immediately clear that R_{15} is an A-atom mode and R_{25}' is a B-atom mode. From the character table B.1 we can read off the type of the R_{25} mode as triply degenerate and odd with respect to the origin of the point group, the A atom. It is also odd with respect to the C_4 symmetry operation which uniquely identifies the R_{25} as the anti-ferrodistortive mode in a $\mathrm{ABO_3}$.

This designation is not unique and in some texts the R_{25}-mode is denoted R_{15}'. There is no contradiction in this, however, since the decomposition if irreps depend on the choice of point group origin. Howard and Stoke [9–11] have defined the point group origin on the B site (in which the oxygen atoms are located on the d Wyckoff site) whereas the choice of the A atom as he point group origin leads to the results in this thesis.

Table B.1: The equivalence transformations at the R-point for the constituent atoms in BaZrO$_3$ (top) and the character table for the O_h point group.

	E	$3C_4^2$	$6C_4$	$6C_2'$	$8C_3$	i	$3iC_4^2$	$6iC_4$	$6iC_2'$	$8iC_3$
$R_{\mathrm{A}}^{\mathrm{eq}}$	1	1	1	1	1	1	1	1	1	1
$R_{\mathrm{B}}^{\mathrm{eq}}$	1	1	−1	−1	1	−1	−1	1	1	−1
$R_{\mathrm{O_3}}^{\mathrm{eq}}$	3	−1	−1	1	0	3	−1	−1	1	0
R_1	1	1	1	1	1	1	1	1	1	1
R_2	1	1	−1	−1	1	1	1	−1	−1	1
R_{12}	2	2	0	0	−1	2	2	0	0	−1
R_{15}	3	−1	1	−1	0	−3	1	−1	1	0
R_{25}	3	−1	−1	1	0	−3	1	1	−1	0
R_1'	1	1	1	1	1	−1	−1	−1	−1	−1
R_2'	1	1	−1	−1	1	−1	−1	1	1	−1
R_{12}'	2	2	0	0	−1	−2	−2	0	0	1
R_{15}'	3	−1	1	−1	0	3	−1	1	−1	0
R_{25}'	3	−1	−1	1	0	3	−1	−1	1	0

Table B.2: Phonon frequencies in meV for BaZrO$_3$ at the high symmetry points computed using CX0p.

Γ_{15}	0	R_{25}	6.00	X_5'	10.99	M_1'	10.87
Γ_{15}	14.59	R_{15}	13.20	X_5	15.62	M_5'	11.11
Γ_{15}	25.88	R_{25}'	38.43	X_3'	16.95	M_2	12.11
Γ_{25}	26.02	R_{15}	46.26	X_5	27.28	M_2'	18.30
Γ_{15}	63.18	R_{12}'	67.57	X_1	28.10	M_5'	26.68
		R_2'	101.04	X_2	30.35	M_5	35.49
				X_5'	33.82	M_5'	44.00
				X_1	55.08	M_1'	51.45
				X_5	61.48	M_2'	59.33
				X_4'	90.73	M_1'	68.72
						M_3	97.23

Acknowledgments

There are some people without whom this thesis could not have been written. Among these are my supervisors Per Hyldgaard and Göran Wahnström and co-supervisor Paul Erhart as well as my colleague Anders Lindman who has co-authored three of the appended papers. I would also like to thank my collaborators Maths Karlsson, Carin Österberg, Laura Mazzei and Adrien Perrichon who have contributed with experimental expertise and my research group at Materials and Surface Theory.

I would also like to thank the Swedish Energy Agency (Energimyndigheten) and the Swedish Foundation for Strategic Research (Stiftelsen for strategisk forskning) for financing and Swedish National Infrastructure for Computing (SNIC) for providing computational resources.

In addition I would like to thank people who have contributed with moral support throughout this work; Adam Arvidsson and Emil Ljungskog for all fruitful lunch discussions, my parents for all encouragement and my friends both at Chalmers and outside.

Finally I would like to thank my wife, Sofia, and my son, Alfred, for being my source of inspiration in life.

Bibliography

[1] R. H. Mitchell, *Perovskites: Modern and Ancient* (Almaz Press Thunder Bay, Thunder Bay, Ontario, Canada, 2002).

[2] R. J. Tilley, *Perovskites: structure-property relationships* (John Wiley & Sons, Chichester, United Kingdom, 2016).

[3] A. S. Bhalla, R. Guo, and R. Roy, *The perovskite structure - a review of its role in ceramic science and technology*, Mater. Res. Innov. **4**, 3 (2000).

[4] V. M. Goldschmidt, *Die Gesetze der Krystallochemie*, Naturwissenschaften **14**, 477 (1926).

[5] A. M. Glazer, *The classification of tilted octahedra in perovskites*, Acta Crystallogr. Sect. B Struct. Crystallogr. Cryst. Chem. **28**, 3384 (1972).

[6] A. M. Glazer, *Simple ways of determining perovskite structures*, Acta Crystallogr. Sect. A **31**, 756 (1975).

[7] P. M. Woodward and IUCr, *Octahedral Tilting in Perovskites. I. Geometrical Considerations*, Acta Crystallogr. Sect. B Struct. Sci. **53**, 32 (1997).

[8] P. M. Woodward and IUCr, *Octahedral Tilting in Perovskites. II. Structure Stabilizing Forces*, Acta Crystallogr. Sect. B Struct. Sci. **53**, 44 (1997).

[9] C. J. Howard and H. T. Stokes, *Group-Theoretical Analysis of Octahedral Tilting in Perovskites*, Acta Crystallogr. Sect. B Struct. Sci. **54**, 782 (1998).

[10] C. J. Howard, H. T. Stokes, and IUCr, *Octahedral tilting in cation-ordered perovskites – a group-theoretical analysis*, Acta Crystallogr. Sect. B Struct. Sci. **60**, 674 (2004).

[11] C. J. Howard, H. T. Stokes, and IUCr, *Structures and phase transitions in perovskites – a group-theoretical approach*, Acta Crystallogr. Sect. A Found. Crystallogr. **61**, 93 (2005).

[12] A. R. Akbarzadeh, I. Kornev, C. Malibert, L. Bellaiche, and J. M. Kiat, *Combined theoretical and experimental study of the low-temperature properties of* $BaZrO_3$, Phys. Rev. B **72**, 205104 (2005).

[13] S. Yamanaka, T. Hamaguchi, T. Oyama, T. Matsuda, S.-i. Kobayashi, and K. Kurosaki, *Heat capacities and thermal conductivities of perovskite type* $BaZrO_3$ *and BaCeO3*, J. Alloys Compd. **359**, 1 (2003).

[14] N. K. Karan, R. S. Katiyar, T. Maiti, R. Guo, and A. S. Bhalla, *Raman spectral studies of* Zr^{4+} *-rich* $BaZr_xTi_{1-x}O_3$ *(*$0.5 \leq x \leq 1.00$*) phase diagram*, J. Raman Spectrosc. **40**, 370 (2009).

[15] Y. Zhao and D. Weidner, *Thermal expansion of* $SrZrO_3$ *and* $BaZrO_3$ *perovskites*, Phys. Chem. Miner. **18**, 294 (1991).

[16] P. S. Dobal, A. Dixit, R. S. Katiyar, Z. Yu, R. Guo, and A. S. Bhalla, *Micro-Raman scattering and dielectric investigations of phase transition behavior in the* $BaTiO_3$*–*$BaZrO_3$ *system*, J. Appl. Phys. **89**, 8085 (2001).

[17] X. Yang, Q. Li, R. Liu, B. Liu, H. Zhang, S. Jiang, J. Liu, B. Zou, T. Cui, and B. Liu, *Structural phase transition of* $BaZrO_3$ *under high pressure*, J. Appl. Phys. **115**, 124907 (2014).

[18] A. I. Lebedev and I. A. Sluchinskaya, *Structural instability in* $BaZrO_3$ *crystals: Calculations and experiment*, Phys. Solid State **55**, 1941 (2013).

[19] J. W. Bennett, I. Grinberg, and A. M. Rappe, *Effect of symmetry lowering on the dielectric response of* $BaZrO_3$, Phys. Rev. B **73**, 180102 (2006).

[20] A. Bilić and J. D. Gale, *Ground state structure of* $BaZrO_3$ *: A comparative first-principles study*, Phys. Rev. B **79**, 174107 (2009).

[21] R. Kagimura, M. Suewattana, and D. J. Singh, *(Ba,K,La)*ZrO_3 *as a possible lead-free ferroelectric: Density functional calculations*, Phys. Rev. B **78**, 012103 (2008).

[22] W. Zhong and D. Vanderbilt, *Competing structural instabilities in cubic perovskites*, Phys. Rev. Lett. **74**, 2587 (1995).

[23] W. Zhong and D. Vanderbilt, *Effect of quantum fluctuations on structural phase transitions in* $SrTiO_3$ *and* $BaTiO_3$, Phys. Rev. B **53**, 5047 (1996).

[24] M. A. Helal, T. Mori, and S. Kojima, *Softening of infrared-active mode of perovskite* $BaZrO_3$ *proved by terahertz time-domain spectroscopy*, Appl. Phys. Lett. **106**, 182904 (2015).

[25] M. A. Helal, T. Mori, and S. Kojima, *Terahertz time-domain spectroscopy and Raman scattering studies of incipient ferroelectric* $BaZrO_3$, Ferroelectrics **499**, 107 (2016).

[26] Y. Kobayashi, O. J. Hernandez, T. Sakaguchi, T. Yajima, T. Roisnel, Y. Tsujimoto, M. Morita, Y. Noda, Y. Mogami, A. Kitada, M. Ohkura, S. Hosokawa, Z. Li, K. Hayashi, Y. Kusano, J. eun Kim, N. Tsuji, A. Fujiwara, Y. Matsushita, K. Yoshimura, K. Takegoshi, M. Inoue, M. Takano, and H. Kageyama, *An oxyhydride of* $BaTiO_3$ *exhibiting hydride exchange and electronic conductivity.*, Nat. Mater. **11**, 507 (2012).

[27] Y. Iwazaki, T. Suzuki, and S. Tsuneyuki, *Negatively charged hydrogen at oxygen-vacancy sites in* $BaTiO_3$*: Density-functional calculation*, J. Appl. Phys. **108**, 1 (2010).

[28] G. Bouilly, T. Yajima, T. Terashima, W. Yoshimune, K. Nakano, C. Tassel, Y. Kususe, K. Fujita, K. Tanaka, T. Yamamoto, Y. Kobayashi, and H. Kageyama, *Electrical Properties of Epitaxial Thin Films of Oxyhydrides* $ATiO_{3-x}H_x$ *(A = Ba and Sr)*, Chem. Mater. **27**, 6354 (2015).

[29] X. Liu, T. S. Bjorheim, and R. Haugsrud, *Formation and migration of hydride ions in* $BaTiO_{3-x}H_x$ *oxyhydride*, J. Mater. Chem. A **5**, 1050 (2017).

[30] P. Erhart, A. Klein, D. Åberg, and B. Sadigh, *Efficacy of the DFT + U formalism for modeling hole polarons in perovskite oxides efficacy of the DFT + U formalism for Erhart, Klein, Åberg, and Sadigh*, Phys. Rev. B **90**, 1 (2014).

[31] A. Lindman, P. Erhart, and G. Wahnström, *Implications of the band gap problem on oxidation and hydration in acceptor-doped barium zirconate*, Phys. Rev. B **91**, 245114 (2015).

[32] A. Lindman, P. Erhart, and G. Wahnström, *Polaronic contributions to oxidation and hole conductivity in acceptor-doped* $BaZrO_3$, Phys. Rev. B **94**, 075204 (2016).

[33] P. Hohenberg and W. Kohn, *Inhomogeneous Electron Gas*, Phys. Rev. **136**, B864 (1964).

[34] W. Kohn and L. J. Sham, *Self-Consistent Equations Including Exchange and Correlation Effects*, Phys. Rev. **140**, A1133 (1965).

[35] K. Burke, *Perspective on density functional theory*, J. Chem. Physics **136**, 150901 (2012).

[36] R. O. Jones, *Density functional theory: Its origins, rise to prominence, and future*, Rev. Mod. Phys. **87**, 897 (2015).

[37] W. Kohn, *Nobel Lecture: Electronic structure of matter—wave functions and density functionals*, Rev. Mod. Phys. **71**, 1253 (1999).

[38] R. O. Jones and O. Gunnarsson, *The density functional formalism, its applications and prospects*, Rev. Mod. Phys. **61**, 689 (1989).

[39] M. Dion, H. Rydberg, E. Schröder, D. C. Langreth, and B. I. Lundqvist, *Van der Waals Density Functional for General Geometries*, Phys. Rev. Lett. **92**, 246401 (2004).

[40] P. M. Gill, *Essay: Obituary: Density Functional Theory (1927-1993)*, Aust. J. Chem. **54**, 661 (2001).

[41] S. Kümmel and L. Kronik, *Orbital-dependent density functionals: Theory and applications*, Rev. Mod. Phys. **80**, 3 (2008).

[42] A. D. Becke, *A new mixing of Hartree–Fock and local density-functional theories*, J. Chem. Phys. **98**, 1372 (1993).

[43] A. D. Becke, *Density-functional thermochemistry. III. The role of exact exchange*, J. Chem. Phys. **98**, 5648 (1993).

[44] A. D. Becke, *Perspective: Fifty years of density-functional theory in chemical physics*, J. Chem. Phys. **140**, 18A301 (2014).

[45] J. P. Perdew, M. Ernzerhof, and K. Burke, *Rationale for mixing exact exchange with density functional approximations*, J. Chem. Phys. **105**, 9982 (1996).

[46] C. Adamo and V. Barone, *Toward reliable density functional methods without adjustable parameters: The PBE0 model*, J. Chem. Phys. **110**, 6158 (1999).

[47] J. Heyd, G. E. Scuseria, and M. Ernzerhof, *Hybrid functionals based on a screened Coulomb potential*, J. Chem. Phys. **118**, 8207 (2003).

[48] J. Heyd, G. E. Scuseria, and M. Ernzerhof, *Erratum: "Hybrid functionals based on a screened Coulomb potential" [J. Chem. Phys. 118, 8207 (2003)]*, J. Chem. Phys. **124**, 219906 (2006).

[49] K. Berland, Y. Jiao, J.-H. Lee, T. Rangel, J. B. Neaton, and P. Hyldgaard, *Assessment of two hybrid van der Waals density functionals for covalent and non-covalent binding of molecules*, J. Chem. Phys. **146**, 234106 (2017).

[50] Y. Jiao, E. Schröder, and P. Hyldgaard, *Extent of Fock-exchange mixing for a hybrid van der Waals density functional?*, J. Chem. Phys. **148**, 194115 (2018).

[51] O. Gunnarsson and B. I. Lundqvist, *Exchange and correlation in atoms, molecules, and solids by the spin-density-functional formalism*, Phys. Rev. B **13**, 4274 (1976).

[52] D. C. Langreth and J. P. Perdew, *Exchange-correlation energy of a metallic surface: Wave-vector analysis*, Phys. Rev. B **15**, 2884 (1977).

[53] M. Levy and J. P. Perdew, *Hellmann-Feynman, virial, and scaling requisites for the exact universal density functionals. Shape of the correlation potential and diamagnetic susceptibility for atoms*, Phys. Rev. A **32**, 2010 (1985).

[54] M. Levy, *Density-functional exchange correlation through coordinate scaling in adiabatic connection and correlation hole*, Phys. Rev. A **43**, 4637 (1991).

[55] J. P. Perdew and A. Zunger, *Self-interaction correction to density-functional approximations for many-electron systems*, Phys. Rev. B **23**, 5048 (1981).

[56] J. P. Perdew, R. G. Parr, M. Levy, and J. L. Balduz, *Density-Functional Theory for Fractional Particle Number: Derivative Discontinuities of the Energy*, Phys. Rev. Lett. **49**, 1691 (1982).

[57] M. Ernzerhof and G. E. Scuseria, *Assessment of the Perdew–Burke–Ernzerhof exchange-correlation functional*, J. Chem. Phys. **110**, 5029 (1999).

[58] Y. Zhang and W. Yang, *Comment on "Generalized Gradient Approximation Made Simple"*, Phys. Rev. Lett. **80**, 890 (1998).

[59] J. P. Perdew and Y. Wang, *Accurate and simple density functional for the electronic exchange energy: Generalized gradient approximation*, Phys. Rev. B **33**, 8800 (1986).

[60] J. P. Perdew, A. Ruzsinszky, J. Tao, V. N. Staroverov, G. E. Scuseria, and G. I. Csonka, *Prescription for the design and selection of density functional approximations: More constraint satisfaction with fewer fits*, J. Chem. Phys. **123**, 062201 (2005).

[61] J. P. Perdew, A. Ruzsinszky, G. I. Csonka, O. A. Vydrov, G. E. Scuseria, L. A. Constantin, X. Zhou, and K. Burke, *Restoring the Density-Gradient Expansion for Exchange in Solids and Surfaces*, Phys. Rev. Lett. **100**, 136406 (2008).

[62] K. Berland, C. A. Arter, V. R. Cooper, K. Lee, B. I. Lundqvist, E. Schröder, T. Thonhauser, and P. Hyldgaard, *van der Waals density functionals built upon the electron-gas tradition: Facing the challenge of competing interactions*, J. Chem. Phys. **140**, 18A539 (2014).

[63] K. Berland and P. Hyldgaard, *Exchange functional that tests the robustness of the plasmon description of the van der Waals density functional*, Phys. Rev. B **89**, 035412 (2014).

[64] M. G. Medvedev, I. S. Bushmarinov, J. Sun, J. P. Perdew, and K. A. Lyssenko, *Density functional theory is straying from the path toward the exact functional*, Science (80-.). **355**, 49 (2017).

[65] E. Kraisler and L. Kronik, *Fundamental gaps with approximate density functionals: The derivative discontinuity revealed from ensemble considerations*, J. Chem. Phys. **140**, 18A540 (2014).

[66] E. Kraisler and L. Kronik, *Piecewise Linearity of Approximate Density Functionals Revisited: Implications for Frontier Orbital Energies*, Phys. Rev. Lett. **110**, 126403 (2013).

[67] C. Freysoldt, B. Grabowski, T. Hickel, J. Neugebauer, G. Kresse, A. Janotti, and C. G. Van de Walle, *First-principles calculations for point defects in solids*, Rev. Mod. Phys. **86**, 253 (2014).

[68] V. I. Anisimov, J. Zaanen, and O. K. Andersen, *Band theory and Mott insulators: Hubbard U instead of Stoner I*, Phys. Rev. B **44**, 943 (1991).

[69] S. L. Dudarev, G. A. Botton, S. Y. Savrasov, C. J. Humphreys, and A. P. Sutton, *Electron-energy-loss spectra and the structural stability of nickel oxide: An LSDA+U study*, Phys. Rev. B **57**, 1505 (1998).

[70] G. Rose, *Mineralogisch-geognostische Reise nach dem Ural, dem Altai and dem Kaspische Meere, Zweiter Band* (Verlag der Sanderschen Buchhandlung (G. E. Reimer), Berlin, 1842).

[71] E. Wainer, *High Titania Dielectrics*, Trans. Electrochem. Soc. **89**, 331 (1946).

[72] M. E. Lines and A. M. Glass, *Principles and applications of ferroelectrics and related materials* (Oxford University Press, Oxford, Great Britain, 1977).

[73] B. Jaffe, W. R. Cook, and H. Jaffe, *Piezoelectric ceramics* (Academic Press, Berkeley Square House, Berkeley Square, London, 1971).

[74] R. von Helmolt, J. Wecker, B. Holzapfel, L. Schultz, and K. Samwer, *Giant negative magnetoresistance in perovskitelike* $La_{2/3}Ba_{1/3}MnO_x$ *ferromagnetic films*, Phys. Rev. Lett. **71**, 2331 (1993).

[75] Y. Moritomo, A. Asamitsu, H. Kuwahara, and Y. Tokura, *Giant magnetoresistance of manganese oxides with a layered perovskite structure*, Nature **380**, 141 (1996).

[76] T. Okuda, K. Nakanishi, S. Miyasaka, and Y. Tokura, *Large thermoelectric response of metallic perovskites:* $Sr_{1-x}La_xTiO_3$ *(*$0 < x < 0.1$*)*, Phys. Rev. B **63**, 113104 (2001).

[77] J. F. Schooley, W. R. Hosler, E. Ambler, J. H. Becker, M. L. Cohen, and C. S. Koonce, *Dependence of the Superconducting Transition Temperature on Carrier Concentration in Semiconducting SrTi O 3*, Phys. Rev. Lett. **14**, 305 (1965).

[78] D. Johnston, H. Prakash, W. Zachariasen, and R. Viswanathan, *High temperature superconductivity in the Li Ti O ternary system*, Mater. Res. Bull. **8**, 777 (1973).

[79] K. Funke, *Solid State Ionics: from Michael Faraday to green energy—the European dimension*, Sci. Technol. Adv. Mater. **14**, 043502 (2013).

[80] K. Kreuer, *Proton-Conducting Oxides*, Annu. Rev. Mater. Res. **33**, 333 (2003).

[81] A. Wells, *Structural Inorganic Chemistry (fifth edition)* (Oxford University Press, Oxford, Great Britain, 1987).

[82] R. D. Shannon and IUCr, *Revised effective ionic radii and systematic studies of interatomic distances in halides and chalcogenides*, Acta Crystallogr. Sect. A **32**, 751 (1976).

[83] L. A. Reznichenko, L. A. Shilkina, S. V. Titov, O. N. Razumovskaya, V. V. Titov, and S. I. Shevtsov, *Defect Structure of Alkaline-Earth, Cadmium, and Lead Titanates*, Inorg. Mater. **41**, 492 (2005).

[84] K. A. Mller and W. Berlinger, *Static critical exponents at structural phase Transitions*, Phys. Rev. Lett. **26**, 13 (1971).

[85] J. C. Slater, *The Lorentz Correction in Barium Titanate*, Phys. Rev. **78**, 748 (1950).

[86] N. A. Benedek and C. J. Fennie, *Why Are There So Few Perovskite Ferroelectrics?*, J. Phys. Chem. C **117**, 13339 (2013).

[87] F. Giannici, M. Shirpour, A. Longo, A. Martorana, R. Merkle, and J. Maier, *Long-Range and Short-Range Structure of Proton-Conducting Y:BaZrO*$_3$, Chem. Mater. **23**, 2994 (2011).

[88] C. Chemarin, N. Rosman, T. Pagnier, and G. Lucazeau, *A High-Pressure Raman Study of Mixed Perovskites* $BaCe_xZr_{1-x}O_3$ *(*$0 \leq x \leq 1$*)*, J. Solid State Chem. **149**, 298 (2000).

[89] C. Toulouse, D. Amoroso, C. Xin, P. Veber, M. C. Hatnean, G. Balakrishnan, M. Maglione, P. Ghosez, J. Kreisel, and M. Guennou, *Lattice dynamics and Raman spectrum of BaZrO*$_3$ *single crystals*, Phys. Rev. B **100**, 134102 (2019).

[90] J. J. Hren, J. I. Goldstein, and D. C. Joy, *Introduction to Analytical Electron Microscopy* (Springer-Verlag, Boston, MA, 1990), p. 305.

[91] C. Grotthuß, *Sur la décomposition de l'eau et des corps qu'elle tient en dissolution à l'aide de l'électricité galvanique*, Ann. Chim. **58**, 54 (1806).

[92] S. B. Adler, *Chemical Expansivity of Electrochemical Ceramics*, J. Am. Ceram. Soc. **84**, 2117 (2001).

[93] A. K. E. Andersson, S. M. Selbach, C. S. Knee, and T. Grande, *Chemical Expansion Due to Hydration of Proton-Conducting Perovskite Oxide Ceramics*, J. Am. Ceram. Soc. **97**, 2654 (2014).

[94] F. G. Kinyanjui, S. T. Norberg, I. Ahmed, S. G. Eriksson, and S. Hull, *In-situ conductivity and hydration studies of proton conductors using neutron powder diffraction*, Solid State Ionics **225**, 312 (2012).

[95] C. Hiraiwa, D. Han, A. Kuramitsu, A. Kuwabara, H. Takeuchi, M. Majima, and T. Uda, *Chemical Expansion and Change in Lattice Constant of Y-Doped BaZrO*$_3$ *by Hydration/Dehydration Reaction and Final Heat-Treating Temperature*, J. Am. Ceram. Soc. **96**, 879 (2013).

[96] C. Chatzichristodoulou, P. Norby, P. V. Hendriksen, and M. B. Mogensen, *Size of oxide vacancies in fluorite and perovskite structured oxides*, J. Electroceramics **34**, 100 (2014).

[97] D. Marrocchelli, S. R. Bishop, H. L. Tuller, and B. Yildiz, *Understanding Chemical Expansion in Non-Stoichiometric Oxides: Ceria and Zirconia Case Studies*, Adv. Funct. Mater. **22**, 1958 (2012).

[98] D. Marrocchelli, S. R. Bishop, H. L. Tuller, G. W. Watson, B. Yildiz, P. A. Madden, P. A. Madden, G. W. Watson, and E. D. Wachsman, *Charge localization increases chemical expansion in cerium-based oxides*, Phys. Chem. Chem. Phys. **14**, 12070 (2012).

[99] S. R. Bishop, K. L. Duncan, and E. D. Wachsman, *Thermo-Chemical Expansion in Strontium-Doped Lanthanum Cobalt Iron Oxide*, J. Am. Ceram. Soc. **93**, 4115 (2010).

[100] S. A. Centoni, B. Sadigh, G. H. Gilmer, T. J. Lenosky, T. Díaz de la Rubia, and C. B. Musgrave, *First-principles calculation of intrinsic defect formation volumes in silicon*, Phys. Rev. B **72**, 195206 (2005).

[101] R. M. Helps, N. H. Rees, and M. A. Hayward, $Sr_3Co_2O_{4.33}H_{0.84}$ *: An Extended Transition Metal Oxide-Hydride*, Inorg. Chem. **49**, 11062 (2010).

[102] Y.-D. Chuang, A. D. Gromko, D. S. Dessau, T. Kimura, Y. Tokura, C. J. Kiely, S. J. Blundell, I. M. Marshall, and F. L. Pratt, *Fermi Surface Nesting and Nanoscale Fluctuating Charge/Orbital Ordering in Colossal Magnetoresistive Oxides*, Science (80-.). **292**, 1509 (2001).

[103] T. Sakaguchi, Y. Kobayashi, T. Yajima, M. Ohkura, C. Tassel, F. Takeiri, S. Mitsuoka, H. Ohkubo, T. Yamamoto, J. eun Kim, N. Tsuji, A. Fujihara, Y. Matsushita, J. Hester, M. Avdeev, K. Ohoyama, and H. Kageyama, *Oxyhydrides of (Ca,Sr,Ba)*TiO_3 *Perovskite Solid Solutions*, Inorg. Chem. **51**, 11371 (2012).

[104] L. Landau and S. Pekar, *Polaron effective mass*, Zh Eksp Teor Fiz **18**, 419 (1948).

[105] J. T. Devreese, *Polarons*, Encycl. Appl. Phys. **14**, 383 (2000).

[106] H. Fröhlich, *Electrons in lattice fields*, Adv. Phys. **3**, 325 (1954).

[107] R. P. Feynman, *Slow Electrons in a Polar Crystal*, Phys. Rev. **97**, 660 (1955).

[108] R. P. Feynman, R. W. Hellwarth, C. K. Iddings, and P. M. Platzman, *Mobility of Slow Electrons in a Polar Crystal*, Phys. Rev. **127**, 1004 (1962).

[109] N. A. Deskins and M. Dupuis, *Electron transport via polaron hopping in bulk* TiO_2*: A density functional theory characterization*, Phys. Rev. B **75**, 195212 (2007).

[110] A. Janotti, J. B. Varley, P. Rinke, N. Umezawa, G. Kresse, and C. G. Van de Walle, *Hybrid functional studies of the oxygen vacancy in* TiO_2, Phys. Rev. B **81**, 085212 (2010).

[111] A. Janotti, C. Franchini, J. B. Varley, G. Kresse, and C. G. Van de Walle, *Dual behavior of excess electrons in rutile* TiO_2, Phys. status solidi - Rapid Res. Lett. **7**, 199 (2013).

[112] M. Setvin, C. Franchini, X. Hao, M. Schmid, A. Janotti, M. Kaltak, C. Van de Walle, G. Kresse, and U. Diebold, *A direct view at excess electrons in* TiO_2 *rutile and anatase*, Phys. Rev. Lett. **113**, 086402 (2014).

[113] S. Yang, A. T. Brant, N. C. Giles, and L. E. Halliburton, *Intrinsic small polarons in rutile* TiO_2, Phys. Rev. B **87**, 125201 (2013).

[114] V. M. Khomenko, K. Langer, H. Rager, and A. Fett, *Electronic absorption by* Ti^{3+} *ions and electron delocalization in synthetic blue rutile*, Phys. Chem. Miner. **25**, 338 (1998).

[115] R. Scharfschwerdt, A. Mazur, O. F. Schirmer, H. Hesse, and S. Mendricks, *Oxygen vacancies in* $BaTiO_3$, Phys. Rev. B **54**, 15284 (1996).

[116] M. Schrader, D. Mienert, T.-S. Oh, H.-I. Yoo, and K. D. Becker, *An optical, EPR and electrical conductivity study of blue barium titanate,* $BaTiO_{3-\delta}$, Solid State Sci. **10**, 768 (2008).

[117] P. A. M. Dirac, *Quantum Mechanics of Many-Electron Systems*, Proc. R. Soc. A Math. Phys. Eng. Sci. **123**, 714 (1929).

[118] L. Kantorovich, *Quantum Theory of the Solid State: An Introduction* (Springer Netherlands, Dordrecht, 2004).

[119] E. Kaxiras, *Atomic end Electronic Structure of Solids* (Cambridge University Press, The Edinburgh Building, Cambridge, United Kingdom, 2003).

[120] N. Ashcroft and N. Mermin, *Solid state physics* (Brooks/Cole Cengage Learning, Belmont, Ca, USA, 1976).

[121] J. Thijssen, *Computational Physics* (Cambridge University Press, The Edinburgh Building, Cambridge, United Kingdom, 2007).

[122] R. Martin, *Electronic Structure* (Cambridge University Press, The Edinburgh Building, Cambridge, United Kingdom, 2008).

[123] L. H. Thomas, *The calculation of atomic fields*, Math. Proc. Cambridge Philos. Soc. **23**, 542 (1927).

[124] E. Fermi, *Un metodo statistico per la determinazione di alcune priorieta dell'atome*, Rend. Accad. Naz. Lincei **65**, 602 (1927).

[125] P. Dirac, *Note on exchange phenomena in the Thomas atom*, Math. Proc. Cambridge Philos. Soc. **26**, 376 (1930).

[126] J. P. Perdew, K. Burke, and M. Ernzerhof, *Generalized Gradient Approximation Made Simple*, Phys. Rev. Lett. **77**, 3865 (1996).

[127] L. Hedin and B. I. Lundqvist, *Explicit local exchange-correlation potentials*, J. Phys. C Solid State Phys. **4**, 2064 (1971).

[128] D. M. Ceperley and B. J. Alder, *Ground State of the Electron Gas by a Stochastic Method*, Phys. Rev. Lett. **45**, 566 (1980).

[129] J. P. Perdew and Y. Wang, *Accurate and simple analytic representation of the electron-gas correlation energy*, Phys. Rev. B **45**, 13244 (1992).

[130] Y. Andersson, D. C. Langreth, and B. I. Lundqvist, *van der Waals Interactions in Density-Functional Theory*, Phys. Rev. Lett. **76**, 102 (1996).

[131] K. Berland, V. R. Cooper, K. Lee, E. Schröder, T. Thonhauser, P. Hyldgaard, and B. I. Lundqvist, *van der Waals forces in density functional theory: a review of the vdW-DF method*, Reports Prog. Phys. **78**, 066501 (2015).

[132] T. Thonhauser, V. R. Cooper, S. Li, A. Puzder, P. Hyldgaard, and D. C. Langreth, *Van der Waals density functional: Self-consistent potential and the nature of the van der Waals bond*, Phys. Rev. B **76**, 125112 (2007).

[133] P. Hyldgaard, K. Berland, and E. Schröder, *Interpretation of van der Waals density functionals*, Phys. Rev. B **90**, 075148 (2014).

[134] Y. Jiao, E. Schröder, and P. Hyldgaard, *Signatures of van der Waals binding: A coupling-constant scaling analysis*, Phys. Rev. B **97**, 085115 (2018).

[135] A. Janotti, D. Segev, and C. G. Van de Walle, *Effects of cation d states on the structural and electronic properties of III-nitride and II-oxide wide-band-gap semiconductors*, Phys. Rev. B **74**, 045202 (2006).

[136] P. Erhart, K. Albe, and A. Klein, *First-principles study of intrinsic point defects in ZnO: Role of band structure, volume relaxation, and finite-size effects*, Phys. Rev. B **73**, 205203 (2006).

[137] H. J. Monkhorst and J. D. Pack, *Special points for Brillouin-zone integrations*, Phys. Rev. B **13**, 5188 (1976).

[138] W. E. Pickett, *Pseudopotential methods in condensed matter applications*, Comput. Phys. Reports **9**, 115 (1989).

[139] D. Vanderbilt, *Soft self-consistent pseudopotentials in a generalized eigenvalue formalism*, Phys. Rev. B **41**, 7892 (1990).

[140] P. E. Blöchl, *Generalized separable potentials for electronic-structure calculations*, Phys. Rev. B **41**, 5414 (1990).

[141] P. E. Blöchl, *Projector augmented-wave method*, Phys. Rev. B **50**, 17953 (1994).

[142] G. Kresse and D. Joubert, *From ultrasoft pseudopotentials to the projector augmented-wave method*, Phys. Rev. B **59**, 1758 (1999).

[143] A. Kiejna, G. Kresse, J. Rogal, A. De Sarkar, K. Reuter, and M. Scheffler, *Comparison of the full-potential and frozen-core approximation approaches to density-functional calculations of surfaces*, Phys. Rev. B **73**, 035404 (2006).

[144] R. P. Feynman, *Feynman lectures on physics. Volume 3: Quantum mechancis* (Addison Wesley, ADDRESS, 1965).

[145] C. Kittel, *Introduction to Solid State Physics (eighth edition)* (Wiley & Sons, New York, N.Y., 2005 (p.73-75)).

[146] J. Ziman, *Principles of the Theory of Solids* (Cambridge University Press, London, United Kingdom, 1972).

[147] J. Callaway, *Quantum Theory of the Solid State* (Academic Press, Inc. (London) LTD., Cambridge, United Kingdom, 1974).

[148] A. Togo and I. Tanaka, *Evolution of crystal structures in metallic elements*, Phys. Rev. B **87**, 184104 (2013).

[149] A. Ghysels, V. Van Speybroeck, E. Pauwels, S. Catak, B. R. Brooks, D. Van Neck, and M. Waroquier, *Comparative study of various normal mode analysis techniques based on partial Hessians*, J. Comput. Chem. **31**, 994 (2009).

[150] H. Li and J. H. Jensen, *Partial Hessian vibrational analysis: the localization of the molecular vibrational energy and entropy*, Theor. Chem. Acc. **107**, 211 (2002).

[151] P. C. H. Mitchell, *Vibrational spectroscopy with neutrons: with applications in chemistry, biology, materials science and catalysis* (World Scientific, London, 2005), Vol. 3.

[152] G. L. Squires, *Introduction to the Theory of Thermal Neutron Scattering* (Cambridge University Press, Cambridge, 2012).

[153] R. Osborn, E. A. Goremychkin, A. I. Kolesnikov, and D. G. Hinks, *Phonon Density of States in MgB 2*, Phys. Rev. Lett. **87**, 017005 (2001).

[154] R. Osborn, S. Rosenkranz, E. Goremychkin, and A. Christianson, *Inelastic neutron scattering studies of the spin and lattice dynamics in iron arsenide compounds*, Phys. C Supercond. **469**, 498 (2009).

[155] R. Stumm von Bordwehr, *A History of X-ray absorption fine structure*, Ann. Phys. (Paris). **14**, 377 (1989).

[156] C. Bonnelle and C. Mandé, *Advances in X-Ray Spectroscopy: Contributions in Honour of Professor Y. Cauchois* (Pergamon Press, Oxford, 1982).

[157] B. Ravel, E. A. Stern, R. I. Vedrinskii, and V. Kraizman, *Local structure and the phase transitions of* $BaTiO_3$, Ferroelectrics **206**, 407 (1998).

[158] D. E. Sayers, *A new technique to determine amorphous structure using extended x-ray absorption fine structure.*, 1972.

[159] P. Fornasini and R. Grisenti, *On EXAFS Debye-Waller factor and recent advances*, J. Synchrotron Radiat. **22**, 1242 (2015).

[160] X. Gonze and C. Lee, *Dynamical matrices, Born effective charges, dielectric permittivity tensors, and interatomic force constants from density-functional perturbation theory*, Phys. Rev. B **55**, 10355 (1997).

[161] S. Baroni and R. Resta, *Ab initio calculation of the macroscopic dielectric constant in silicon*, Phys. Rev. B **33**, 7017 (1986).

[162] M. Gajdoš, K. Hummer, G. Kresse, J. Furthmüller, and F. Bechstedt, *Linear optical properties in the projector-augmented wave methodology*, Phys. Rev. B **73**, 045112 (2006).

[163] D. Vanderbilt and R. D. King-Smith, *Electric polarization as a bulk quantity and its relation to surface charge*, Phys. Rev. B **48**, 4442 (1993).

[164] R. Resta, *Macroscopic Electric Polarization as a Geometric Quantum Phase*, Europhys. Lett. **22**, 133 (1993).

[165] R. D. King-Smith and D. Vanderbilt, *Theory of polarization of crystalline solids*, Phys. Rev. B **47**, 1651 (1993).

[166] R. Resta, *Macroscopic polarization in crystalline dielectrics: the geometric phase approach*, Rev. Mod. Phys. **66**, 899 (1994).

[167] R. Resta, *Manifestations of Berry's phase in molecules and condensed matter*, J. Phys. Condens. Matter **12**, R107 (2000).

[168] R. Resta and D. Vanderbilt, *Phys. Ferroelectr.* (Springer Berlin Heidelberg, Berlin, Heidelberg, 2007), pp. 31–68.

[169] N. A. Spaldin, *A beginner's guide to the modern theory of polarization*, J. Solid State Chem. **195**, 2 (2012).

[170] A. Togo and I. Tanaka, *First principles phonon calculations in materials science*, Scr. Mater. **108**, 1 (2015).

[171] A. Togo, L. Chaput, and I. Tanaka, *Distributions of phonon lifetimes in Brillouin zones*, Phys. Rev. B **91**, 094306 (2015).

[172] N. S. Gillis, N. R. Werthamer, and T. R. Koehler, *Properties of Crystalline Argon and Neon in the Self-Consistent Phonon Approximation*, Phys. Rev. **165**, 951 (1968).

[173] N. R. Werthamer, *Self-Consistent Phonon Formulation of Anharmonic Lattice Dynamics*, Phys. Rev. B **1**, 572 (1970).

[174] L. D. Whalley, J. M. Skelton, J. M. Frost, and A. Walsh, *Phonon anharmonicity, lifetimes, and thermal transport in $CH_3NH_3PbI_3$ from many-body perturbation theory*, Phys. Rev. B **94**, 220301 (2016).

[175] J. M. Skelton, L. A. Burton, S. C. Parker, A. Walsh, C.-E. Kim, A. Soon, J. Buckeridge, A. A. Sokol, C. R. A. Catlow, A. Togo, and I. Tanaka, *Anharmonicity in the High-Temperature C m c m Phase of SnSe: Soft Modes and Three-Phonon Interactions*, Phys. Rev. Lett. **117**, 075502 (2016).

[176] P. Souvatzis, O. Eriksson, M. I. Katsnelson, and S. P. Rudin, *The self-consistent ab initio lattice dynamical method*, Comput. Mater. Sci. **44**, 888 (2009).

[177] T. Tadano and S. Tsuneyuki, *Self-consistent phonon calculations of lattice dynamical properties in cubic $SrTiO_3$ with first-principles anharmonic force constants*, Phys. Rev. B - Condens. Matter Mater. Phys. **92**, 054301 (2015).

[178] O. Hellman, P. Steneteg, I. A. Abrikosov, and S. I. Simak, *Temperature dependent effective potential method for accurate free energy calculations of solids*, Phys. Rev. B **87**, 104111 (2013).

[179] F. Eriksson, E. Fransson, and P. Erhart, *The Hiphive Package for the Extraction of High-Order Force Constants by Machine Learning*, Adv. Theory Simulations **2**, 1800184 (2019).

[180] E. Fransson, F. Eriksson, and P. Erhart, *Efficient construction and applications of higher-order force constant models*, arXiv:1902.01271 , (2019).

[181] J. Updike, *The Dance of the Solids*, Scientific American **220**, 130 (1969).

[182] J. Maier, *Physical chemistry of ionic materials: ions and electrons in solids* (John Wiley & Sons, West Sussex, England, 2004).

[183] S. Zhang and J. Northrup, *Chemical potential dependence of defect formation energies in GaAs: Application to Ga self-diffusion*, Phys. Rev. Lett. **67**, 2339 (1991).

[184] S. Lany and A. Zunger, *Assessment of correction methods for the band-gap problem and for finite-size effects in supercell defect calculations: Case studies for ZnO and GaAs*, Phys. Rev. B **78**, 235104 (2008).

[185] C. Freysoldt, J. Neugebauer, and C. G. Van de Walle, *Electrostatic interactions between charged defects in supercells*, Phys. status solidi **248**, 1067 (2011).

[186] H.-P. Komsa, T. T. Rantala, and A. Pasquarello, *Finite-size supercell correction schemes for charged defect calculations*, Phys. Rev. B **86**, 045112 (2012).

[187] *NIST Computational Chemistry Comparison and Benchmark Database NIST Standard Reference Database Number 101, Release 18, Editor: Russell D. Johnson III, http://cccbdb.nist.gov.*

[188] *NIST JANAF thermochemical tables 1985, Editor: Malcolm W. Chase Jr, http://kinetics.nist.gov/janaf.*

[189] D. A. Porter, K. E. Easterling, and M. Y. Sherif, *Phase Transformations in Metals and Alloys* (CRC Press, Taylor & Francis Group, Boca Raton,FL, 2009).

[190] E. K. Salje, *Phase Transitions in Ferroelastic and Co-elastic Crystals*, *Cambridge Topics in Mineral Physics and Chemistry* (Cambridge University Press, Cambridge, 1991).

[191] M. T. Dove, *Introduction to lattice dynamics*, *Cambridge Topics in Mineral Physics and Chemistry* (Cambridge University Press, Cambridge, 1993).

[192] E. Salje, *Phase transitions in ferroelastic and co-elastic crystals*, Ferroelectrics **104**, 111 (1990).

[193] M. A. Carpenter, *Elastic anomalies accompanying phase transitions in (Ca,Sr)*TiO_3 *perovskites: Part I. Landau theory and a calibration for* $SrTiO_3$, Am. Mineral. **92**, 309 (2007).

[194] M. A. Carpenter, *Elastic anomalies accompanying phase transitions in (Ca,Sr)*TiO_3 *perovskites: Part II. Calibration for the effects of composition and pressure*, Am. Mineral. **92**, 328 (2007).

[195] M. Guennou, P. Bouvier, J. Kreisel, and D. Machon, *Pressure-temperature phase diagram of* $SrTiO_3$ *up to 53 GPa*, Phys. Rev. B **81**, 054115 (2010).

[196] A. Togo, F. Oba, and I. Tanaka, *First-principles calculations of the ferroelastic transition between rutile-type and* $CaCl_2$*-type* SiO_2 *at high pressures*, Phys. Rev. B **78**, 134106 (2008).

[197] H. B. Callen, *Thermodynamics* (Wiley & Sons, New York, N.Y., 1960 (p.213-219)), p. 213.

[198] A. Nowic and B. Berry, *Anelastic Relaxation in Crystalline Solids* (Academic Press, London, 1972).

[199] G. A. Holzapfel, *Nonlinear Solid Mechanics: A Continuum Approach for Engineering* (Wiley, Chichester, New York, 2000 (chap. 2)).

[200] C. Franchini, *Hybrid functionals applied to perovskites*, J. Phys. Condens. Matter **26**, 253202 (2014).

[201] R. Wahl, D. Vogtenhuber, and G. Kresse, *SrTiO and BaTiO revisited using the projector augmented wave method*, Phys. Rev. B **78**, 104116 (2008).

[202] K. Popper, *The Logic of Scientific Discovery* (Hutchinson & Co, London, 1959).

[203] F. Bruneval, C. Varvenne, J.-P. Crocombette, and E. Clouet, *Pressure, relaxation volume, and elastic interactions in charged simulation cells*, Phys. Rev. B **91**, 024107 (2015).

[204] F. Crick, *What Mad Pursuit* (Penguin, London, 1990), p. 150.

[205] T. Hahn, in *International tables for crystallography. Volume A, Space-group symmetry*, fifth edit ed., edited by T. Hahn (Springer, Dordrecht, 2002), p. 911.

[206] M. Dresselhaus, G. Dresselhaus, and A. Jorio, *Group Theory: Application to the Physics of Condensed Matter* (Springer, Heidelberg, 2008).